Design, Modeling and Fabrication of Radio-Frequency Microelectromechanical Switches and Coplanar Filters

Dissertation
zur Erlangung des akademischen Grades

Doktoringenieur
(Dr.-Ing.)

von **M. Sc. Anatoliy Batmanov**
geb. am 21. Januar 1979 in Stebnyk, Ukraine

genehmigt durch die Fakultät für Elektrotechnik und Informationstechnik
der Otto-von-Guericke-Universität Magdeburg

Gutachter:
Prof. Dr.-Ing. Edmund P. Burte
Prof. Dr.-Ing. Abbas S. Omar

Promotionskolloquium am: 14 April 2010

Zusammenfassung

Das Ziel der hier vorgelegten Dissertation waren die Modellierung, der Entwurf, die Herstellung und die messtechnische Charakterisierung von mikroelektromechanischen (MEMS) Schaltern sowie koplanaren Filtern für Anwendungen im Hochfrequenzbereich (HF).

Die elektro-mechanische Modellierung und Optimierung von HF MEMS Schaltern mittels Finite Element Methoden (FEM) wurde untersucht. Dabei wurden zwei verschiedene Ansätze der Modellierung des elektrostatisch-strukturierten Problems verwendet. Die erste Methode basiert auf der konsequenten Anwendung eines Kopplungsalgorithmus, wobei die elektrostatische und die mechanische Problemstellung nacheinander gelöst wurden. Die zweite Methode benutzte eine reduzierte Ordnung des Modells, bei dem die beiden Probleme durch Wandlerelemente (transducer elements) beschrieben (gekoppelt) wurden. Die elektromagnetische Simulationen der HF MEMS Schalter und der HF Filterstrukturen wurden mit den elektromagnetischen (EM) 3-D Simulatoren durchgeführt.

Neue Designs von kapazitiven und DC-Kontakt MEMS Schaltern mit geringer Betätigungsspannung (4 V … 13 V) und hoher HF-Performance für die Anwendungen in den L-, S- und X-Bändern wurden entworfen. Es wurden zwei Methoden zur Erhöhung der kapazitiven Kopplung und der damit verbunden Verschiebung der Resonanzfrequenz des kapazitiven MEMS Schalters zu einem tieferen Frequenzbereich hin (0,8 GHz ... 2 GHz) eingesetzt und optimiert. Ein erster erfolgreicher Lösungsansatz basierte auf der Gestaltung einer MIM (metal-insulator-metal) Struktur, die auf dem HF-Leiter gegenüber der MEMS Brückenstruktur angeordnet war. Im Zusammenwirken mit der Top-Elektrode der MIM Struktur realisierte die Brückenstruktur einen ohmschen Kontakt. Mit einem solchen MEMS Schalter wurde im Frequenzbereich von 1,5 GHz bis 35 GHz eine Isolation von mehr als -20 dB erreicht. Darüber hinaus zeigte die neue Geometrie der Brückenstruktur in Verbindung mit dem Signalleiter eine Einfügungsdämpfung, die bis zu einer Frequenz von 35 GHz nur bei -0,3 dB lag. Im zweiten Lösungsansatz zur kapazitiven Kopplung von RF Schalterstrukturen finden zum Unterschied zur ersten zwei Kondensatoren ihren Einsatz, die gegen das Massepotenzial geschaltet sind. Technologisch erfolgte die Herstellung der Isolationsschicht in der Weise, dass sie mittels Abscheidung einer dielektrischen Schicht auf der Massefläche aufgesetzt wurde. Dieser MEMS Schalter zeigte auch eine sehr niedrige

Einfügungsdämpfung, die für einen erweiterten Durchlassbereich bis zu einer Frequenz von 40 GHz bei -0,8 dB lag und im Frequenzbereich von 0,8 GHz bis 40 GHz eine Isolation, die unter -20 dB lag, aufwies. Dazu wurde eine neue Methode zur Herstellung einer out-of-plane Membran vorgeschlagen.

Konventionelle kapazitive MEMS Schalter wurden simuliert und auf hochohmigem Siliziumsubstrat in CMOS-kompatibler Dünnschicht-MEMS-Technologie hergestellt. Dazu wurden alle Herstellungsprozesse für die Anforderungen an die Schalter entwickelt und erprobt. Niedertemperatur ECR-PECVD Prozesse zur Abscheidung der dielektrischen Schichten aus Siliziumnitrid mit hoher Durchschlagspannung, mit niedriger relativer dielektrischer Konstante, und mit geringer Oberflächenrauhigkeit wurden entwickelt und optimiert. Die Trockenätz- sowie Nasschemie-Prozesse zur Strukturierung der eingesetzten metallischen und dielektrischen Schichten wurden angepasst und optimiert. Die hergestellten MEMS-Schalter wurden getestet und die Messergebnisse mit den Simulationsergebnissen verglichen, wobei eine gute Übereinstimmung aufgezeigt werden konnte.

Zusätzlich wurden koplanaren Filterstrukturen entworfen, simuliert und auch hergestellt. Dazu wurden zwei unterschiedliche Methoden zur Realisierung von Bandpassfiltern (BPF) eingesetzt. Die erste Methode basierte auf den $\lambda/4$ open-stubs Resonatoren, die kapazitiv gekoppelt sind. Ein anderer Ansatz war eine induktiv Shunt-gekoppelte Struktur, die mittels Serpentin förmiger shunt-stubs realisiert wurde. Dabei konnte die hohe HF-Performance und die Kompaktheit von BPF erreicht werden. Die Fraktal-Methode wurde verwendet, um die Verbesserung der HF-Eigenschaften von konventionellen zweidimensionalen periodischen rechteckigen DGS (defected ground structure) zu erreichen. Es wurden zwei weitere Anordnungen der DGS entworfen und untersucht, um die HF-Performance von DGS-Resonatoren weiter zu verbessern. Dabei wurde die Abhängigkeit der Ersatzschaltungselemente von den Entwurfsparametern der DGS demonstriert. Um damit hochwertige koplanare DGS Tiefpassfilter (LPF) entwerfen zu können, wurde die Kaskadierungsmethode zur Anwendung gebracht. Alle diese theoretischen Ergebnisse konnten erfolgreich experimentell bestätigt werden.

Als Ausführungsbeispiel für die Anwendung von MEMS-Schaltern wurde ein kompakter, abstimmbarer HF-MEMS Quasi-DGS Bandpassfilter für den Einsatz im K-Band entworfen. Die vorgeschlagene Filterstruktur wurde mit dem Ersatzschaltmodell sowie mit dem EM-Simulator untersucht. Ein derartiges Bandpassfilter kann unter anderem in Automobilen und in Transceivern seinen Einsatz finden.

Content

Physical Symbols and Abbreviations

α	Coefficient of thermal expansion K^{-1}
BPF	Bandpass filter
BSF	Bandstop filter
BST	Barium strontium titanate
CMOS	Complementary metal-oxide-semiconductor
CPW	Coplanar waveguide
CVD	Chemical vapour deposition
D	Plate stiffness N/m
DGS	Defected ground structures
DOG	Dielectric on ground
E	Young's modulus N/m^2
E	Electrostatic field V/m
ECR	Electron cyclotron resonance
F_e	Electrostatic force N
F_r	Restoring force
fo	Resonant frequency Hz
FEM	Finite element method
FET	Field Effect Transistor
G	CPW slot width µm
g_o	Nominal gap height µm
HMDS	Hexamethyldisilazane
I	Moment of inertia m^4
k	Spring constant N/m
L_m	Beam length m
LIGA	Lithographie, Galvanoformung und Abformung
LPF	Low-pass filter
MEMS	Micro-electro-mechanical systems
MIM	Metal-insulator-metal
MIC	Microwave integrated circuit
MMIC	Monolithic microwave integrated circuit
MoM	Method of moment
PBG	Photonic band gap

PECVD	Plasma enhanced chemical vapor deposition
PIN diode	Positive intrinsic negative diode
PR	Photoresist
PVD	Physical vapour deposition
Q-factor	Quality factor
R_a	Average surface roughness
RF	Radio-frequency
RFIC	Radio-frequency integrated circuit
RIE	Reactive ion etching
ROM	Reduced order modeling
SP2T	Single-pole double-throw
SP4T	Single-pole four-throw
STO	Strontium titanate
TEM	Transverse electromagnetic mode
t_m	Beam thickness μm
t_m	Thickness of dielectric film μm
u	Transverse beam displacement μm
UWB	Ultra wideband
V	Applied voltage Volts
V_p	Pull-down voltage Volts
VLSI	Very large-scale integration
λ	Wavelength m
W	Lower electrode width μm
w_m	Beam width μm
ρ	Electrostatic charge density Q/m^2
v	Poisson's ration |
σ	Biaxial residual stress N/m^2
σ_t	Thermal stress N/m^2
ε_o	Free space permittivity F/m
ε_t	Thermal strain N/m
XPS	X-ray photoelectron spectroscopy

Chapter 1

Introduction and Basic Considerations

Micro-Electro-Mechanical Systems (MEMS) technology allows the fabrication of miniature devices or systems which are able to combine electrical and mechanical components and are scaled in the size from micrometers to millimeters [1-9]. These MEMS products range from physical sensors (e.g. pressure, inertial) to radio-frequency (RF) devices and are useful for many different industrial and research applications [1, 3]. They are already used in automotive, chemical, medical, optical, robotic and sensing systems, for instance.

Radio-frequency (RF) MEMS technology offers new possibilities to improve performance of the devices which work in millimeterwave and microwave ranges such as RF switches, phase shifter, routing switches, time delay networks, reconfigurable antennas, tunable filters and resonators and other passive components [10-17]. It allows the fabrication of devices which are advantageous over conventional RF component with unique actuation mechanism, miniature size, and high integration features. Planar RF MEMS passive devices or circuits which can be batch processed lead to an increase of the functionality without extra connector losses and to a dramatic reduction of the manufacturing costs. Also, millimeterwave devices, which are fabricated by MEMS technology, have high Q-factors, that can solve the loss issues associated with passive devices. In addition, this technology allows to use a variety of substrates.

Currently, three different RF MEMS fabrication technologies are predominantly used:

- Bulk micromachining techniques, which utilize wet- or dry etching processes to produce an isotropic or anisotropic etch profile in a material in order to form the microstructures with desired shapes as shown in Figure 1.1 (a).
- Surface micromachining techniques (see Figure 1.1 (b)) form the microstructures on the surface of silicon or any other suitable substrate by using thin films and sacrificial layers. This technique offers the possibility to integrate the electronics and the MEMS structure more easily. Generally, this technique is limited by a film thickness of 2 μm to 6 μm with an overall device thickness of < 15 μm [1].

- LIGA (Lithographie, Galvanoformung und Abformung, a German acronym for Lithography, Electroplating and Molding) is a technology which allows to form complex structures with very high aspect ratios using x-ray lithography, thick resist layers and electroplated metals, as illustrated in Figure 1.1 (c).

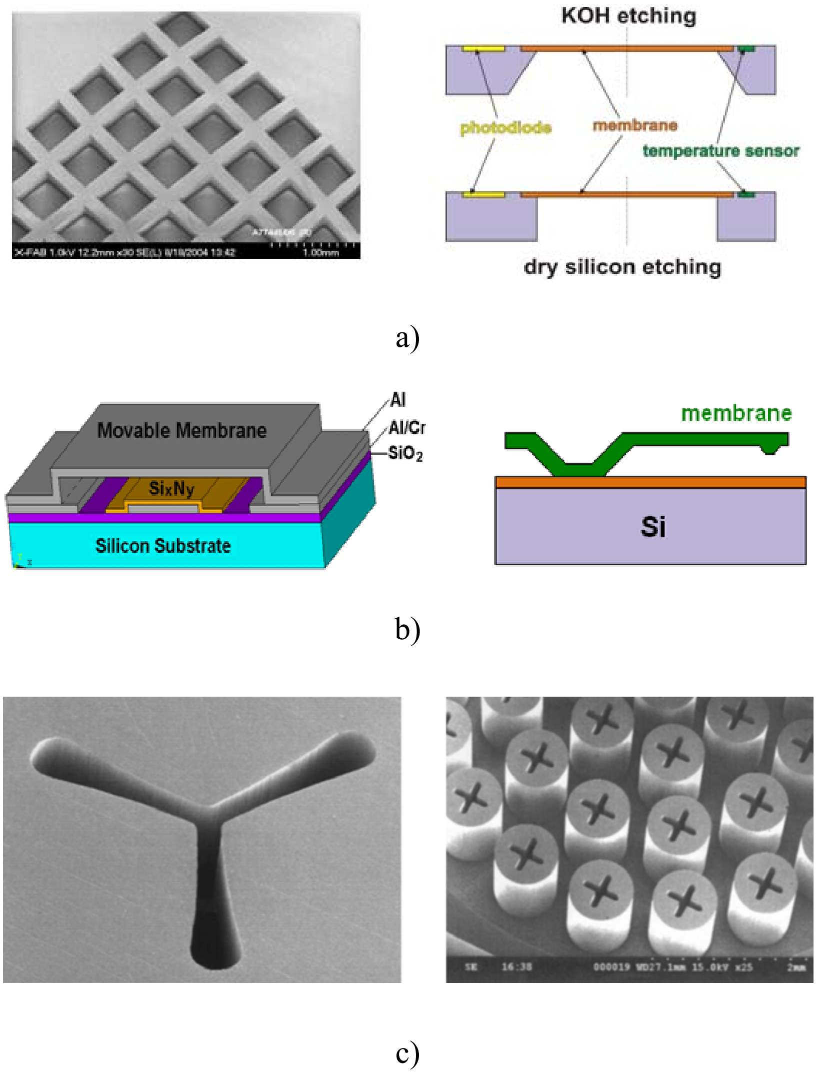

Figure 1.1: MEMS fabrication techniques: (a) bulk micromachining [18], (b) surface micromachining and (c) LIGA process [19].

Micro-Electro-Mechanical Systems have been developed since 1970s for sensor applications. But the most common MEMS devices for RF/Microwave applications are MEMS switches and varactors. The first RF MEMS switch (and varactor) has been investigated in 1990-1991, by Dr. Larry Larson at Hughes Research Labs in Malibu, California [20]. Figure 1.2 shows some application fields of RF MEMS switches: a 2-bit MEMS phase shifter using SP4T switches (a), phased-array antenna (b), and single-pole double-throw (SP2T) transceiver switches (c).

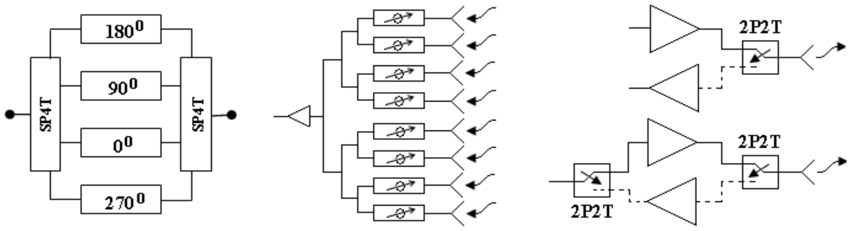

a) b) c)

Figure 1.2: Some application fields of RF MEMS switches: a 2-bit MEMS phase shifter using SP4T switches (a), phased-array antenna (b), and single-pole double-throw (SP2T) transceiver switches (c).

1.1 RF MEMS Switches

The conventional MEMS devices for millimetre/microwave applications are RF MEMS switches. In these devices a mechanical movement is used to realise an open or short circuit in the RF transmission line (for a given bandwidth). In other words, the impedance of an RF transmission line is controlled by the physical mechanical movement of an RF MEMS switch. The very first cantilever beam MEMS switches have been fabricated on silicon and investigated for low-frequency applications [21, 22]. Therefore, many devices are based on polysilicon, which has excellent mechanical properties [23]. But for the microwave low-loss circuits the polysilicon is not suitable due to its high resistivity. That has been the reason to develop high-conductivity metallic MEMS components. Aluminum, gold and copper are usually used as materials for the fabrication [24-28], while nickel and platinum have also been demonstrated as potential candidates [29, 30].

RF MEMS switches are suitable for low-loss microwave systems, which do not require high switching rates, such as: cellular telephone, airborne, automotive and satellite communication. The advantages of RF MEMS switches over their solid-state counterparts, such as FETs or PIN diodes, are:

1. *Low Power Consumption*: Electrostatic actuated switches operate by a dc voltage but do not consume any current resulting in a very low power consumption.
2. *Very Low ON-state Insertion Loss*.
3. *Very High Off-state Isolation*.
4. *High Intermodulation Products*: Due to a very high linearity of the RF MEMS switches (no *p*-*n* junction) they provide negligible intermodulation distortion.

5. *Very Low Fabrication Cost*: RF MEMS switches can be fabricated on different substrates using surface micromachining techniques and do not require high cost processes.

However, RF MEMS switches have also some disadvantageous, such as:

1. *Relatively Low Switching Time*: The switching time of most RF MEMS switches is between 1 µsec and 200 µsec. This relatively low switching speed does not satisfy the requirements for some communication and radar systems. However, etching holes in the movable membrane allows faster operation by reducing the damping effect.
2. *Low Power Handling*: Most RF MEMS switches can handle a power of 20-50 mW, but not more.
3. *High Actuation-Voltage*: Conventional electrostatic RF MEMS switches require 20-80 V for a reliable operation, a rather high voltage. Therefore, a lot of work has been done to reduce the actuation-voltage values [31-36].
4. *Low Reliability*: The lifetime of mature RF MEMS switches is higher than 50 billion cycles. But, a lot of microwave systems require switches with lifetime of more than 200 billion cycles.
5. *Packaging*: The packaging technique itself can lead to significant degradation of the switch reliability.
6. *High Total Cost*: Costs of packaging have a high share of total costs in switch fabrication [37, 38, 39]. Additionally, the high-voltage drive has to be considered, while fabrication costs of the switch itself are rather low [40].

The RF MEMS switches can be generally classified based on contact type, actuation mechanism, construction and circuit configuration. Two different contact mechanisms can characterize RF MEMS switch designs: a capacitive contact (metal-insulator-metal) and a resistive (metal-to-metal) contact. The capacitive contact switch is characterized by the capacitance ratio between the up-state (ON-state) and the down-state (OFF-state) positions. This ratio typically ranges from 80 to 200 and depends on the switch design. The OFF-state capacitance amounts to 2-4 pF, and is suitable for 5-100 GHz applications. The conventional dielectric films used in RF MEMS switches are silicon oxide or silicon nitride. They do not allow to obtain a large down-state capacitance due to their low dielectric constant that limits the low-frequency operation of the switches. This problem can be solved by using high dielectric constant materials such as strontium titanate (STO), barium strontium titanate (BST) or titanium oxide [41-46]. But these dielectric materials require a special technology and are not standard materials for CMOS technology. Moreover, MEMS capacitive switches with high relative dielectric constant materials are very sensitive to the capacitance degradation caused by non-planar metal membranes and surface roughness of the dielectric layer [39]. A method to eliminate the effect of the surface roughness is the deposition of a thin metal film directly on the dielectric layer [47]; by doing so a metal-insulator-metal (MIM) structure on the center line is formed. In [48] the dielectric on ground (DOG) approach has been introduced to increase the down-state capacitance and, in such a way, to improve the switch isolation at lower frequencies. Resistive contact switches have small up-state capacitances (ON-state) and operate from 0.01 GHz up to 60 GHz. For example, the design of the Rockwell Scientific switch [49] provides an OFF-state capacitance of only 1.75 fF and an isolation of -23 dB at 60 GHz. In the ON-state a gap in the microwave t-line is contacted together by the MEMS switch forming a series resistor with a resistance of 0.5-2 Ω, depending on the used contact material. The main disadvantage of the dc-contact switch, compared to the capacitive coupled one, is a contact metal degradation leading to a short lifetime [50-52].

Four most frequently used actuation methods for RF MEMS switches are based on electrostatic [53], magnetostatic [54], piezoelectric [55] or thermal [56] techniques. In the magnetostatic MEMS switches the mechanical actuation is based on the Lorentz force, when the pulling force is induced by a magnetic field. Motion force of piezoelectric MEMS switches is based on the ability of certain materials to change their geometrical dimensions in response to the applied electrical potential. A change in a linear dimension due to thermal expansion of any solid underlies the functioning of the thermal MEMS switches. But the majority of the RF MEMS switches are electrostatic in nature. Their motion is actuated by the attractive Coulomb's force existing between charges of opposite polarity. The electrostatically actuated MEMS switch has a great potential for microwave applications due to its extremely high power handling capability and compatibility with other state-of-the-art fabrication technologies for high level integrated circuits or systems. Moreover, the fabrication of these switches is relatively simple and requires only a minimum of commonly available fabrication equipment. A drawback is the high actuation-voltage, which is in the range of 20 V to 80 V. The high actuation-voltage can cause the stiction between a movable membrane and a bottom electrode. It has been investigated and published that the failure mechanism is due to a charge accumulation in the dielectric material [57-60]. This charge builds up in the dielectric layer and is strictly related to the actuation-voltage. It has been observed that a switch lifetime is increased by one order of magnitude for every 5-7 V reduction of the applied voltage [60].

Two different constructions of the RF MEMS switches are commonly used: cantilever or fixed-fixed beam. The cantilever type has an important advantage in comparison to the suspension bridge, a lower actuation-voltage [4]. But these switches are very sensitive to residual mechanical stress in the beam material. The fabrication process of the fixed-fixed beam configuration is easier and does not require special processing compared to dielectric beams or thick low-stress electroplated cantilevers [61].

RF MEMS switches can also be classified according to the configuration of the circuit. Generally, there are two configurations: shunt and series configurations depending on the position across a transmission line. A shunt configuration is typically used for capacitive switches [62], while a series configuration is major used for resistive-contact switches [63]. The reason is that it is easier to get a good isolation with a limited impedance ratio (such as the capacitive switch) in a shunt-circuit than in a series circuit. Both configurations of RF MEMS switches are implemented either for microstrip or coplanar waveguide (CPW) lines on glass, quartz, silicon, *GaAs*, and other substrates [15, 64, 65, 66, 67], and have been used in these implementations up to 100 GHz. High-resistivity materials must be used as substrate in order to eliminate dielectric losses in the substrate for low-loss microwave applications.

1.1.1 State-Of-The-Art

During the last years, the MEMS market showed a rapid roughly exponential growth. It is expected to reach the $8.3 billion dollars by 2012, up from $5.6 billion in 2006. This is mostly due to the incorporation of MEMS devices into accelerometers, microphones, gyroscopes, pressure devices and more recently, the application of RF MEMS devices in mainstream consumer products [68].

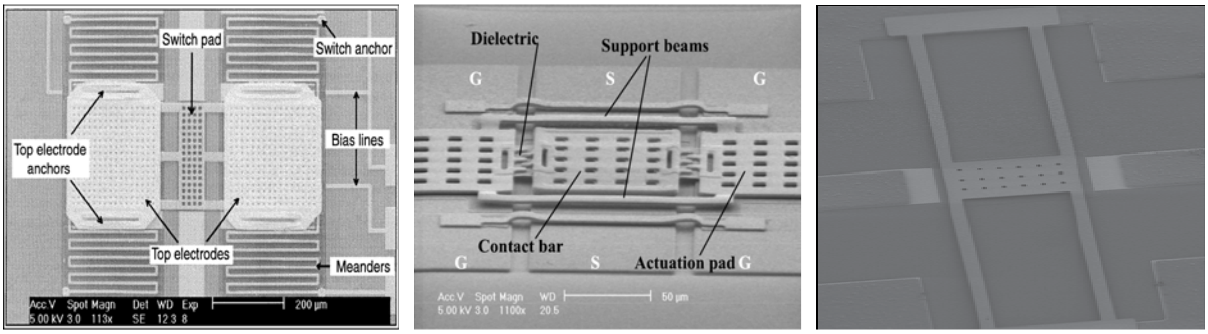

a) b) c)

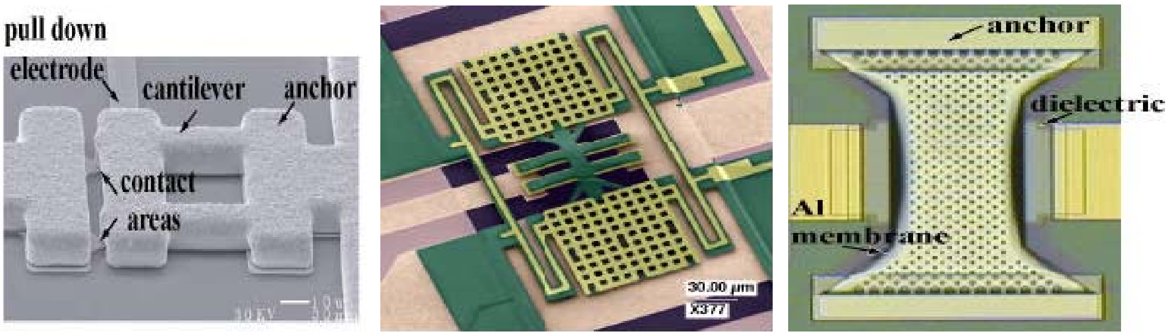

d) e) f)

Figure 1.3: Photomicrographs of MEMS switches: (a) low-voltage MEMS shunt-capacitive switch of the University of Michigan [36], (b) direct contact MEMS switch of the Ewha Womans University [69], (c) shunt-capacitive switch of Electronic Laboratory (EPFL) [46], (d) the Radant MEMS series switch [63], (e) the Rockwell Scientific MEMS series switch [49], and (f) the Raytheon MEMS shunt-capacitive switch [24, 70].

More than 120 research centers, laboratories and universities in Europe are involved in MEMS technologies, developing and investigating a large variety of modern processes and device concepts and providing considerable tests. A huge amount of RF MEMS switches and RF MEMS based devices have been introduced, developed, tested and presented in open sources. The choice of the type of RF MEMS switch depends on the performance requirements, on the application and on the manufacturing facilities. In Figure 1.3 several examples of these switches are shown.

1.1.2 RF MEMS Switch Analytical Modeling

Electrostatic Domain

The fundamental principle of an electrostatic actuation is the attraction of two plates of opposite charge to each other. It is widely used as it allows a relatively straightforward fabrication. However, this force is nonlinearly related to the applied voltage. The simple parallel plate model is shown in Figure 1.4. The electrostatic force (F_e) within the initial gap g_0 is directly related to the local separation g (see Figure 1.5) as:

$$F_e(V,g) = -\frac{1}{2}V^2\frac{dC(g)}{dg}, \tag{1.1}$$

where C is the capacitance of the parallel plate model and V is the applied voltage.

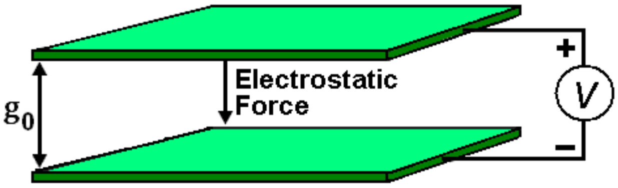

Figure 1.4: A simple parallel plate electrostatic actuator.

If the initial gap g_0 is much smaller than the lateral dimensions of the parallel plate structure, a fringing field effect can be neglected and the capacitance can be calculated as:

$$C(g) = \frac{\varepsilon_0 A}{g_0} \tag{1.2}$$

where ε_0 is the free space permittivity and A is the area of the plate. Substituting $C(g)$ into the electrostatic force equation yields:

$$F_e(V,g) = -\frac{1}{2}V^2\frac{\varepsilon_0 A}{g^2} \tag{1.3}$$

It can be seen from equations above that the force tends to infinity if the gap separation reaches zero.

Electrostatic force can also be expressed in term of the electric field applied to the plate as:

$$F_e = \frac{QE}{2}, \tag{1.4}$$

where Q is the charge on the plate and $E=V/g$ is the electric field caused by the applied voltage. The charge induced on the plate is increased as the applied voltage is increased that results in an increase in the electrostatic force.

Mechanical Domain

The theory of beams and plates can be used to describe the mechanical behaviour of MEMS structures [71, 72]. However, the theory of beams covers the movement of a components only in one direction. In the case of a significant deformation in two directions, the theory of plates and shells must be used. At a small deflection the restoring force, F_r, countering the electrostatic force and preventing the beam from immediately collapsing onto bottom electrode is given by:

$$F_r = -k(g_0 - g), \tag{1.5}$$

where k is normalized spring constant of the beam, and g_0-g is the small deflection of the beam from its initial position as shown in Figure 1.5. The effective spring constant k of the membrane can be expressed as [73]:

$$k = \frac{32Et_m^3 w_m}{L_m^3} + \frac{8\sigma(1-v)t_m w_m}{L_m}, \tag{1.6}$$

where E and v are the Young's modulus and Poisson's ratio of the membrane material, respectively, t_m and L_m are the thickness and the length of the membrane, respectively, and σ is the tensile residual stress in the membrane.

It should be noted that a very low spring-constant design with a thin meander which supports the bridge anchors results in a large bridge inductance affecting the operation of the switch above 10.0 GHz [39]. Also, the isolation of the switch is strongly depending on the connection of the switch to the post [39].

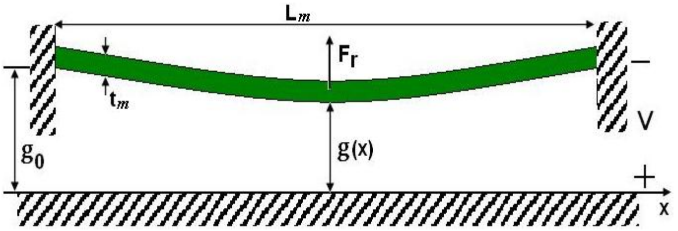

Figure 1.5: Schematic diagram of the simple 2-D distributed model for fixed-fixed beam.

Electromechanical Coupling

Electrostatic actuation provides very low forces, but it is a high enough for the actuation of a MEMS switch. When a dc voltage is applied between both, fixed and movable electrodes, the movable part is pulled down, the gap is reduced, and the electrostatic force increases. On the other hand, the restoring force acts in the opposite direction. The force balance equation for the electrostatic and the mechanical forces is given by:

$$F(V,g) = F_r, \tag{1.7}$$

$$\frac{\varepsilon_0 \varepsilon_r A V^2}{2g^2} = k(g_0 - g), \tag{1.8}$$

The solution of this cubic equation in term of g results in an unstable position of the beam at $2g_0/3$ due to a positive feedback in the electrostatic actuation. At a deflection higher than $2g_0/3$ a complete collapse of the movable plate to the lower electrode happens. The voltage that causes this collapse is expressed as:

$$V = \sqrt{\frac{2k}{\varepsilon_0 \varepsilon_r A} g^2 (g_0 - g)}\,, \tag{1.9}$$

The schematic diagram of the conventional MEMS switch is shown in Figure 1.6. In this case, the up-state capacitance is defined by the thick air gap, g_0, and the thin dielectric layer in series and is given by:

$$C(g) = \frac{\varepsilon_0 A}{g_0 + \left(\frac{t_d}{\varepsilon_r}\right)}\,, \tag{1.10}$$

where t_d and ε_r are the thickness and the relative dielectric constant of the dielectric layer. Then the electrostatic force is calculated using Eqn. (1.10) and is:

$$F(V,g) = \frac{1}{2}\frac{V^2 \partial C(g)}{\partial g} = \frac{1}{2}\frac{\varepsilon_0 A V^2}{\left(g_0 + \left(\frac{t_d}{\varepsilon_r}\right)\right)^2}\,, \tag{1.11}$$

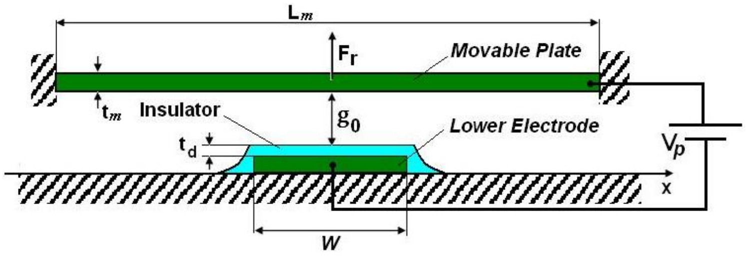

Figure 1.6: Schematic diagram of the simple 2-D for fixed-fixed beam MEMS switch.

The mechanical restoring force is the same as in the case of the parallel plate model. Substituting this value in Eqn. (1.7) and assuming that the height at which instability occurs is found to be exactly $2g_0/3$, the "pull-down" voltage is found to be [39]:

$$V_p = \sqrt{\frac{8k}{27\varepsilon_0 W w_m} g_0^3}\,, \tag{1.12}$$

where w_m and W is the width of the membrane and the lower actuation electrode, respectively. It should be noted that the pull-down voltage does not depend on the beam width, since the spring constant, k, varies linearly with the beam width, w_m. Eqn. (1.12) is a first-order approximation to model the MEMS switch as a parallel plate capacitor, which has some disadvantages. The first one is that the structure is fixed at both edges, thus the structure is not an ideal parallel plate capacitor. The second one is that the stiffness of the beam is not constant, especially at large deformations. In [74, 75] Senturia and co-workers determined the deflection of a beam under applied voltage by solving an elastic beam equation. The governing differential equation, which balances the electrostatic and the mechanical restoring forces, is given as:

$$E'I\frac{d^4g}{dx^4} - T\frac{d^2g}{dx^2} = -\frac{\varepsilon_0 V^2}{2g_0^2}(1+0.65\frac{g_0}{w_m}), \tag{1.13}$$

where $I = \frac{1}{12}w_m t_m^3$ is the moment of inertia, $T = \sigma(1-v)w_m t_m$, t_m is the thickness of the membrane, σ is the biaxial tensile residual stress in the membrane, and v is the Poisson's ratio for the membrane material. The factor in parentheses on the right-hand side of the equation is a fringing field correction. If $w_m<5t_m$ (short beam) the effective modulus E' is equal to Young's modulus of the membrane material E and in the case of $w_m \geq 5t_m$ the effective modulus is $E'=E/(1-v^2)$ [74]. A solution for this equation shows that a stable position of the beam is possible until the beam deflection is approximately 40% of the initial gap. When no residual stress is present in the membrane and the initial gap height is much smaller than the bridge width the pull-down voltage is given as [74]:

$$V_p \approx 3.444\sqrt{\frac{E't_m^3 g_0^3}{\varepsilon_0 L_m^4}} \tag{1.14}$$

Thermo Mechanical Analysis

The main effect of the temperature variation is to change the residual stress and the stress gradient in the membrane for the fixed-fixed beams. When the temperature of the switch membrane changes, the membrane becomes stressed by a normal mechanical strain. The thermal strain for a homogeneous and isotropic material is given by:

$$\varepsilon_t = \alpha(\Delta T), \tag{1.15}$$

where α is the coefficient of thermal expansion and ΔT is the temperature variation. Due to the fact that the second component of the spring constant in Eqn. (1.6) depends on the value of the residual stress the effective spring constant of the membrane will be changed. The value of the thermal stress due to a temperature variation can be calculated as [71]:

$$\sigma_t = \frac{E\alpha(\Delta T)}{1-v}, \tag{1.16}$$

where E and v are the Young's modulus and Poisson's ratio of the membrane material, respectively. For a fixed-fixed beam with a dominating residual stress, the spring constant can be changed by ±20% in the temperature range from -20^0 C to +85^0 C, resulting in a ±10% variation in the pull-down voltage [49].

Electromagnetic Domain Simulation for Fixed-Fixed Beam MEMS Switches

The RF parameters which usually characterize MEMS switches are: the ON-state insertion loss, the OFF-state isolation and the return loss in both states. Basically, it is desirable to have a low insertion and a high return loss in the ON-state and a high OFF-state isolation. The RF MEMS switches considered in this thesis are the series switches, Figure 1.6 (a) and the shunt-capacitive switches, Figure 1.6. (b), with fixed-fixed beam implementations.

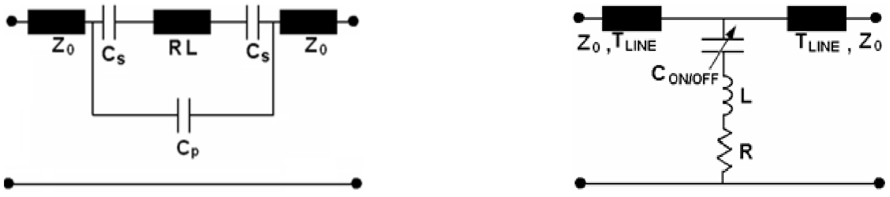

a) b)

Figure 1.6: Two port equivalent RF circuit for a MEMS switch: (a) in series configuration and (b) shunt-capacitive configuration.

The series switch in the up-position represents an open circuit with a 40-100 μm wide gap in the microwave t-line resulting in a high isolation. When the switch is in the down-position, a short circuit between the open ends is created. The up-state isolation of the dc-contact series switch is calculated as [39]:

$$S_{21} = \frac{2j\omega C_u Z_0}{1 + 2j\omega C_u Z_0}, \tag{1.17}$$

where $C_u = C_s/2 + C_p$. When $S_{21} <<$ -10 dB and $2\omega C_u Z_0 << 1$ the up-state isolation can be approximated as:

$$|S_{21}|^2 \approx 4\omega^2 C_u^2 Z_0^2 \tag{1.18}$$

In the down-state, the equivalent series impedance of a dc-contact switch is given by [39]:

$$Z_s = R + j\omega L, \tag{1.19}$$

and if $Z_s = R$, $(\omega L << R)$ then return loss is calculated as:

$$|S_{11}|^2 = \left(\frac{R}{2Z_0}\right)^2, \tag{1.20}$$

where L is the inductance of the switch in the down-state position.

The shunt impedance of the MEMS shunt-capacitive switch corresponding to the lumped *LCR* model in Figure 1.6 (b) is given by:

$$Z_s = R + j\omega L + \frac{1}{j\omega C}, \tag{1.21}$$

where *C* is the down- or the up-state capacitance. The *LC* series-resonant frequency of the switch is:

$$f_0 = \frac{1}{2\pi}\frac{1}{\sqrt{LC}} \tag{1.22}$$

At frequencies lower than the inductance-capacitance *LC* series-resonant frequency the switch behaves as a capacitor, while at frequencies above the *LC* resonant frequency it represents a inductance, and is a pure resistance at the resonant.

The reflection coefficient (return loss) in the up-state position can be calculated as [39, 76]:

$$S_{11} = \frac{-j\omega C_u Z_0}{2 + j\omega C_u Z_0}, \tag{1.23}$$

if $S_{11} \leq$ -10 dB or $\omega CuZ_0 << 2$ then:

$$|S_{11}|^2 \approx \frac{\omega^2 C_u^2 Z_0^2}{4} \tag{1.24}$$

When a bias voltage is applied, the movable bridge collapses onto the dielectric layer, largely increasing the switch capacitance by a factor of 30-100. The t-line becomes to be connected to the ground by this capacitance resulting in the reflection of the RF power. Then the relationship between the capacitance and the insertion loss in the down-state is [76]:

$$S_{21} = \frac{1}{1 + j\omega C_d Z_0 / 2} \tag{1.25}$$

and if $S_{21} <<$ -10 dB and $\omega C_d Z_0 >> 2$ then:

$$|S_{21}|^2 \approx \frac{4}{\omega^2 C_d^2 Z_0^2} \tag{1.26}$$

The down-state capacitance can be determined from the measured isolation which is taken far away from the resonant frequency [39, 76].

Conventional RF MEMS shunt-capacitive switches have a good performance from the X-band (8-12 GHz) to the W-band (75-110 GHz) frequency range [5, 24, 61, 65, 76, 77, 78]. And at frequencies lower than 10 GHz the capacitive switches are not useful due to their weak isolations. The one of ways to overcome this disadvantage is adding of a short section of a high impedance transmission line between the fixed-fixed beam and the ground plane, so that the series resonant frequency can be shifted down to the X-band [79]. However an increased inductive loading leads to the reduction of the bandwidth.

1.1.3 MEMS Simulation and Design Tools

The interdisciplinary MEMS switch nature requires a very tight coupling between the electrical and mechanical domains. One-, two- and three-dimensional simulations with various accuracy levels have been used to help understanding and characterization of switches [80-84]. Simulation of MEMS plays an increasingly important role. The motivation here is similar to that of the simulation of purely electronic VLSI circuit: before fabricating a prototype, one wishes to virtually build the device and predict its behavior [3]. Many physical aspects, such as mechanical, electrical, thermal and electromagnetic, must be comprised in the simulation of RF MEMS switches. All these aspects interact with each other and have influence on each other. Therefore, the problem of simulation is rather difficult and complex. Two approaches are used in MEMS electromechanical simulation software. The first one is system level (or behavioral or reduced order or lumped parameter) modeling and the second one is finite element modeling (FEM). The concept of the system level modeling is that the device can be described by a set of ordinary differential equations and nonlinear functions at a block diagram level [3]. The most popular modeling tools, which use this approach, are Simulink, which is a toolbox within Matlab [85], Spice [86], VisSim [87] and Saber [88]. The finite element modeling approach can predict mechanical and nonmechanical responses to a load, such are force, moment, temperature, electromagnetic field and any other loading applied to a body. The simulating component is divided into small, discrete elements which interact with each other at the connected nodes. FEM results in a more realistic simulation than system level modeling, but it requires more computational resources. Well known FEM simulation software tools are: CoventorWare [89], Intellisuite [90], ANSYS [91], ABAQUS FE [92], MEMSCAP [93] and several other simulators. In this thesis, ANSYS Multiphysics simulation tool has been used for electromechanical analyses of the RF MEMS switches.

ANSYS FEM Electromechanical Analysis of RF MEMS Switches

The ANSYS FEM simulator introduces two different methods for the solution of the electrostatic-structural problem. The first method is based on the sequential coupling algorithm [94, 95]. It allows to combine the results of single field simulations for solving the coupled field model. In the case of an electromechanical problem, electrostatic and mechanical structural domains are solved sequentially. The coupling between both domains is realized by the load vector which represents the electrostatic force acting upon the boundaries of the structural elements. In ANSYS, each domain is described by a database file co-called physics environment [91]. In the electromechanical analysis the interaction between both, the electrostatic environment and the structural environment is performed by the transfer between two corresponding databases. The electrostatic problem is based on solving Laplace's equation in different homogenous regions. By solving this equation, the potential distribution in the surrounding environment and on the conductor surfaces can be determined and, thus, the electrostatic force between the two conductors can be calculated. The next step is to solve the structural problem in the structural environment. The actually deformed shape of the membrane under acting of the electrostatic force is obtained following the plate/shell theory [71-73]. Then, the structural domain is switched back to the electrostatic environment updating the electrostatic mesh. The iterative process proceeds until a convergence between two environments will be reached. The second method to realize the electrostatic-structural problem in ANSYS environment is the lumped or reduced order method. This method is usually strongly coupled and considered to be the fastest with respect to the convergence time perspective [96, 97]. It can be implemented using lumped transducer elements, which can eliminate the shortcoming of the sequential method. Transducer elements are a special concept for direct coupling of different physical environments. This element stores electrostatic energy and transforms it into mechanical energy and vice versa. Input data for the transducer element is a voltage applied to the opposite nodes; and from electrostatic field solution a capacitance-displacement relationship can be obtained. Compared with the sequential coupling method 3-D electrostatic elements, which represent the surrounding environment (air between two conductors), are replaced by a set of transducer elements. Thus, a reduced order modeling (ROM) of a coupled electrostatic-structural system can be performed.

As shown in [98], ANSYS produces results that are almost identical to these obtained by other simulators.

1.1.4 Fabrication of RF MEMS Switches

RF MEMS devices and structures can be fabricated using conventional integrated circuit process techniques, such as lithography, deposition, and etching, together with a broad range of specially developed micromachining techniques [3]. The standard CMOS processes, such as oxidation, chemical vapour deposition (CVD), epitaxy, physical vapour deposition (PVD), lithography, dry and wet etching, diffusion, and ion implantation are used for MEMS fabrication. Some of these standard processes have been modified for MEMS fabrication, e.g. the use of thick photoresist, greyscale lithography, or deep reactive ion etching (DRIE).

The materials used in RF MEMS fabrication are all those related to integrated circuit processing. They include epitaxial, polycrystalline, or amorphous silicon, silicon nitride, silicon dioxide, deposited by CVD, or a variety of metals and metallic compounds, such as *Cu, W, Al, Ti, Cr*, and *TiN*, deposited by PVD processes. Optical lithography and spin-on technologies are used for deposition and structuring of standard organic polymer photoresists or polyimides with thickness up to a few micrometers used as a sacrificial layer in RF MEMS fabrication. Additional metals, metallic compounds and metallic alloys such as *Au, Ni, ZnO, SnPb*, deposited by PVD, CVD, cosputtering or electroplating are widely presented in the literature as materials for RF MEMS fabrication [26, 29, 99, 100].

The critical step in RF MEMS switch fabrication is the development of a low-stress thin film process for the membrane material (*Al, Au, Ni*) [39]. Deposition conditions have to be found to form membranes with a low biaxial residual stress and a low stress gradient in the vertical direction. Otherwise, the membrane can be deflected from the desired position by several microns. It leads to a significant change in the bias voltage or even to switch failure. A lot of studies are presented in literature, which theoretically explain the mechanisms of these stress phenomena [101,102] and experimentally measure their effects [74, 103, 104]. However, in general thin film stress is complicately to be treated and strongly depends on the fabrication process conditions. As shown in literature [70, 104], only a micromachining process resulting in tensile residual stress in the thin metal film can be used for manufacturing of MEMS switches. Several approaches have been proposed in the literature to achieve a low stressed thin metal membrane. On of them is based on the formation of holes in the membrane in order to reduce the effective Young's modulus of the structure [105]. But this approach can result in a reduction of the effective down-state capacitance areas. The second way is based on modifying the out-of-plane geometry of the membrane (corrugated membranes) so that the structure becomes much more compliant [29, 104, 106]. Both approaches can also be implemented together.

Conventional dielectric films used in the RF MEMS switch fabrication are silicon oxide and silicon nitride deposited by plasma enhanced chemical vapor deposition (PECVD). Due to better electrical properties with respect to silicon dioxide, silicon nitride deposited by electron cyclotron resonance (ECR) PECVD has been utilized in this study. The main properties of silicon nitride as a dielectric layer for RF MEMS capacitive switches are: high breakdown voltage, relatively high dielectric constant, low surface roughness and low trap density. These characteristics strongly depend on the *Si/N* ratio and the hydrogen contents in the deposited films [107-110]. The ECR-PECVD method allows to reach these requirements and has some advantages over the conventional RF-plasma process. That includes a low deposition pressure leading to a good uniformity, a low process temperature, a reduced process contamination, and a potentially low damage density deposition [107-110]. As has been investigated in [111] the low temperature silicon nitride has a lower dielectric charging than the high temperature deposited films and the charging increases as the film thickness increases.

1.2 CPW Filters

1.2.1 CPW Lines and Conventional CPW Filters

Coplanar waveguides (CPW) are a type of planar transmission line used in microwave integrated circuit (MICs) as well as in monolithic microwave integrated circuits (MMICs) [112]. The major conception of these transmission lines is their uniplanar nature, which means that all of the conductors are only on one side of the substrate. The conventional CPW on a dielectric substrate supports a quasi transverse electromagnetic (TEM) mode of propagation, and consists of a center strip conductor with semi-infinite ground planes on either side. Main advantages of the CPW over conventional microstrip lines are: simple manufacturability; possible surface mounting of active and passive devices [113-117]; abandonment of wraparound and via holes; and reduced radiation loss [112]. Moreover, the characteristic impedance is determined by the ratio of the center conductor width to the gap width [112]. This all makes CPW eminently suitable for MIC as well as MMIC applications.

Filters are essential components of most microwave and mobile systems [118]. Such systems require compact filter structures, which can effectively suppress unwanted out-of-band signals. Design of microwave and millimetrewave filters based on coplanar waveguide (CPW) transmission lines offers some advantageous compared to microstrip lines such as: easier realisation of shunt and series connections, avoiding via holes and providing lower frequency dispersion. Up to now, numbers of CPW filters have been reported in literature. They are usually realised using distributed transmission line stubs which occupy relatively large area [119-123]. Several approaches have been proposed to reduce the stub size: bent lines [124, 125], meander stubs [126, 127] and capacitive loading [128, 129]. End-coupled coplanar filters are realised by cutting gaps in the center line [130], but the gap does not satisfy the filter requirements due to a low capacitance. Also, the method of coupling is the inductively-coupled lines approach to realize a shunt inductively-coupled CPW filter, which has good RF characteristics such as low insertion loss and good stop-band rejection [131]. An alternative approach to filter design is the use of DGS resonators.

1.2.2 Defected Ground Structures

Defected ground structures (DGS) have promised an increasing potential for implementation in different applications: MIC, MMIC, and RFIC [132-151]. These structures have etched defects in a metallic ground plane like photonic band gap (PBG) structures [152-154]. These defects disturb the shielded current distribution in the ground plane exciting a parallel propagating mode. This disturbance can change the characteristics of a transmission line such as the effective line capacitance and inductance [132]. The DGS can not only significantly increase the characteristic impedance of a microstrip line, but also improve the stop-band performance by rejecting higher order pass-bands. It leads to a reduction of resonant structure sizes. Most of the applications of DGS and PBG structures, which have been published in the recent years, are in microstrip implementation [132-145]. Therefore, these devices require a precise fabrication process on both substrate sides and an adequate packaging to keep an air-gap between the ground and the package box. In such a way, CPW can be a good compromise for DGS structures. Additionally, they are less sensitive to substrate thickness and substrate dielectric constant compared to microstrip structures [155]. To the author’s knowledge, few applications for DGS on CPW circuits have been reported [145-151]. Different defect shapes in both microstrip and CPW implementations exist in the literature: dumbbell [134], periodic [140, 145, 150], fractal [135], circular [152], spiral [151], T-shaped [141], L-shaped DGS [146], arrowhead [142, 143], and different other geometrical shapes. Several examples of DGS are shown in Figure 1.7.

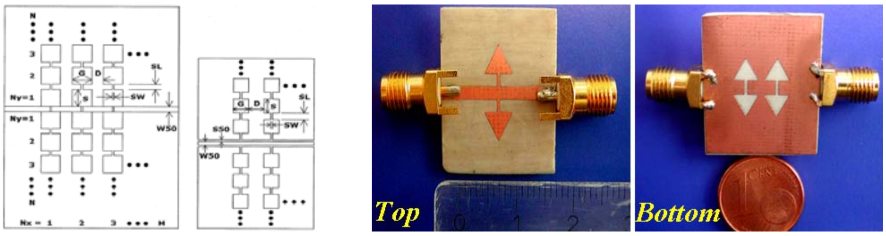

a) b)

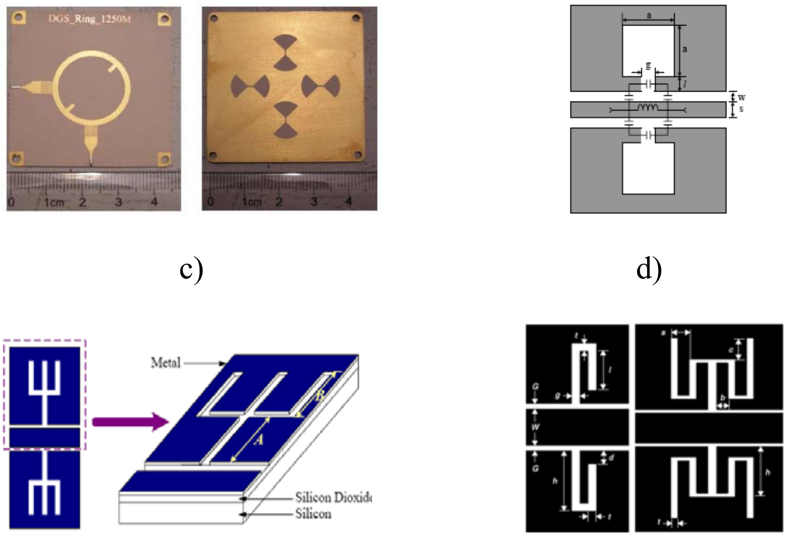

c) d)

e) f)

Figure 1.7: Examples of DGS: (a) schematic diagram of microstrip and CPW transmission lines with vertical periodic DGS [145], (b) photograph of fabricated DGS LPF using arrowhead DGS and multilayer technique [143], (c) photograph of the microstrip ring filter with patterned ground plane [144], (d) schematic view of the lattice shape DGS on CPW [147, 156], (e) fork-shaped DGS on CPW [149] and (f) L-shaped DGS on CPW [146].

Analytical Model for DGS

The conventional lumped-element resonator generally works well at low frequencies while it has several problems at microwave frequencies [157]. The main of them is a limited range of values of inductors and capacitors at microwave frequencies. Moreover, the distance between the resonator components can not be neglected at microwave frequencies. Transformation of lumped elements to transmission line sections can be carried out by using Richard's transformation, while a separation of the filter elements by transmission line sections can be provided by Kuroda's identities [157].

A parallel *LC* equivalent circuit (see Figure 1.8 (b)) represents the DGS slot; the geometrical dimensions and the shape of the defect affect the lumped-element parameters [132]. Any shape of the DGS slot with the same area can be used to obtain the same equivalent inductance at the cut-off frequency [132]. However, the performance of the complete circuit strongly depends on shape, size and orientation of a DGS slot, which provides the band-reject (band-stop) characteristic [132, 158]. A DGS basically consists of large defects and a narrow connecting slot. Large defects result in an equivalent inductance, while the connecting slot represents an equivalent capacitance [132]. Figure 1.8 (a) shows the dumbbell shape DGS slots which are symmetrically etched on the ground planes on both sides of the CPW center line. The one-cell DGS can provide cut-off and resonance frequencies due to the slow-wave effect, as shown in Figure 1.8 (c).

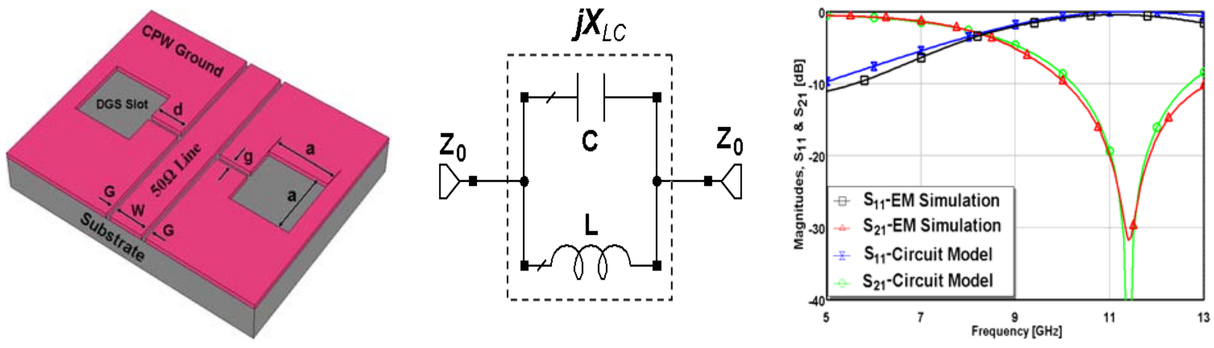

a) b) c)

Figure 1.8: Schematic view of the dumbbell shape DGS unit section (a); its equivalent circuit (b); and frequency response of the DGS unit section (c).

The simulation result clearly reveals that the DGS provides a one-pole low-pass filter characteristic [157]. The slow-wave effect changes the propagation constant of the transmission line by an increased inductive loading corresponding to the DGS slot. Therefore, the compactness of the resonance structure can be increased by reducing the line length.

At frequencies below the resonance frequency the DGS slot behaves as an increased effective inductance of the CPW line. The cut-off frequency is mainly controlled by the DGS slot head area. The frequency response of the DGS slot can be described using an equivalent circuit extraction method. The equivalent circuit will simultaneously exhibit low-pass and bandstop filter performances. The 3-dB cut-off and attenuation pole frequencies can be extracted from EM simulation or from the measured frequency response. The equivalent inductive reactance can be easily derived from the maximally flat Butterworth low-pass response using a one-pole prototype element [157]. Then, the parallel capacitance can be extracted from the resonance frequency value. The equivalent reactance value of the one-cell DGS unit can be expressed as follows [132, 157, 158]:

$$jX_{LC} = \frac{j\omega L / j\omega C}{j\omega L + 1/j\omega C} = \frac{j\omega L}{1-\omega^2 LC} \tag{1.31}$$

$$\omega_0^2 = \frac{1}{LC} \tag{1.32}$$

$$X_{LC} = \frac{1}{\omega_0 C\left(\frac{\omega_0}{\omega} - \frac{\omega}{\omega_0}\right)} \tag{1.33}$$

where L and C are the inductance and capacitance of the equivalent circuit model, respectively, and ω_0 is the resonance angle frequency. The value of the parallel effective capacitance in pF of the 50-Ω CPW line can be calculated by using the prototype element of the one-pole response network, which is shown in Figure 1.9, as follows [132, 157, 158]:

$$C = \frac{\omega_c}{Z_0 g_1(\omega_0^2 - \omega_c^2)} = \frac{5 f_c}{\pi(f_0^2 - f_c^2)} \quad [\mathrm{pF}] \tag{1.34}$$

Rearranging (1.32), the parallel effective inductance in nH is defined as [158]:

$$L = \frac{250}{C(\pi f_0)^2} \quad [\mathrm{nH}] \tag{1.34}$$

where f_c and f_0 are 3 dB cut-off and attenuation pole frequencies in GHz, respectively, Z_0 is the characteristic impedance of the CPW, and $g_1 = 2$ is a tabulated element value for a maximally flat low-pass filter prototype. The comparison between EM and circuit model simulations, obtained by the commercially available method-of-moment electromagnetic (MoM EM) simulators Sonnet [159] and Microwave Office [160], is depicted in Figure 1.8 (c). The resonance magnitude of the circuit model simulation is infinite because the lumped-element model does not take into account the radiation losses in the DGS. Due to a bandstop response of the DGS most of researches are performed to realise CPW low-pass filters (LPF).

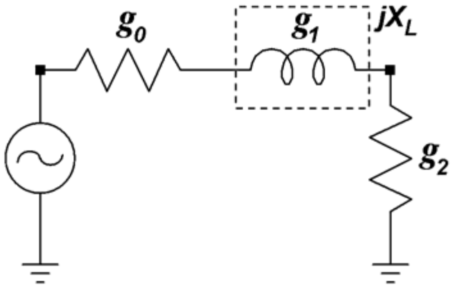

Figure 1.9: One-pole prototype low-pass filter.

1.3 Tunable MEMS Filters

The subject microwave filters is quite extensive due to the importance of these components in practical systems and the wide variety of possible implementations. Tunable microwave devices should offer services which provide flexibility and scalability that meet the system requirements. For instance, a control system of a tunable filter should have a minimum influence on transmission and reflection characteristics. Several different tuning methods have been investigated in the past as outlined in [161]. Most of them are based on varactor diodes [162], paraelectric capacitors [163], or micro-electro-mechanical systems capacitors [164-170]. However, filters which utilize the first two tuning elements have a low Q- factor due to a high series resistance of the diodes. MEMS technology offers promising opportunities to fabricate filter structures with good parameters, like narrow band width, low loss, and good stability.

For many applications, the tunable filters must have a compact size and a small degree of tunability and must be realized in CPW configuration. To our knowledge only several tunable filters, based on CPW DGS and MEMS switches are presented in literature [171, 172]. Both tunable bandstop filters are realized by introducing MEMS capacitive switches periodically located between DGS providing the capacitance loading. In [171] a conventional rectangular DGS slots is used. This filter reveals a tuning range from 19.0 GHz to 17.3 GHz with lower pass-band insertion loss of 0.7-2.2 dB and a bandwidth of 5.5 GHz. However, losses in both pass-bands are very high. A filter presented in [172] is based on a fractal DGS etched on the ground plane as well as on the signal line. This BSF offers a tuning range from 17.6 GHz to 16.5 GHz with insertion loss of 1.7-2.5 dB. This approach allows to increase the structure compactness and improves the pass-band performance. An other approach to combine DGS structures with MEMS switches realising a reconfigurable resonator is proposed in [173]. In this work, series MEMS switches are located directly on the ground plane and provide the control of a number of rectangular DGS cells.

1.4 Dissertation Objectives and Organisations

The objects of the dissertation are:

- To model and simulate accurately the mechanical behaviour of the fixed-fixed beam micro-bridges under the effect of electrostatic forces and residual biaxial tensile stress and predict their actuation-voltage and stress intensity distribution using the finite elements method (FEM).
- To design and optimise low actuation-voltage high isolation and high reliability RF MEMS switches using commercially available FEM and full-wave 2.5-D planar MoM

(method of moment) electromagnetic simulation tools, and to describe the electromagnetic behaviour of the proposed switches using lumped-element equivalent circuit models.

- To fabricate RF MEMS switches based on fixed-fixed beam configuration and optimize every fabrication step using standard CMOS technology, to optimize the deposition process of the conventional dielectric films, such as silicon nitride, using the low-temperature plasma enhanced chemical vapour deposition (PECVD) method, to find the optimal etch (wet or dry) process parameters for the metal, photoresist and the dielectric films; and finally to compare the measured results with the theoretical calculated and simulated results.
- To design passive, high performance RF filters in CPW implementation using the conventional design approach and the approach based on the defected ground structure (DGS) method. To fabricate the proposed HF structure and compare the measured response with the simulated one.
- To design and investigate the tunable RF MEMS switch controlled quasi defected ground structure (DGS) microwave filter using a full-wave 2.5-D planar MoM electromagnetic simulator and a lumped-element equivalent circuit model.

The organization of the dissertation is as follows. Chapter 1 begins with an introduction and basic considerations for micro-electro-mechanical systems. It discusses the state-of-the-art of RF MEMS switches, DGS and passive and tunable RF filters. It presents the contributions of the thesis to the RF MEMS and the CPW filter topics.

Chapter 2 deals with the 2-D and 3-D coupled electrostatic-mechanical FEM models for the fixed-fixed beam micro-bridge structure. Two methods to solve the electrostatic problem will be presented. The first one is the sequential coupling algorithm; electrostatic and structural aspects are solved sequentially. The second method of the solution of the electrostatic-structural problem is the lumped or reduced order model. This model is usually strongly coupled and is considered to be the fastest from the convergence time perspective.

Chapter 3 is dealing with the modeling, the simulation and the optimization of low actuation-voltage, high isolation and high reliability RF MEMS shunt-capacitive and shunt-resistive switches for *L*-, *S*-, and *X*-band applications. The new configuration of the movable membrane based on the flexure-flexure suspension will be proposed to increase the effective areas of the actuation pads, and thus to reduce the actuation-voltage. On the other hand, the contact areas between the movable membrane and the CPW center conductor have been decreased to reduce an insertion loss of the switch in the ON-state. Two approaches have been used to increase the OFF-state isolation of the shunt-capacitive switch. In the first one a larger capacitive structure is formed directly on the center conductor by depositing a thin metal film on a dielectric layer which covers the center line. The second approach implements large shunting capacitances on the ground plane under the suspension posts. The proposed RF MEMS switches will be investigated with FEM electromechanical simulations to define the actuation-voltage and with a 3-D full-wave EM simulator to define the frequency responses of the switches. The lumped-element equivalent circuit simulations will also be used to describe the switch electromagnetic properties.

In chapter 4 a fabrication process of RF MEMS switches based on a fixed-fixed beam configuration is described. High-resistivity (> 4.0 kΩ) silicon has been used as substrate material. Each fabrication step being compatible to standard CMOS technology will be investigated in details. Low temperature deposition processes of dielectric films like silicon nitride have been carried out by using ECR-PECVD using mixtures of Ar, N_2 and SiH_4 as precursors. The deposited films have been investigated with ellipsometry and X-ray photoelectron spectroscopy (XPS). Metal-insulator-metal (MIM) capacitors have been fabricated in order to investigate the electrical properties of the dielectric films. The conventional chemical wet etch process has been used to form CPW line while RIE etching has been utilized to realize the movable metal parts of the RF MEMS switches. Finally, the fabricated switches have been tested and the measured results have been compared to the electromechanical and electromagnetic simulations. Good agreements have been reached.

In chapter 5 the designs of microwave coplanar filters are introduced. The conventional methods of the filter implementation have been modified to improve the filter characteristics. Serpentine shape shunt/open-stubs are proposed to increase the inductive and capacitive loading of the CPW line, therefore, the shift of the operation range of the bandpass/bandstop filters to lower frequency without any enlargement in filter dimensions. The DGS approach is used to realize the coplanar low-pass and ultra wideband (UWB) low-pass filters with compact size and high performance. Quasi-fractal DGS slots have been investigated with EM and lumped-element equivalent circuit simulations and, then, the obtained results have been confirmed by measurements.

The design of tunable coplanar quasi-DGS bandpass filter for K-band applications, for instance in automotive and transceivers systems, is introduced in Chapter 6. The proposed structure is composed of $\lambda/4$ open-end stubs resonators coupled by the gap capacitance and external metal stubs on both sides of the CPW. A method to control the resonance frequency and bandwidth has been developed by creating an ohmic contact between the ground plane and external metal plane in a certain location. Eight RF MEMS series-resistive switches form the control system of the tunable bandpass filter. The proposed BPF has been designed and described using the full-wave EM MoM simulator and lumped-element equivalent circuit model.

In Chapter 7 this work is concluded.

Chapter 2

FEM Electromechanical Analysis of Fixed-Fixed Beam MEMS Switches

This chapter presents the coupled finite element model (FEM) electrostatic-structural analysis of fixed-fixed beam parallel plate microstructures using the commercial FEM simulator ANSYS Muliphysics 9.0 [91]. The two- and three-dimensional (2-D and 3-D) models will be investigated in order to determine the pull-down voltage and the stress in the membrane. Two different algorithms will be implemented to solve the electrostatic problem. Additionally, the effects of the residual stress due to the fabrication process and the axial force resulting from the mechanical deformation of the beam are taken into account in this study.

2.1 Sequential Coupling Algorithm

One of the most accurate methods to analyze coupled electrostatic-structural problems using full 3-D FEM simulations is the sequential coupling approach. It provides a high accuracy level, but requires a lot of computational resources. For the sequential coupling analysis ANSYS can use an *ESSOLV* macro which solves the coupled electrostatic-structural problem [174].

The sequential coupling analysis starts with the generation of an electrostatic physic file, which describes the electrical potential distribution when a voltage is applied to the conductors. The problem is solved by Laplace's equation which is given by:

$$\nabla^2 V = \frac{\partial^2 V}{\partial x^2} + \frac{\partial^2 V}{\partial y^2} + \frac{\partial^2 V}{\partial z^2} = 0, \qquad (2.1)$$

where V is the potential distribution in the electrodes surrounding medium. The known boundary conditions are: $V = V_a$ is a voltage applied to the membrane (upper electrode); and $V = 0$ V is the potential of the bottom electrode. This equation is suitable for any geometry of MEMS devices.

Figure 2.1 shows the parallel plate model which will be verified using the ANSYS simulation platform and the result will be compared with the theoretical model described in chapter 1.

The initial gap high g_0 is assumed to be uniform in the structure. The upper plate is a moveable electrode which is clamped in two opposite sides while the bottom plate is a fixed electrode, as shown in Figure 2.1 (b). Both electrodes are enclosed in an air box (not shown in the figures). The electrode material used for this simulation is aluminum. The dimensions and the materials properties of the problem are listed in Table 2.1. It considers a wide beam ($w_m \geq 5t_m$) which exhibits plane-strain conditions [74]. Therefore, the key options for the structural elements in ANSYS must be set to allow the plane-strain modeling.

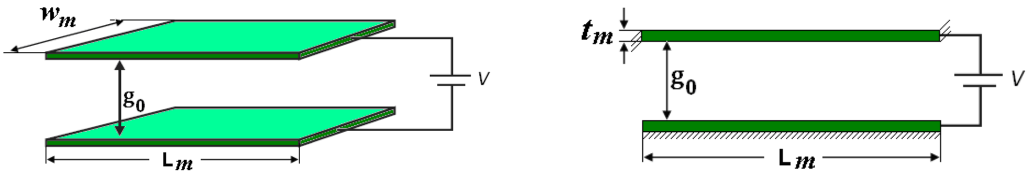

a) b)

Figure 2.1: Verification parallel plate model: (a) 3-D view and (b) cross-section (2-D).

Table 2.1 Verification parallel plate model dimensions and material properties

Length of the plates,	L_m (µm)	300
Width of the plates,	w_m (µm)	100
Initial gap height,	g_0 (µm)	2
Thickness of plates,	t_m (µm)	2
Young's modulus of *Al*,	E (GPa)	70
Poisson's ratio of *Al*,	v	0.35

Usually, in the electrostatic analysis the electric field must be unbounded. Therefore the effect of the open environment has to be included in the electrostatic model for high accuracy. But in practice, the electrostatic model cannot be infinitely extended. There are two possibilities to model the effect of an open field using ANSYS environment. The first one is extending of the free space region, and the second is using infinite elements. In the case of a small initial gap (in ANSYS $L_m > 20t_m$), where a fringing field has a minimum effect, an extension of the free space is more efficient. For models with a large initial gap ($L_m < 20t_m$), for which fringing has to be taken into account, the infinite elements are required. A fringing field builds up in the perimeter of the parallel plates. Since all problems encountered in this study are small gap problems, the method of the free space region extension is used. In this method an outer edge of the air box must be modeled with Neumann boundary conditions which assume that current flows only parallel to the box edges [175]. On the other hand, an air-metal interface is modeled with Dirichlet boundary conditions where the electric field is perpendicular to the conducting surface [175]. For a higher accuracy level in ANSYS the free space must be extended approximately by 4 times of the initial gap height.

Figure 2.2 (a) shows a scaled view of the right side of the meshed 2-D fixed-fixed beam structure. Due to a structure symmetry in both *x*- and *y*-directions only a quarter of the 3-D model has been modeled, as shown in Figure 2.2 (b). 2-D, 8-nodes triangular charge-based electrostatic elements, *PLANE121*, have been used to mesh the air region in the 2-D model, while for the 3-D model, meshing of the surrounding medium has been implemented by using the 3-D, 20-nodes rectangular charge-based elements *SOLID122* [174].

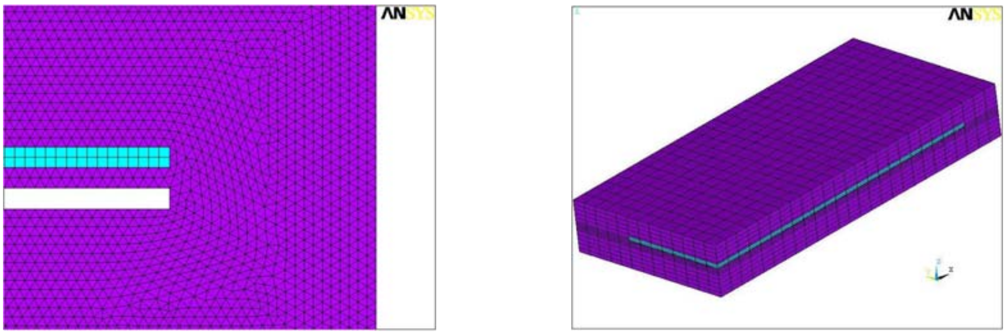

a) b)

Figure 2.2: Enlarged meshed model views: (a) 2-D model and (b) 3-D model.

A bias voltage, applied to the moveable electrode, is changing from zero volt to a value at which a convergence between the electrostatic and the structural domains does not happen. It should be noted that the membrane can be pulled through the bottom electrode, because the contact problem has not been modeled in this study. But it plays no role, since the simulator cannot identify a stable solution until the applied voltage is less than the pull-down value. The enlarged contour plots of the applied voltage of 28 V surrounding the deformed plates for the 2-D and 3-D models are shown in Figure 2.3. This voltage is very close to the pull-down voltage and almost a maximum deflection can be obtained.

A 2-D contour plot of the electric field strength of the half membrane and at the right side of the structure is shown in Figure 2.4. As expected the maximum magnitude is in the gap region where the maximum displacement occurs, namely, at the membrane center. The maximum electrical field is 19.515 V/µm corresponding to a gap height of 1.44 µm and a bias of 29 V. The fringing field is shown in Figure 2.4 (b). In the case of the 2-D model the fringing field can be observed at both opposite fixed edges of the membrane. It is obvious, that in the case of the 3-D model, the fringing field is present at every side of the membrane. Figure 2.5 shows a 2-D vector plot of the electric field at the right side of the membrane, where the fringing field effect is observed, and one half of the membrane. The vector set in Figure 2.5 determines the electric field direction.

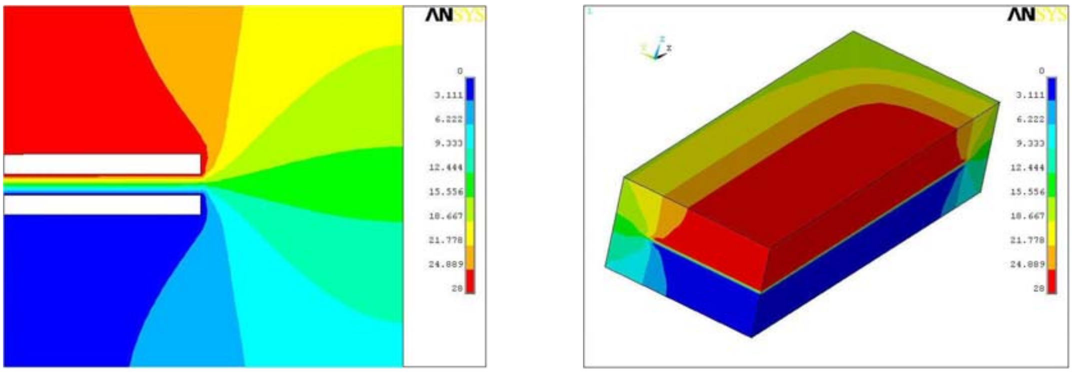

a) b)

Figure 2.3: Voltage contour plot for the structure with applied bias voltage of 28 V: (a) right side of the 2-D model and (b) quarter of the 3-D model.

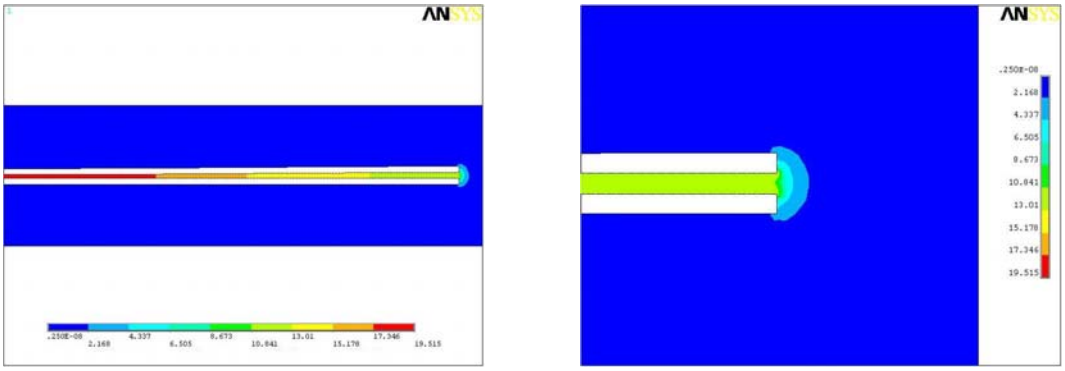

a) b)

Figure 2.4: Contour plot of the electric field strength in V/μm for the 2-D structure: (a) one half of the membrane and (b) structure right side.

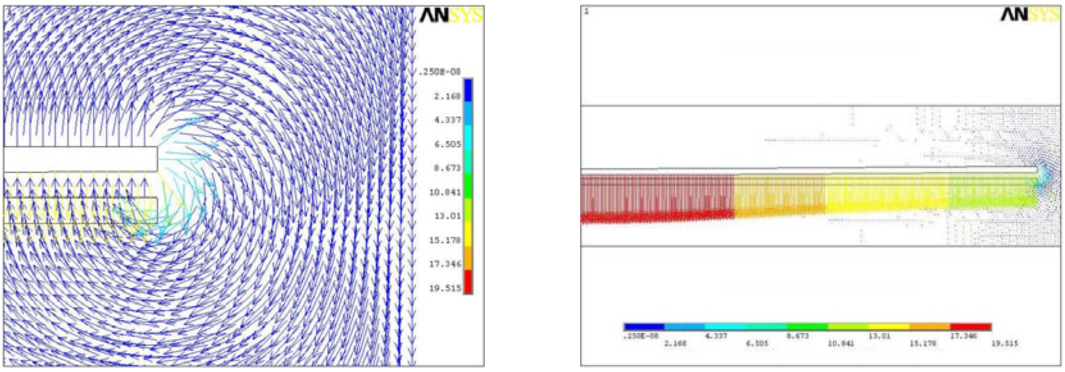

a) b)

Figure 2.5: Vector plot of the electric field strength in V/μm for the 2-D structure: (a) right side and (b) one half of the membrane.

The 2-D vector plot of the electrostatic force distribution along the membrane length is shown in Figure 2.6. The vector length is linearly related to the magnitude of the force. It is obvious that the force increases as the membrane deflection is increased (from the fixed ends to the center of the membrane) and has its highest value at the center of the bridge where the maximum deflection occurs.

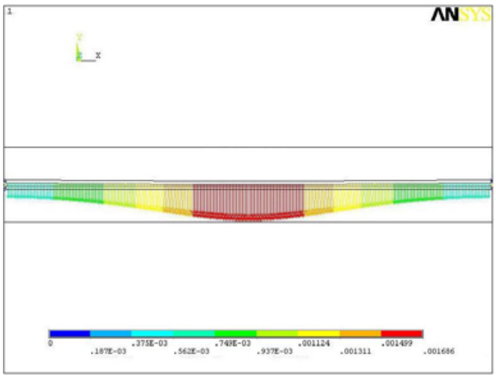

Figure 2.6: Vector plot of electrostatic force distribution in µN for the 2-D model.

The structural model is based on solving the plate equation, which describes the behaviour of the plates (or shells) under the applied pressure and is given by [71]:

$$\frac{\partial^4 u}{\partial x^4} + 2\frac{\partial^4 u}{\partial x^2 \partial y^2} + \frac{\partial^4 u}{\partial y^4} = \frac{P(x,y)}{D} \quad , \tag{2.2}$$

where u is the transverse deflection in z-direction, $P(x, y)$ is the pressure (N/m^2) (in our case the electrostatic force obtained from the electrostatic simulation), $D=Et_m^3/12(1-v^2)$ is the flexural rigidity of the plate, where E is the Young's modules, t is the bridge thickness, and v is the Poisson's ratio of the membrane material. For the fixed edges, the deflection in all directions is assumed to be zero. Taking into account that the center of the membrane is given by $x = 0$ and the fixed edges are at $x = -L_m/2$ and $x = L_m/2$ (L_m is the length of the membrane), the boundary conditions are:

$$u = 0\Big|_{x=\pm L_m/2} \tag{2.3a}$$

$$\frac{\partial u}{\partial x} = 0\Big|_{x=\pm L_m/2} \tag{2.3b}$$

Figure 2.7 shows the deflection of the bridge structure in micrometers obtained with the 2-D and 3-D models under an applied bias of 28 V. Figure 2.7 (a) shows the undeformed membrane and deformed structure directly below. The maximum displacements of the bridge structure with respect to its initial position are 0.565 µm for the 2-D model and 0.677 µm for the 3-D model. It should be noted that the free edges of the membrane in the 3-D model are stronger deformed due to a probability of motion in all directions as can be seen in Figure 2.7 (b). In Figure 2.7 the deflection of the membrane is magnified by a factor of 20 for an easier visibility of the displacement.

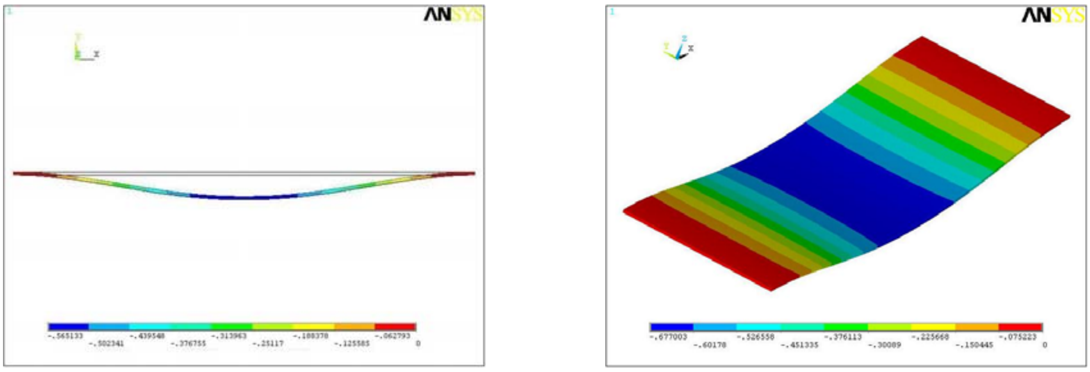

a) b)

Figure 2.7: Contour plot of the deformed membrane with the applied voltage of 28 V: (a) 2-D model and (b) 3-D model.

The voltage has been varied from 0 V until the pull-down voltage has been found. At the pull-down voltage the solution becomes unstable and the simulator cannot find a convergence between electrostatic and structural energies. A plot of the center deflection of the bridge versus the applied voltage is shown in Figure 2.8.

The maximum deflection of the center of the fixed-fixed beam before the membrane collapses onto the bottom electrode was 0.774 µm at a voltage of 29.1 V for the 2-D model and 0.732 µm at 28.4 V for the 3-D model, respectively. This corresponds to a 39% and 37% center deflection of the original gap for the 2-D and 3-D simulations, respectively. For the 2-D case, the convergence between the two physical environments has been reached with an applied voltage of 29.1 V, but for 29.2 V a solution can not be found. Therefore, the pull-down voltage is lying between these two voltage values. Using the *CMATRIX* macro of ANSYS and 0 V for the applied voltage the capacitance values of the 2-D and 3-D parallel plate structures are 13.47 pF and 14.1 pF, respectively. According to Eqn. 1.10 the capacitance value of a simple parallel plate capacitor formula is 13.28 pF. It can be seen that both, theoretical and simulated capacitance values of the 2-D model are very close (1.4% difference) to each other because the fringing field is very small. Therefore, it can be concluded that the simulator is valid to predict the MEMS structure behavior. Figure 2.9 shows the capacitance of the parallel plate structure versus the applied voltage simulated by using the *CMATRIX* macro. The pull-down voltage obtained by using the approximation in Eqn. 1.14 has been found to be 29.06 V.

This is very close to the results calculated by ANSYS (29.1 V - 29.2 V). In the case of the 3-D model, the initial capacitance value is 6.2% higher than the theoretically calculated one. Therefore, the pull-down voltage is lower than the values obtained by the 2-D simulation and the theoretical prediction. This is due to the fringing field effect at every side of the membrane in the 3-D model. The fringing capacitance amplifies the electrostatic force between the parallel plates; consequently, the maximum deflection before the membrane collapses onto bottom electrode in the 3-D model is also smaller than in the 2-D case.

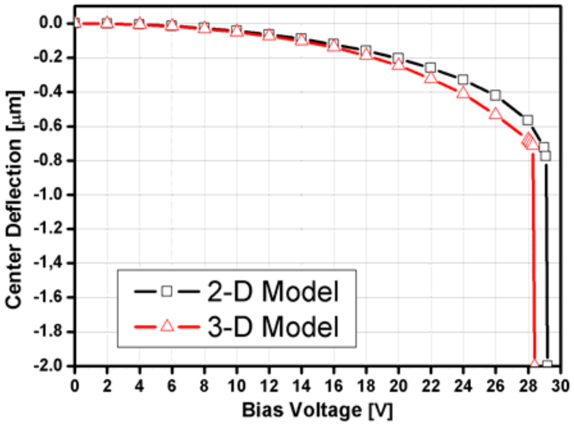

Figure 2.8: Membrane center deflection for 2-D and 3-D models versus applied voltage.

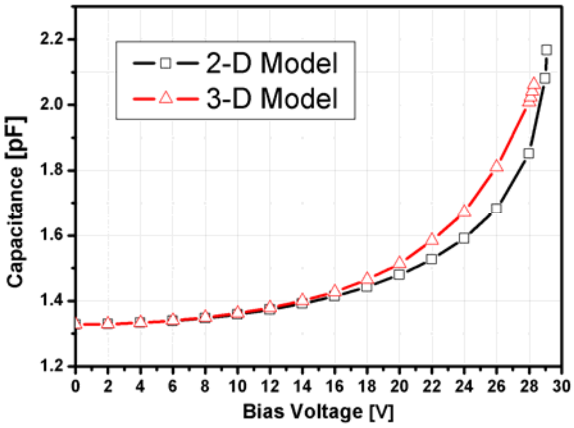

Figure 2.9: Membrane capacitance for 2-D and 3-D models versus applied voltage.

2.2 Lumped or Reduced Order Algorithm

Lumped-element models allow the treatment of a diverse number of analysis types, including pre-stressed modal and harmonic analyses. The Newton-Raphson nonlinear iteration is used to find quickly and robustly a convergence between the electrostatic and the mechanical energies by use of a lumped model. On the other hand, this method has some limitations with regard to geometries where the capacitance cannot be accurately described as a function of a single degree of freedom, usually for the deflection of a comb drive. For small gap problems, like MEMS shunt capacitive switches, the fringing field effect can be neglected; then the capacitance between the electrodes can be practically modeled by a number of parallel connected capacitors. In the ANSYS simulator the electro mechanical transducer generator (*EMTGEN* command) macro can be used to solve the electrostatic-structural problems [174].

The 1-D electromechanical transducer element, *TRANS126,* can realise strong coupling between distributed, lumped mechanical and electrostatic systems, representing a reduced-order model suitable for the use for structural finite element analysis as well as for electromechanical circuit simulation. This element represents the capacitive response of the device for the motion in one direction. The *TRANS126* element calculates a capacitance-displacement relation as [174]:

$$C(g) = \frac{C_0}{g} + C_1 + C_2 g + C_3 g^2 + C_4 g^3 \tag{2.4}$$

where C_0, C_1, C_2, C_3 and C_4 are the polynomial coefficients of capacitance per unit length.

a) b)

Figure 2.10: The ANSYS *TRANS126* element: (a) finite element interpretation, and (b) geometry of the *TRANS126* element.

The finite element interpretation and geometry of the ANSYS' *TRANS126* element is shown in Figure 2.10. The element has two nodes (*i, j*) with two degrees of freedom for each node: displacement in *x*-, *y*- or *z*-direction and electric potential. The gap is calculated as the sum of the initial gap and the difference of the nodal displacement in the direction of the element. The force with the constant voltage is calculated as:

$$F = -\frac{1}{2}\frac{\partial C(g)}{\partial (g)} V^2 = \frac{V^2}{2}\left[-\frac{C_0}{g^2} + C_2 + 2C_3 g + 3C_4 g^2 \right], \tag{2.5}$$

In the case of an electrostatic pressure on an area of the parallel plate structure, each node of the area in an overlapping location is connected to the opposite electrode by a transducer element.

Figures 2.11 show the enlarged meshed structure views of the 2-D and 3-D models. The air space between the electrodes is meshed with transducer elements *TRANS126,* which are shown in the plots as violet lines. In the case of the 2-D simulation, the mechanical solid structures have been meshed with 2-D, 8-nodes structural solid elements *PLANE82.* A key option for this elements has been set so that the structure is modeled using only plane-strain conditions. For the 3-D simulation, solid mechanical parts have been meshed with 3-D, 20-nodes structural solid elements *SOLID95*. Every node of the bottom surface of the movable membrane is connected to the top node of the transducer element. The transducer element matrix has been performed using the *EMTGEN* macro from ANSYS.

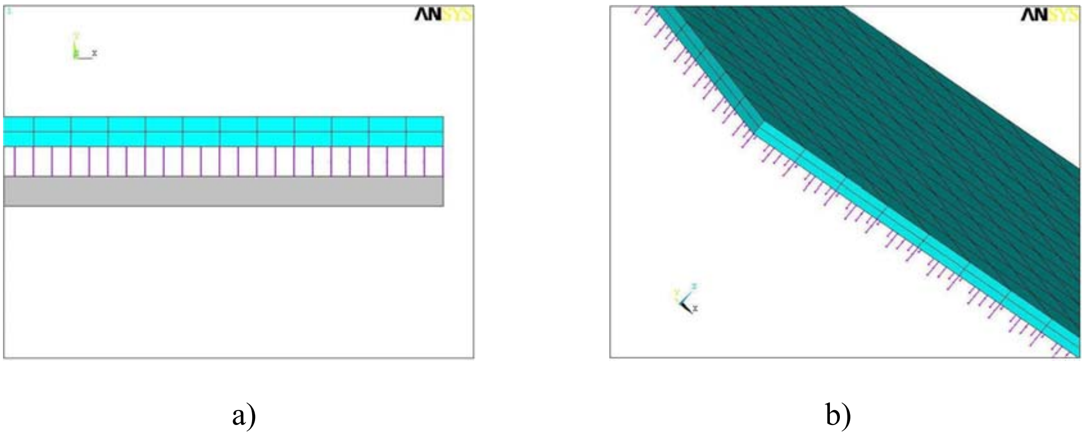

a) b)

Figure 2.11: Enlarged meshed model views: (a) 2-D model (grey box is the bottom electrode), and (b) 3-D model (the bottom electrode is not shown). Violet lines are distributed *TRANS126* elements.

In Figure 2.12 the contour plots of a deformed and an undeformed membrane are shown with transducer elements at the applied voltage of 29 V. The displacement is enlarged by a factor of 20. The length of the transducer elements is equivalent to the displacement value. The voltage has been varied from 0 V up to the predicted pull-down voltage with a step width of 0.2 V. Close to the pull-down voltage the step width is changed to 0.1 V. After the pull-down voltage has been reached the membrane is immediately collapsing to the bottom electrode.

Figure 2.13 shows the plot of the center deflection of the membrane versus the applied voltages for the 2-D and for the 3-D model. Before the collapse occurs the maximum deflections of the center of the fixed-fixed beam were 0.76 μm at 29.45 V and 0.728 μm at 29.1 V for the 2-D and 3-D simulations, respectively.

Table 2.2 summarises the simulation results of the sequential coupling and reduced order algorithms. It can be seen that the simulation results are almost equal. However, the pull-down voltages of the reduced order method are higher because the fringing field effect has not been taken into account.

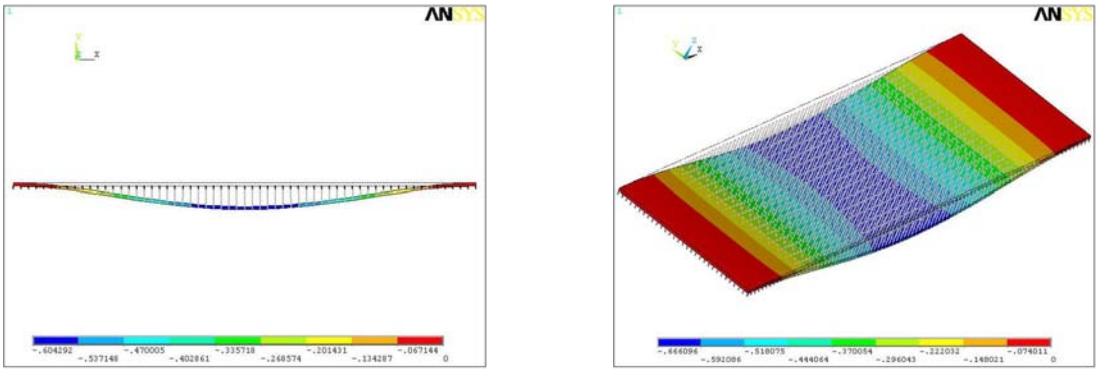

a) b)

Figure 2.12: Contour plot of the deformed and the undeformed membrane with the applied voltage of 29 V: (a) 2-D model and (b) 3-D model.

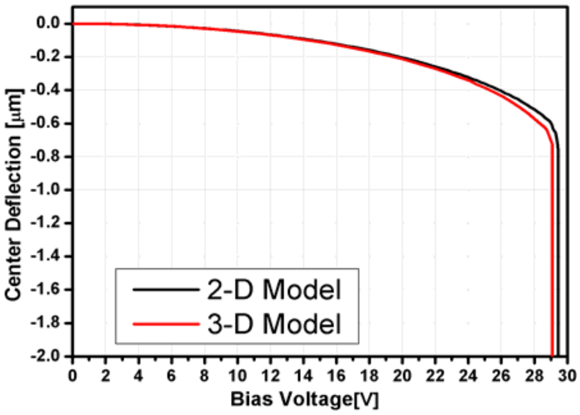

Figure 2.13: Membrane center deflection for 2-D and 3-D models versus applied voltage.

Table 2.2 Simulation results with ANSYS *ESSOLV* and *EMTGEN* macros

	Max. center deflect. before collapse, [µm]		Pull-down voltage, [*V*]	
	2-D	3-D	2-D	3-D
ESSOLV	0.774	0.732	29.1-29.2	28.4
EMTGEN	0.76	0.728	29.45	29.1

2.3 Stress in a Fixed-Fixed Beam

The stress level in the metal membrane has a strong influence on the device reliability. If the stress is too large the device will fail. The stress level should not exceed the material yield strength. In the case of a metal membrane, material can fail plastically so that the metal bridge does not return to its original position after the loading (electrostatic force) has been removed.

Thus, the reliability of the device strongly depends on the stress during device actuation. Therefore, its level should be determined.

The 3-D model of the fixed-fixed beam has been applied to determine the stress level during actuation. The voltage between the metal plates has been chosen to be a little bit lower than the pull-down voltage so that the movable electrode has a maximum deflection of 0.7 µm at the center. Figure 2.14 shows the contour plots of the stress on the top membrane surface in the *x*-, *y*- and *z*-directions, and the stress intensity of the fixed-fixed beam. The maximum stress in the *x*-direction (along the beam length) is 23.6 MPa. This stress concentrates on the edges of the beam, where the bridge structure is connected to the supports, and decreases towards the center of the membrane. It is clear that the fixed edges at the top membrane surface are stretched and at the bottom membrane surface are compressed. But at the center of the membrane, where a maximum deflection is observed, the top surface is compressed and the bottom surface is stretched. The *y*-component of stress has a maximum value of 12.2 MPa. This stress is also concentrated at the fixed edges of the membrane. And as it is for the *x*-component, the top surface at the fixed edges is stretched and the bottom surface is compressed. It can be seen that the middle part of the membrane is almost not stressed. The same situation is observed for the *z*-component of the stress but with a maximum value of 11.1 MPa.

ANSYS can combine all components of stress in order to compare it with allowable values. The stress in the *x*-, *y*-, and *z*-directions is combined into a stress intensity. This value is derived on base of the Tresca failure criterion [91]. The stress intensity can be compared with the ultimate strength, in this case for aluminum, of 55-310 MPa [176]. As can be seen in Figure 2.14 (d), the maximum stress intensity in the membrane is 19.8 MPa. It is more than two times smaller than the ultimate strength for aluminum.

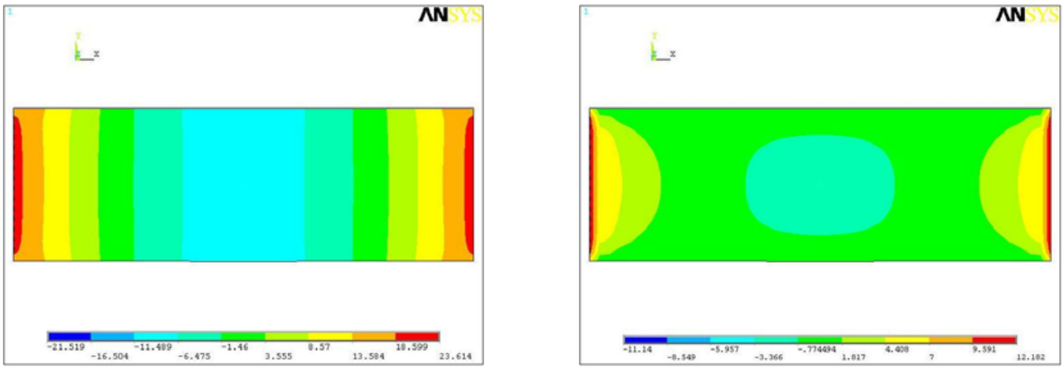

a) b)

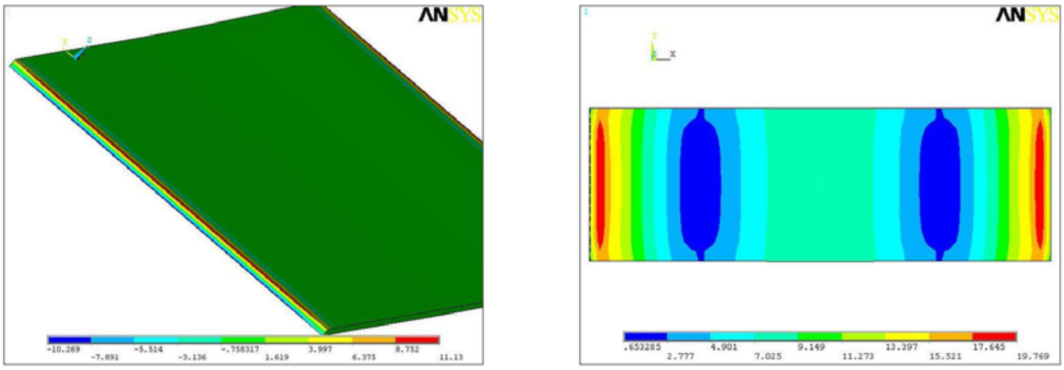

c) d)

Figure 2.14: Contour plots of the stress on the top surface of the deformed membrane (0.7 μm center deflection): (a) S_x component, (b) S_y component, (c) S_z component and (d) stress intensity. The unit of the stress is MPa.

2.4 Effect of Residual Stress on the Pull-Down Voltage

The previous analysis has been performed for the pull-down voltage of the parallel plate structure without any intrinsic residual stress in the metal film. Residual stress, however, is developed during the fabrication of most microstructures and typically ranges from a few MPa to over 100 MPa [103, 176, 177]. Therefore, the effect of the residual stress should be taken into account in MEMS device simulations. In this section, the effect of the tensile residual stress on the pull-down voltage will be discussed.

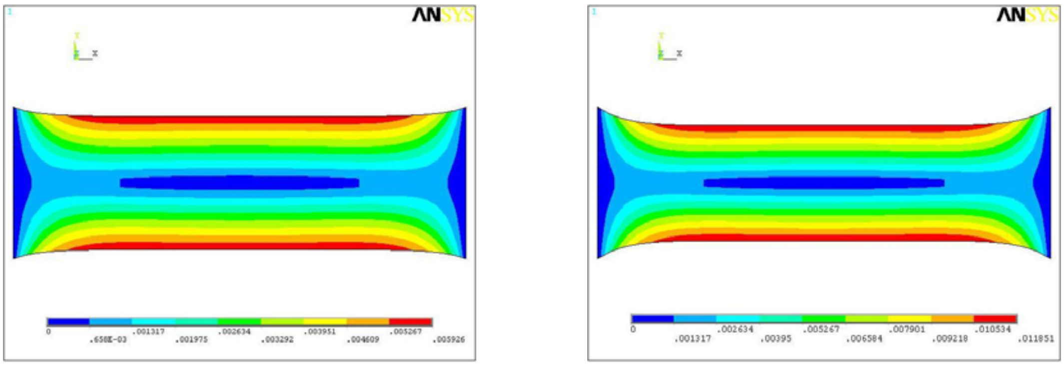

a) b)

Figure 2.15: Contour plots of the displacement vector sum for the deformed membrane with applied biaxial tensile stress: (a) 20 MPa and (b) 40 MPa.

Values of 20 MPa and 40 MPa biaxial tensile stress have been applied to the rectangular thin metal plate (movable electrode) to investigate its effect on the pull-down voltage. Figure 2.15

shows the contour plots of the displacement vector sum for the deformed metal membrane in its initial position (0 V bias voltage) with values of 20 MPa and 40 MPa biaxial tensile stress applied to the membrane. The displacement has been magnified by a factor of 1000 to improve visibility. It can be seen that the displacement is proportional to the applied stress value in this stress range and the metal membrane exhibits a linear behaviour. It is obvious, that the displacement is maximum in *y*-direction, and no displacement is observed at the fixed edges.

Figure 2.16 shows the contour plots of the stress intensity at the top surface of the metal membrane in its initial position (0 V bias voltage) with a biaxial tensile stress of 20 MPa and of 40 MPa. Due to the structure symmetry only one half of the membrane is shown. The maximum stress is observed near the sharp corners of the membrane, and is 24.4 MPa and 48.8 MPa for 20 MPa and 40 MPa biaxial tensile stress, respectively. There are critical points on the suspended metal plates. This stress concentration could spread tiny cracks produced during fabrication. The stress in the middle part of the membrane is constant and quite small, 4.2 MPa and 8.4 MPa for the plate with 20 MPa and 40 MPa, respectively.

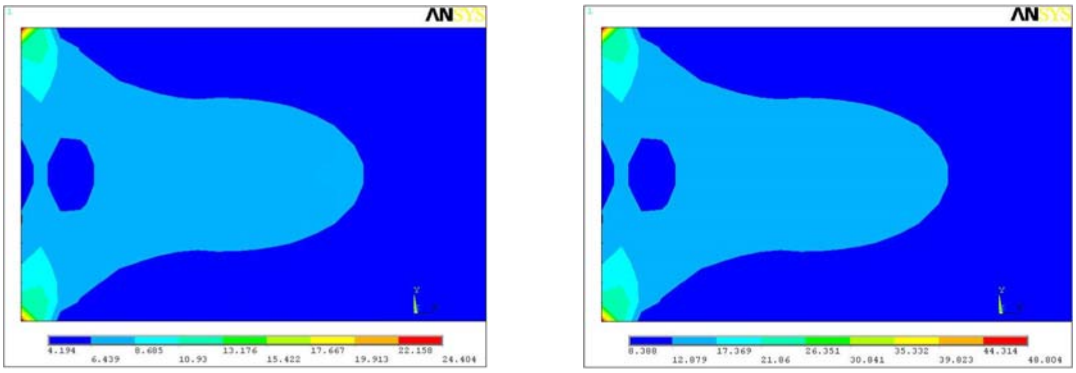

a) b)

Figure 2.16: Contour plots of the stress intensity for the membrane in its initial position with applied biaxial tensile stress: (a) 20 MPa and (b) 40 MPa.

Figure 2.17 shows the contour plots of the stress distribution at the top surface in the *x*-, *y*-, and *z*-directions and stress intensity for the membrane with 0.7 µm center deflection and applied biaxial tensile stress of 20 MPa. As in the case of no actuated structure with applied biaxial tensile stress the critical points are near the sharp corners at the fixed edges. It is obvious that the maximum stress is in the *x*-direction where the membrane has a limited degree of freedom due to the fixed opposite edges. The main stress concentration is located at the fixed edges while the middle part of the membrane is almost unstressed.

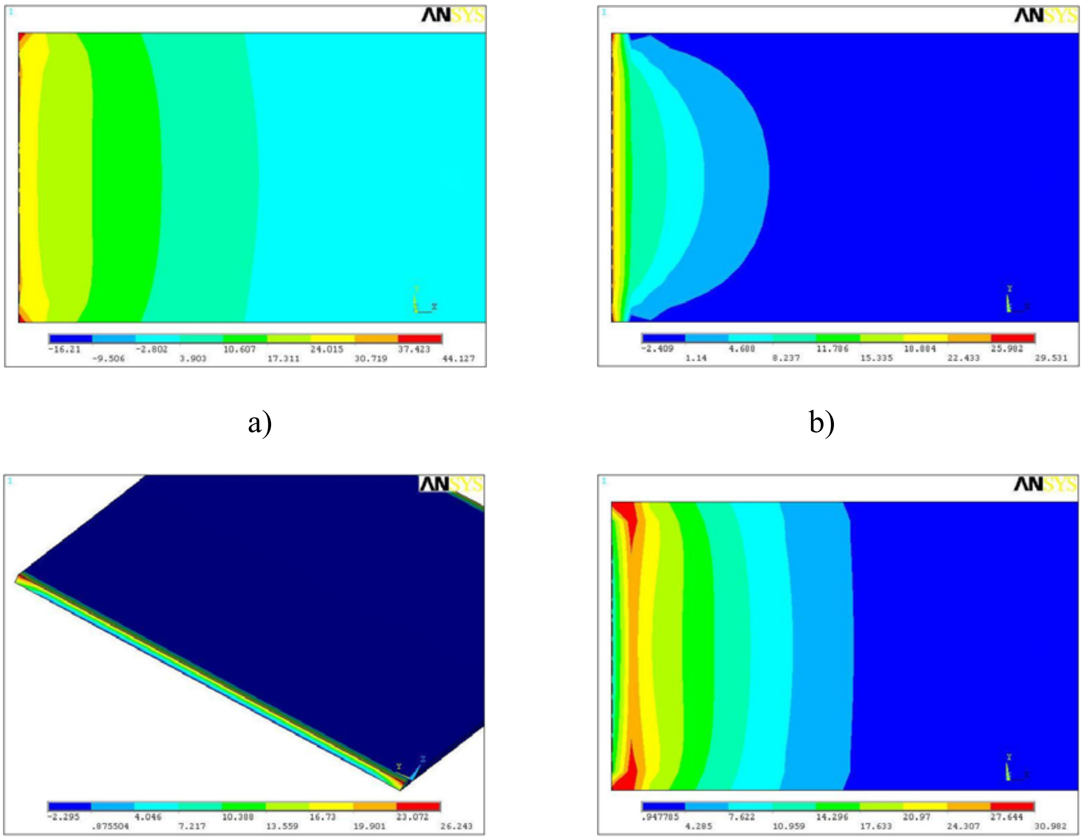

a) b)

c) d)

Figure 2.17: Contour plots of the stress for the membrane with 0.7 µm center deflection and an applied biaxial tensile stress of 20 MPa: (a) S_x component, (b) S_y component, (c) S_z component and (d) stress intensity.

The value of the compressive stress in the bottom surface of the membrane (not shown in the figure) is not comparable to the value of the tensile stress in the top surface, as in the case of the unstressed membrane (Figure 2.14) because the compressive stress is reduced by the applied biaxial residual stress. The maximum stress intensity is 31 MPa, as shown in Figure 2.17 (d), and does not exceed the allowable value for aluminum of 55-310 MPa.

The same tendency has been observed for the fixed-fixed beam with 0.7 µm center deflection and an applied biaxial tensile stress of 40 MPa, as shown in Figure 2.18. There only the contour plots of the *x*-component of stress at the top surface are shown, where the stress is largest. It can be seen that the maximum value of the compressive stress in *x*-direction is less than in the membrane with 20 MPa tensile stress. The maximum stress intensity is 57.1 MPa that is close to the lower limit of the allowable stress range for the aluminum. Typical average tensile stress in thin aluminum membranes, which is usually used for fixed-fixed beam simulation, amounts close to about 20 MPa.

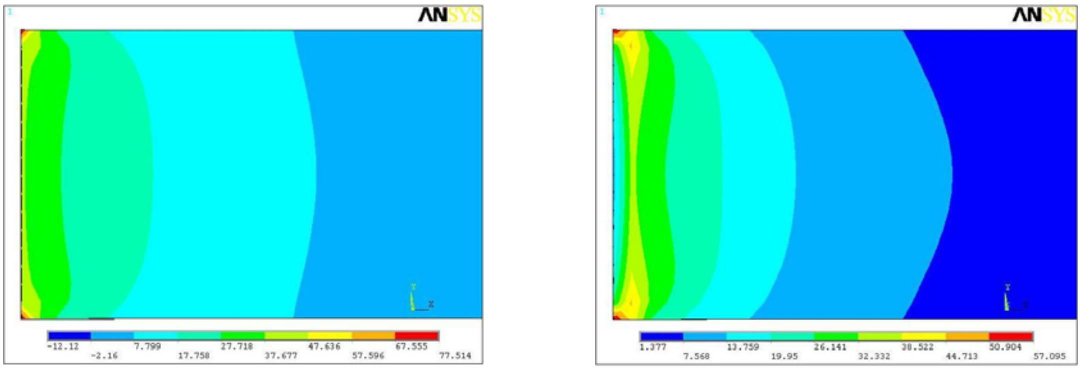

a) b)

Figure 2.18: Contour plots of the stress for the membrane with 0.7 µm center deflection and applied biaxial tensile stress of 40 MPa: (a) S_x component and (d) stress intensity.

The curves of the center deflection of the stressed membrane versus the applied voltage predicted by the analyses are shown in Figure 2.19. It can be seen that the pull-down voltage is increased up to 55 V for the membrane with a biaxial tensile stress of 40 MPa. It is well known that the high actuation-voltages can result in a stiction after a limited number of actuation cycles due to charge accumulation in the dielectric layer [57-60]. Therefore, designing of reliable MEMS switches requires lower actuation-voltages.

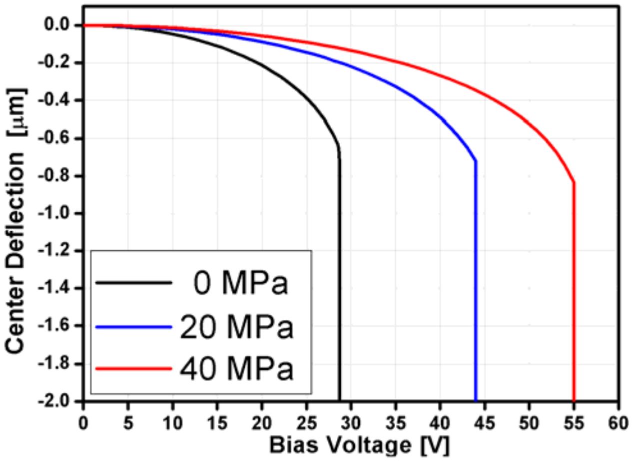

Figure 2.19: Membrane center deflection for the 3-D model with different values of the biaxial tensile stress versus applied voltage.

2.5 Summary

In this chapter, two- and three-dimensional coupled electrostatic-mechanical models for fixed-fixed beam parallel plate structures have been presented. The simulations have been performed using the finite element method (FEM) in ANSYS environment in order to determine the deformation of the membrane as a function of the applied voltage. The influence of the residual biaxial tensile stress on the structure behaviour has also been investigated.

Two methods for the modeling of the electrostatic environment have been presented. One is the sequential coupling algorithm which allows the combination of the strength of single field simulators. The electrostatic problem is based on the solution of the Laplace’s equation in the different homogenous regions. The second method to solve the electrostatic problem in ANSYS environment is the lumped or reduced order model. This method is implemented by using lumped transducer elements which convert the stored electrostatic energy into mechanical energy and vice versa. The mechanical model to determine the deformation of the membrane under acting of the electrostatic force is obtained following the plate/shell theory.

The predictions by the simulation are very close to the theoretical calculations described in chapter 1. The sequential coupling algorithm leads to results of high accuracy as the fringing field effect is taken into account. But this algorithm requires much more CPU time compared to a lumped or reduced order model.

The simulated stress level in a deformed 1.0 µm thick *Al* metal membrane with an applied biaxial tensile stress of 40 MPa does not exceed the critical value of aluminum. It has been shown, however, that the initial biaxial tensile stress can increase the pull-down voltage significantly.

Chapter 3

Design, Modeling and Optimization of Low Actuation-Voltage RF MEMS Switches

This chapter is treating design and optimization of low actuation-voltage, high RF performance MEMS switches. Several different approaches to enlarge the isolation of the RF MEMS switches will be investigated using a numerical design technique based on 3-D full-wave electromagnetic and circuit simulations using the commercial EM MoM simulators Sonnet [159] and Microwave Office [160]. The first method is realized by adding a thin metal layer on the bottom surface of the dielectric deposited on the center conductor. And the second one is based on the realization of capacitive structures on the ground plane. In this study all RF MEMS switches are designed on a 735 µm thick high-resistivity (> 5 kΩ·cm) silicon substrate (ε_r=11.9) covered by a 1.0 µm silicon dioxide (ε_r=3.9) buffer layer in order to decrease the dielectric loss in substrate. The structures are modeled on 50-Ω CPW lines with a center conductor width of W = 120 µm and a slot width of G = 80 µm. Aluminum is used as a metallization material. FEM simulations are performed for the electromechanical modeling using the ANSYS platform. The chapter starts with the description of the conventional RF MEMS shunt-capacitive and shunt-resistive switches operation. In the next sections the designs of the low-actuation voltage RF MEMS switches based on a H-shaped membrane will be introduced and investigated. For all switches, the lumped-element equivalent circuit model will be studied for a better understanding and for optimization purposes.

3.1 Conventional RF MEMS Switches Operation

A conventional RF MEMS shunt-capacitive switch in a fixed-fixed beam configuration consists of a thin metal membrane suspended over a lower electrode (CPW signal line) which is covered by a dielectric layer, as shown in Figure 3.1 (a). In the case of a RF MEMS shunt-resistive switch the actuation electrodes are placed on the sides of a center conductor and a metal dimple is added between a movable membrane and a signal line as shown in Figure 3.1 (b). For the shunt-capacitive switch the dielectric film, which covers the bottom electrode, prevents the electric short between the moveable membrane and the bottom electrode and realises a low impedance path for the RF signal when the switch is actuated. In the ON-state the membrane is in the up-position and the fixed-fixed beam provides a high impedance path for the RF signal due to a low capacitance between the membrane and the CPW signal line. Figure 3.2 (a) shows simulated EM frequency responses of the conventional RF MEMS shunt-capacitive and shunt-resistive switches in the ON-state with a bridge size of $300\times100\ \mu m^2$ and a center conductor width of 100 μm. After applying a dc voltage between the moveable membrane and the fixed lower electrode the bridge is pulled down onto a dielectric surface; the switch starts in the OFF-state. When the membrane is in direct contact with the dielectric layer in the case of a shunt-capacitive switch or with the ohmic contact in the case of a shunt-resistive switch the bridge provides a low impedance path for the RF signal due to a high capacitance (shunt-capacitive switch) or low resistance (shunt-resistive switch). The simulated EM frequency responses of the conventional shunt-capacitive and shunt-resistive switches in the OFF-state are depicted in Figure 3.2 (b).

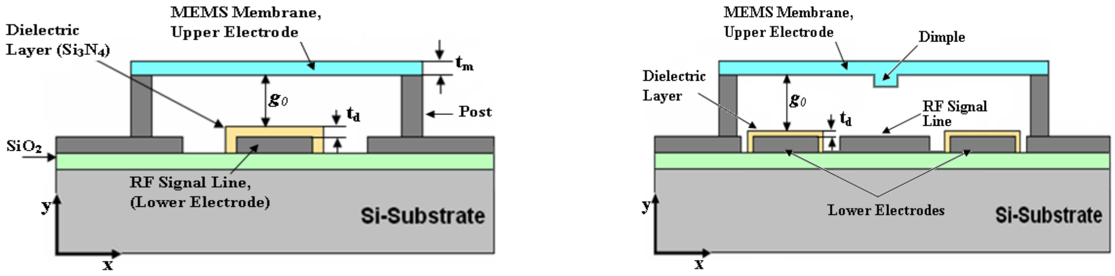

a) b)

Figure 3.1: Fixed-fixed beam FR MEMS switches: (a) shunt-capacitive switch and (b) shun-resistive switch.

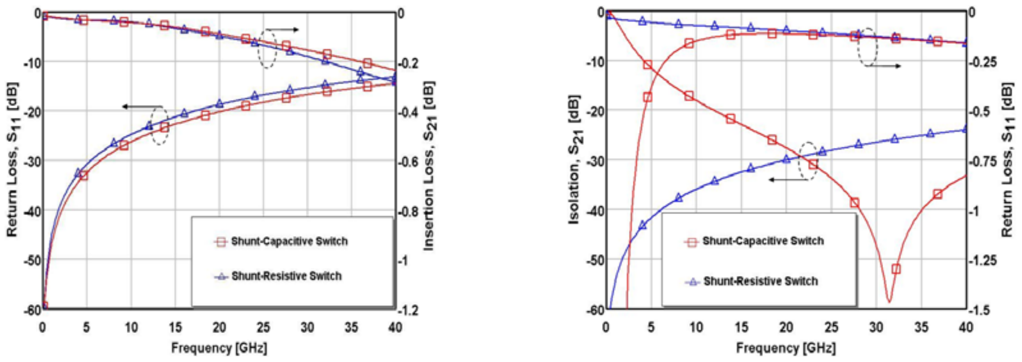

a) b)

Figure 3.2: EM simulations for the conventional RF MEMS shunt-capacitive and shunt-resistive switches: (a) up-state and (b) down-state.

3.2 Design of H-Shaped Low Actuation-Voltage RF MEMS Switches

In this section, new designs for RF MEMS shunt-capacitive and shunt-resistive switches are investigated to meet the requirements of a low actuation-voltage and a high reliability for many RF and microwave applications.

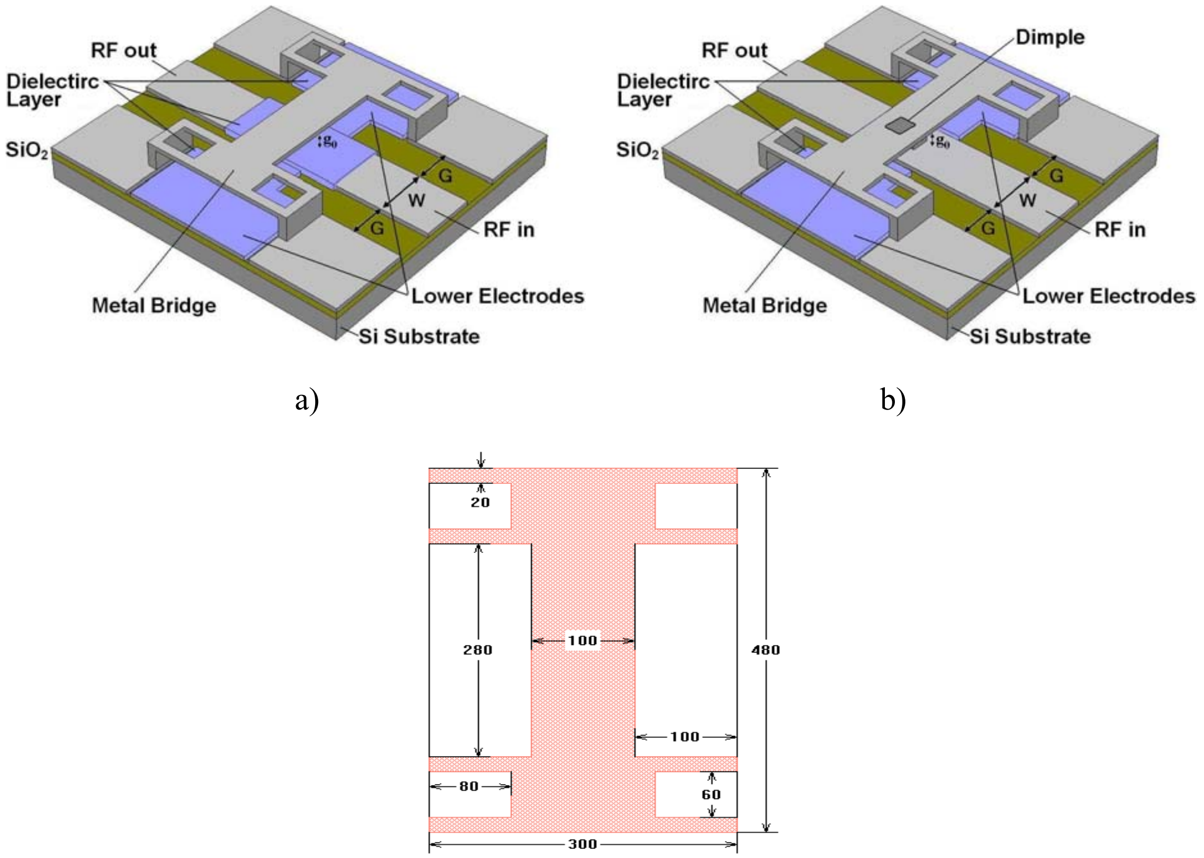

a)

b)

c)

Figure 3.3: Schematic diagram of the designed RF MEMS switches: (a) shunt-capacitive switch, (b) shunt-resistive switch and (c) H-shaped membrane (b). All dimensions in microns.

3.2.1 H-Shaped MEMS Switch Design

Figure 3.3 (a) and (b) show schematic diagrams of the designed RF MEMS shunt-capacitive and shunt-resistive switches. They consist of the so-called H-shaped membrane suspended above a coplanar waveguide line. Figure 3.3 (c) shows the moveable electrode which consists of two bridges with fixed-fixed flexure suspensions, which are connected to each other by the contact area. The membrane with a thickness of 0.8 μm is suspended above the lower electrode with an initial gap height $g_0 = 3.0$ μm. The lower electrodes are made of a higher resistivity metal (*NiCr*) with a sheet resistance of 1400 Ω/square. A silicon nitride layer of 0.1 μm thickness and a relative permittivity of 7.6 covers the lower electrodes to avoid the direct electrical contact between the metal electrodes. For a capacitive switch, this dielectric layer is larger and covers the signal line underneath the membrane to achieve a high coupling capacitance in the OFF-state. In the case of the shunt-resistive switch(see Figure 3.3 (b)), a 50×60 μm rectangular dimple with height of 0.15 μm is added to the lower surface of the membrane above the RF signal line in order to achieve a good metal-to-metal contact in the OFF-state.

3.2.2 Electromagnetic and Circuit Simulations

RF responses for the capacitively coupled and the resistive-contact switches are shown in Figure 3.4 (a) and 3.4 (b) for the ON- and OFF-states, respectively. The optimized ON-state return losses (S_{11}) are less than -18 dB and -21 dB, while the insertion losses (S_{21}) are less than 0.19 dB and 0.18 dB from dc up to 40 GHz for the resistive and the capacitive switches, respectively. The OFF-state isolation (S_{21}) for the resistive structure is higher than -25 dB from dc up to 40 GHz, while for the capacitive one it is higher than -20 dB at 7.0 GHz and higher than -30 dB from 15 GHz up to 40 GHz, see Figure 3.4 (b).

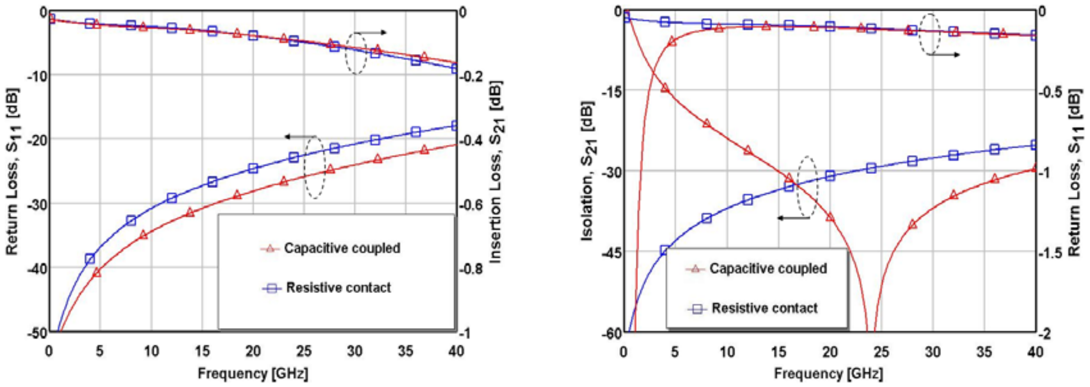

a) b)

Figure 3.4: EM simulations for the designed shunt-capacitive and shunt-resistive RF MEMS switches: (a) in the ON-state and (b) in the OFF-state.

The EM circuit simulator has been used to find out an appropriate equivalent circuit for the designed RF MEMS switches. Figure 3.5 shows the equivalent circuit model for both the types of H-shaped RF MEMS switches.

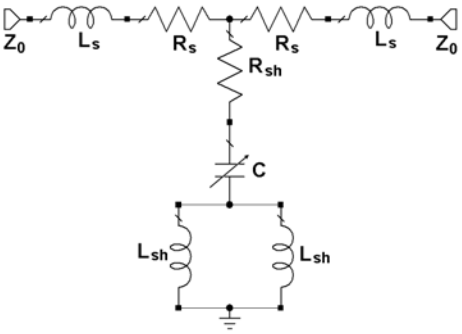

Figure 3.5: Equivalent circuit model for the designed RF MEMS switches.

The bridge structure is modeled by a lumped *RLC* branch, which represents the circuit with the changeable capacitance from the up-position to the down-position. It should be noted, that for the shunt-resistive switch in the down-position (OFF-state) the capacitance *C* must be removed from the branch because the capacitive coupling changes to ohmic. This electrical circuit model has been used to fit the S-parameters of the switches, which are obtained by using the EM simulator. The simulation results for both switches in the ON- and OFF-states are depicted in Figure 3.6 and Figure 3.7. A good matching between the circuit and the EM simulations assure that the proposed equivalent circuit model describes the H-shaped RF MEMS shunt-capacitive and shunt-resistive switches with sufficient accuracy. Table 3.1 shows the values of the lumped electrical circuit parameters extracted from circuit simulation.

Table 3.1 Extracted equivalent circuit element parameters

	Shunt-Capacitive Switch		**Shunt-Resistive Switch**	
	ON-state	OFF-state	ON-state	OFF-state
C (pF)	0.036	8.08	0.039	—
L_{sh} (pH)	12	12.5	11.7	11.8
R_{sh} (Ω)	5.0	0.011	4.2	0.0255
L_s (pH)	30	30	25.6	25.6
R_s (mΩ)	200	337	230	200

The simulated frequency responses of the designed RF MEMS switches shown in Figure 3.4 are achieved by an iterative optimization technique. Some of these results are depicted in Figure 3.8. The switches have a good isolation over a wide bandwidth. The initial gap height g_0 between the movable membrane and the RF center conductor has an influence on the insertion loss which depends on the up-state capacitance. Therefore, the capacitive coupling must be as small as possible. It can be reached by an increase of the gap height or a decrease of the overlap between bridge and signal line areas. But a large gap leads to an increase of the actuation-voltage and a decreased overlap leads to a deterioration of the OFF-state isolation.

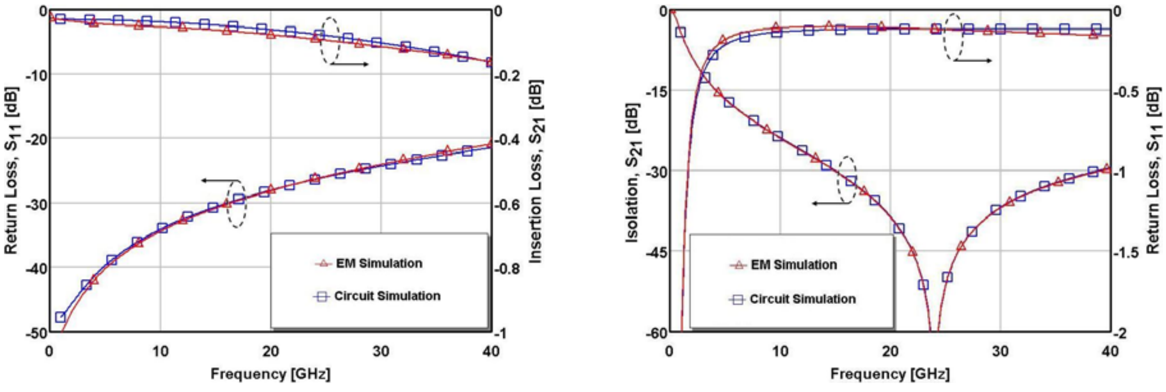

a) b)

Figure 3.6: EM and equivalent circuit model simulations for the designed shunt-capacitive RF MEMS switch: (a) in the ON-state and (b) in the OFF-state.

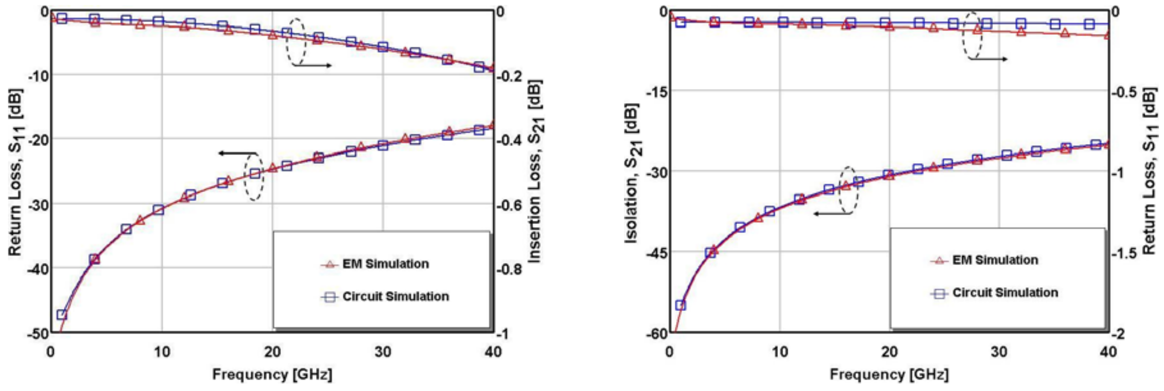

a) b)

Figure 3.7: EM and equivalent circuit model simulations for the designed shunt-resistive RF MEMS switch: (a) in the ON-state and (b) in the OFF-state.

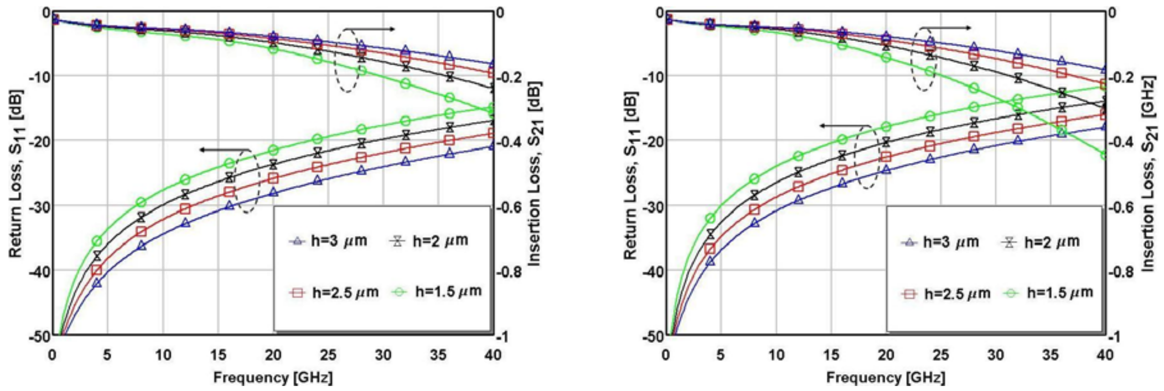

a) b)

Figure 3.8: EM simulation for the designed RF MEMS switches in the ON-state for different values of the initial gap height g_0**:** (a) shunt-capacitive switch and (b) shunt-resistive switch.

A compromise between these values has to be found. Figure 3.8 shows RF responses for the shunt-capacitive and shunt-resistive switches in the up-position for different gap heights. It can be seen in the figure that a 3 µm gap is the optimum value for the both switches to achieve a return loss less than -18 dB with an insertion loss less than 0.2 dB from dc up to 40 GHz.

3.2.3 Electromechanical Modeling

As has been mentioned in chapter 1 the formula for the pull-down voltage in terms of the switch dimensions is given by [39]:

$$V_p = \sqrt{\frac{8kg_o^3}{27A\varepsilon_o}} \tag{3.1}$$

where k is the spring constant of the membrane, g_o is the initial gap height between the membrane and the bottom electrode, A is the area of the actuation pads and ε_o is the free space permittivity. There are three approaches to reduce the pull-down voltage: 1) reducing the spring constant; 2) decreasing the gap between the membrane and the bottom electrode; and 3) increasing the effective actuation area. A small gap height can lead to an increase of the insertion losses of the switch as has been shown above. The effective area of the actuation electrodes is limited with regard to the total area of the device. Decreasing the spring-constant is the route with the highest flexibility, since the design of the springs does not have a considerable impact on size, weight, and/or RF performance of the circuit. The actuation areas of the lower electrodes have been extended toward CPW line under the membrane. The use of a low spring-constant suspension membrane supports with improvement.

The electromechanical simulations have been carried out with the FEM simulator using the reduced order method. The 1-D transducer element (*TRANS126*) has been used to directly couple the structural motion with the electrostatic fields, as shown in chapter 2. The initial residual stress has been introduced by applying a “negative” temperature to the membrane and considered with large deformation and stress stiffening effects. A zero voltage has been applied to the bottom electrodes, while the actuation voltage has been applied to the membrane.

All geometrical parameters must fulfill the fabrication requirements, which are the major considerations of the geometrical design. The proposed design is completely based on real fabrication data. 20 MPa and 40 MPa biaxial tensile stresses have been applied to the H-shaped switch to examine its effect on the pull-down voltage. Figure 3.9 (a) shows the shape of the membrane with an actuation voltage of 14 V (very close to the pull-down voltage) and no residual stress. The maximum deflection of the membrane is 1.77 μm at the center of the contact area. The maximum stress concentrates in the meander suspension near the contact area, as shown in Figure 3.9 (b), because there are maximum torsion and motion in all directions. The maximum stress of 25.5 MPa does not exceed the allowable value for aluminum of 55-310 MPa.

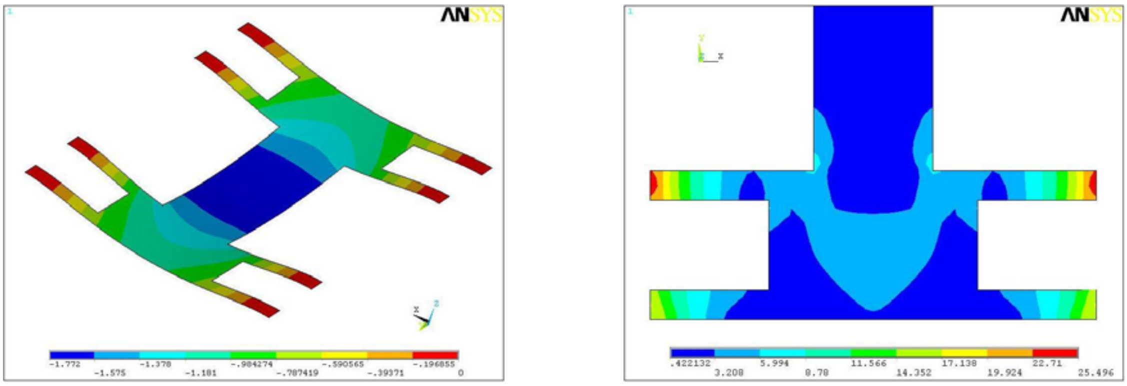

a) b)

Figure 3.9: Contour plot of the H-shaped membrane with an applied bias voltage of 14 V and no residual stress: (a) deformed shape and (b) stress strength.

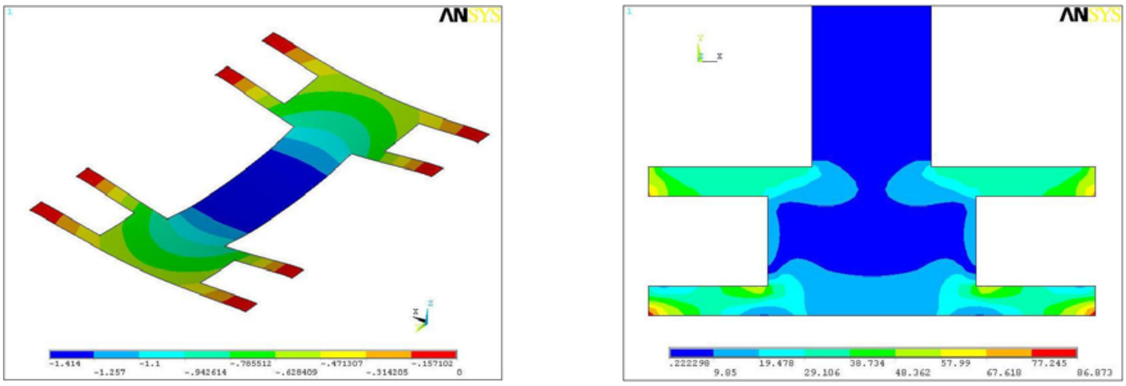

a) b)

Figure 3.10: Contour plot of the H-shaped membrane with an applied bias voltage of 32.5 V and 40 MPa biaxial tensile stress: (a) deformed shape and (b) stress strength.

Figure 3.10 shows contour plot of the deformed H-shaped membrane with an applied bias voltage of 32.5 V and a 40 MPa biaxial tensile stress (Figure 3.10 (a)) the stress strength in this membrane can be seen in Figure 3.10 (b). As in the case of a membrane with no residual stress the critical points of the H-shaped membrane are the fixed supports. The maximum value of the stress strength is 86.87 MPa, a value which exceeds the acceptable limit of aluminum of 55-310 MPa. Therefore, the fabrication conditions have to be optimised in order to obtain a membrane with low stress. The deflections of the center of the contact area versus the applied voltage are presented in Figure 3.11 for different values of biaxial tensile stress. The maximum deflection of the center of the contact area, after which the structure collapses onto the lower electrodes, decreases with an increase in the biaxial tensile stress value. This can be explained by an increased tensile strength in both directions deforming the structure before the actuation voltage is applied.

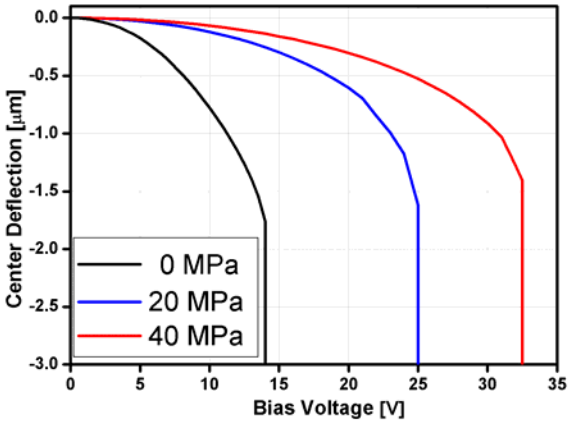

Figure 3.11: H-shaped membrane center deflection versus applied voltage for different values of the biaxial tensile stress.

3.3 Design of Low Actuation-Voltage, High Isolation S-Band MEMS Shunt-Capacitive Switches

In this section the RF MEMS shunt-capacitive switches, the concept of which has been investigated in the previous section, has been redesigned and optimized in order to obtain a high isolation at 2-4 GHz (S-band).

3.3.1 S-Band Switch Design

Figure 3.12 (a) shows the schematic diagram of the S-band MEMS shunt-capacitive switch of type1. It is based on a H-shaped membrane, investigated in the previous section, but the thickness has been increased to a 1.0 µm. The initial gap height has also been changed to 2.0 µm. The lower electrodes are made of a highly doped polysilicon with a sheet resistance of 1400 Ω/□. In this case the dielectric layer over the lower electrode can be made of silicon dioxide deposited in a high temperature low pressure chemical vapor deposition (LPCVD) process [178]. Due to LPCVD silicon oxide the reliability of a RF MEMS shunt-capacitive switch can be increased significantly. A silicon nitride layer (0.1 μm thick) covers the central RF line as a dielectric layer for capacitive coupling. The thin (50 nm) *Al* layer of 540 μm length and 130 μm width is deposited on the silicon nitride forming a large capacitance area when the switch is actuated. This metal interlayer also solves the problem related to the roughness of the dielectric layer when the switch is in the down-state. Figures 3.12 (b, c) show the top views of the investigated types of RF MEMS shunt-capacitive switches. To avoid the stiction between the membrane and the metal layer on the dielectric in the down-state the contact area should be small. Both types of MEMS switches do not require dimples at the contact areas simplifying their fabrication significantly.

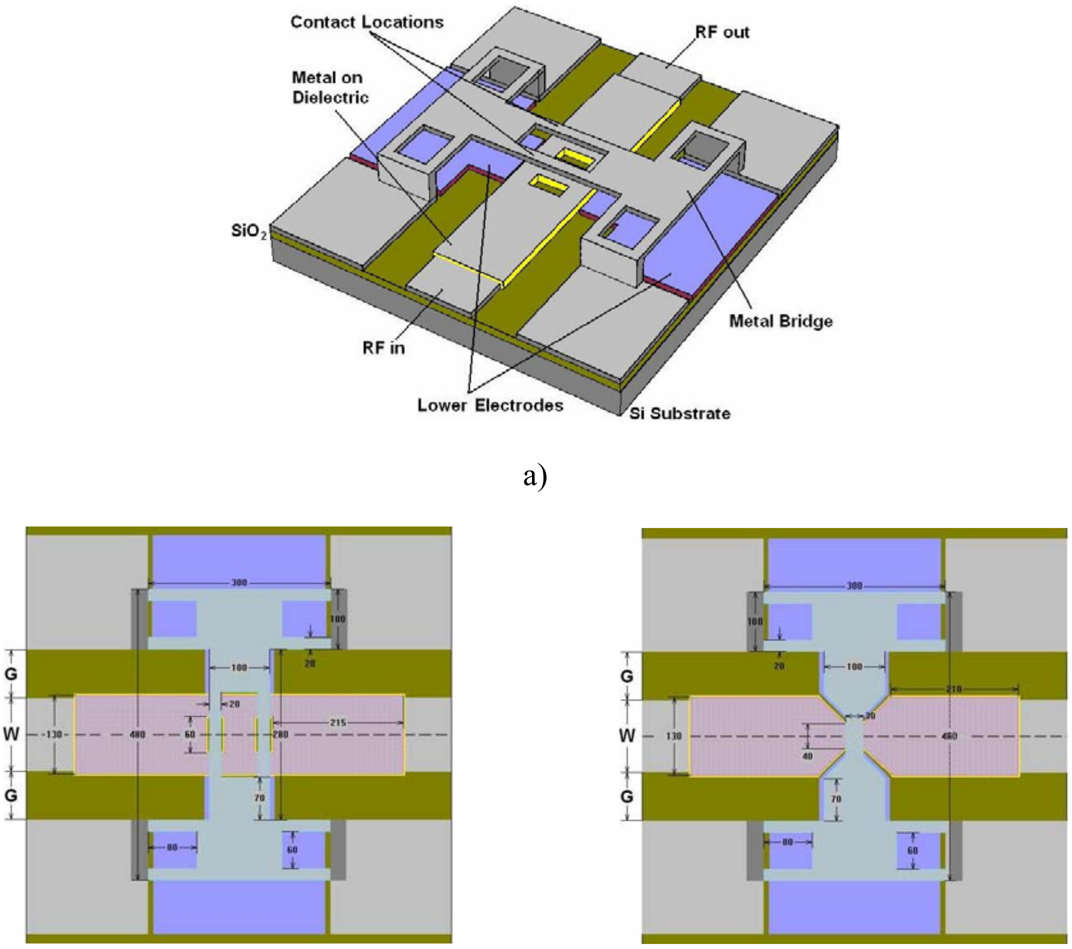

a)

b)

c)

Figure 3.12: Schematic diagrams of the designed S-band MEMS shunt-capacitive switches: (a) type 1 (3-D view), (b) type 1 (top), and (c) type 2 (top). All dimensions in microns.

3.3.2 Electromagnetic and Circuit Simulations

The designed RF MEMS shunt-capacitive switches are modeled by two short sections of the transmission lines with a characteristic impedance $Z_0 = 50\Omega$. The equivalent circuit of the designed RF MEMS shunt-capacitive switches is shown in Figure 3.13. The base-model used for the calculation of the capacitance between the RF signal line and the bridge is the parallel-plate capacitance model [39]:

$$C_{up} = \frac{\varepsilon_0 A}{g_0 + t_d / \varepsilon_r} + C_f \tag{3.2}$$

$$C_d = \frac{\varepsilon_0 \varepsilon_r A}{t_d} \tag{3.3}$$

where C_{up} and C_d are the designed up-state and the down-state capacitance, respectively. C_f is the fringing field capacitance; t_d is the thickness of the dielectric layer; g_0 is the gap between RF signal line and the bridge; ε_0 is the free space permittivity; ε_r is the relative permittivity of the dielectric layer and A is the total area of the capacitive structure. In the down-state the total capacitive area is the area of the thin metal layer deposited on the dielectric above the CPW signal line and is 59.2×10^3 µm^2 and 57.15×10^3 µm^2 corresponding to the down-state capacitances of 39.8 pF and 38.5 pF for the switches of type 1 and type 2, respectively. The total up-state capacitance area is the area below the bridge at the contact location and is 2×10^3 µm^2 and 0.9×10^3 µm^2 for the RF MEMS switches of type 1 and type 2, respectively. Thus the up-state capacitances, excluding the fringing capacitance, which usually ranges from 0.2 to 1.0 of a parallel-plate capacitance and depends on the bridge dimension and the initial gap height, are 8.80 fF for the switch of type 1 and 3.96 fF for the switch of type 2. Consequently, the designed MEMS switches have a down-state/up-state capacitance ratio higher than 3.8×10^3.

The equivalent resistance R_{sh} represents the sum of the resistances of the metal bridge R_b and the electrical pass R_{ep} between the membrane and the metal interlayer at the contact location. In the up-state the bridge inductance and the bridge resistance can be neglected because the switch impedance is predominantly determined by the small up-state capacitance.

The down-state resonant frequency of the switch response ω_0 is given by:

$$\omega_0 = \frac{1}{\sqrt{L_{sh} C}} \tag{3.4}$$

where C is the down-state capacitance which has to be relatively high to reach an acceptable isolation at lower frequencies.

The horizontal branch of the equivalent circuit in Figure 3.13 describes the CPW transmission line. As will be shown below, each type of the designed switches has different lumped-element parameters due to the shape of their CPW lines.

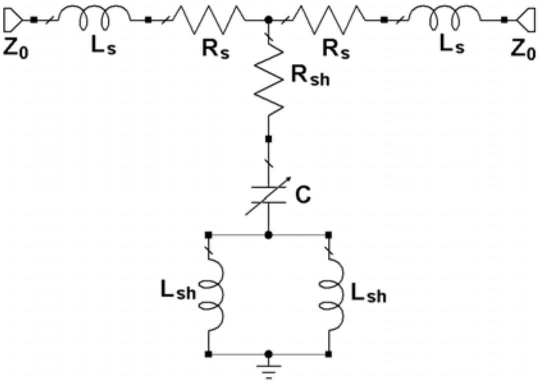

Figure 3.13: Equivalent circuit model for the designed S-band RF MEMS switches.

Figure 3.14 shows the simulated RF responses for the designed RF MEMS shunt-capacitive switches of type 1 and type 2 in the up-state and the down-state. The ON-state return loss (S_{11}) is less than -20 dB and -30 dB, while the insertion loss (S_{21}) is less than 0.32 and 0.28 dB from dc up to 35 GHz for the switches of type 1 and type 2, respectively. The OFF-state isolation (S_{21}) for both types of the designed shunt-capacitive switches is higher than -20 dB from 1.5 GHz up to 35 GHz. However, the isolation of the switch of type 1 is higher than -30 dB from 4.5 GHz up to 28 GHz with a maximum stop-band rejection of 56 dB at the resonance frequency of 11.6 GHz. The switch of type 2 provides an OFF-state isolation higher than -30 dB only from 4.2 GHz up to 20 GHz with a maximum stop-band rejection of 42 dB at the resonance frequency of 9.6 GHz.

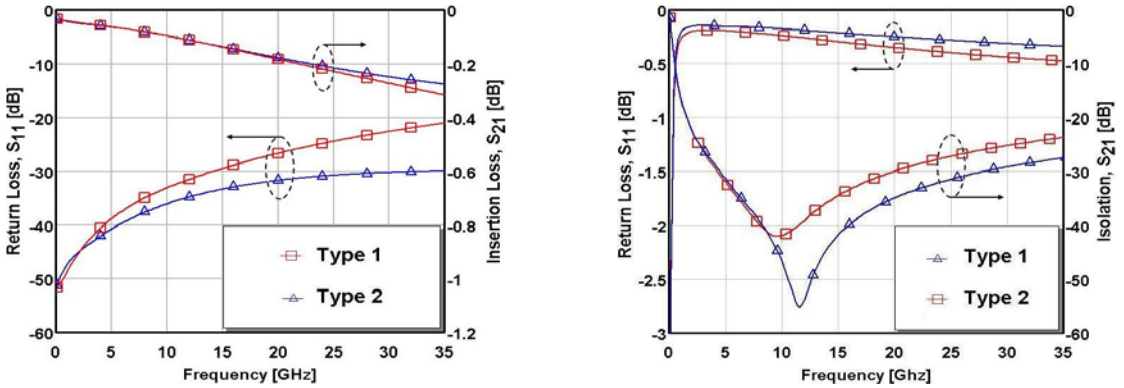

a) b)

Figure 3.14: EM simulations for the designed S-band MEMS shunt-capacitive switches: (a) in the ON-state and (b) in the OFF-state.

Figure 3.15 shows the ON- and OFF-state frequency responses obtained using EM and equivalent circuit simulations. A good agreement between both simulations has been reached.

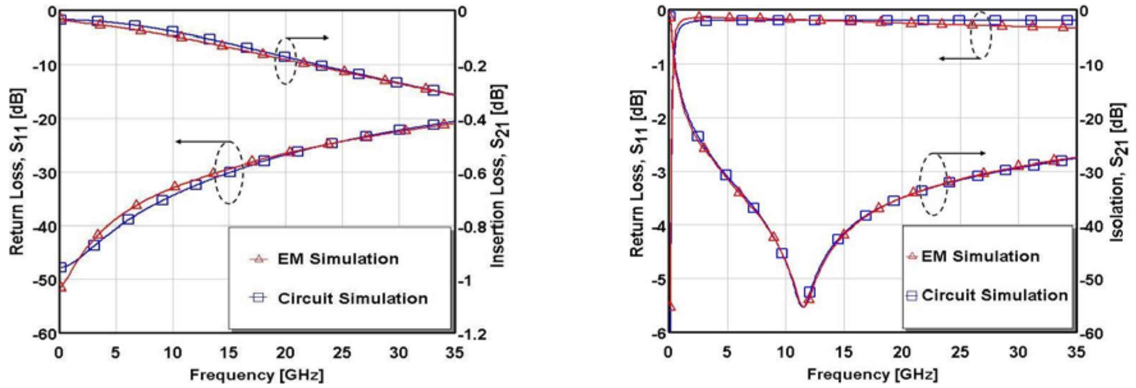

a) b)

Figure 3.15: EM and equivalent circuit simulations for the designed S-band MEMS shunt-capacitive switch of type 1: (a) in the ON-state and (b) in the OFF-state.

Table 3.2 summaries the lumped-element parameters extracted from the EM simulations. It can be seen that the designed switches have different element values due to the different shapes of the bridges and the CPW center conductors at the contact locations.

Table 3.2 Extracted equivalent circuit parameters for S-band MEMS switches

		Type 1	**Type 2**
C_{up}	(fF)	14.4	11.4
C_d	(pF)	39.2	38
L_{sh}	(pH)	10	14.4
R_{sh} *"ON"*	(Ω)	500	560
R_{sh} *"OFF"*	(mΩ)	44	200
L_s	(pH)	2.2	28.2
R_s	(mΩ)	250	250

The simulation shows that the rectangular holes on the transmission line of the switch of type 1 increase the series inductive loading L_s significantly. The theoretically calculated up-state capacitance, excluding the fringing capacitances C_f, and the EM simulated capacitance are 8.80 fF and 14.4 fF for the switch of type 1 and 3.96 fF and 11.4 fF for the switch of type 2. It can be seen that the simulated up-state capacitance is 1.7 times higher than the parallel-plate capacitance of the switch of type 1 and 3 times higher for the switch of type 2. This may be is due to the fringing field capacitance existing at the bridge edges close to the CPW signal lines. The CPW slot of the switch of type 2 is increased by the decrease of the signal line width; therefore, the inductances L_{sh} and L_s of the switch of type 2 are higher than for the switch of type 1.

The isolation of both types of RF MEMS shunt-capacitive switches at low frequency (0.8-2 GHz) can be increased by increasing the length of the thin *Al* layer on the dielectric layer. Unfortunately, the size of the switches will also be increased. Figure 3.16 shows the simulated OFF-state RF responses of the MEMS shunt-capacitive switches of type 1 and type 2 and of the same switches with an interlayer length increased to 1000 μm (high capacitance (HC) switches). It can be seen that the HC switches have an isolation of -20 dB at 0.8 GHz that makes them useful for mobile systems such as cell phones, etc.

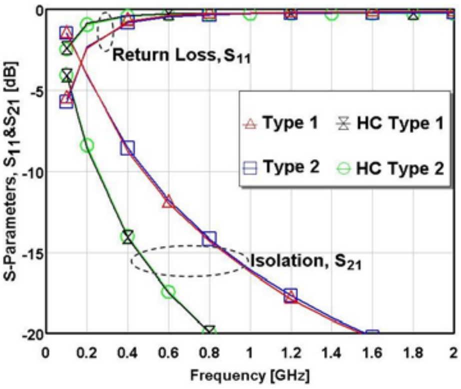

Figure 3.16: EM simulations for the designed MEMS switches in the OFF-state.

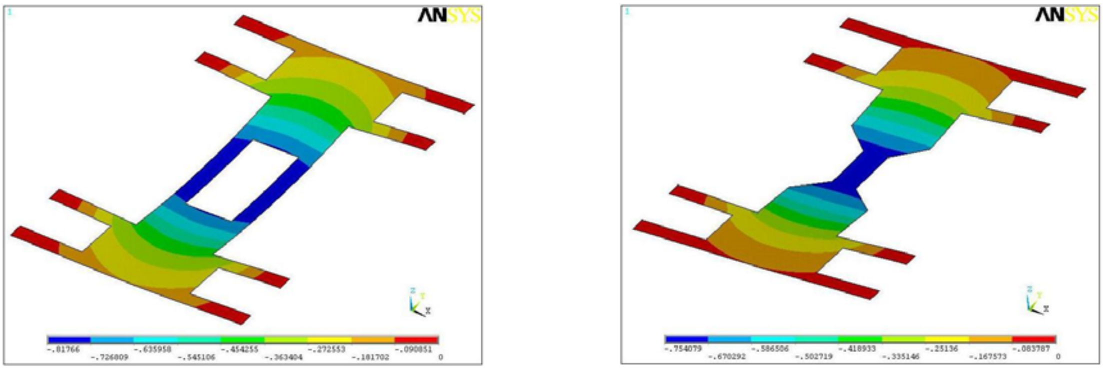

a) b)

Figure 3.17: Contour plot of the deformed membranes with biaxial tensile stress of 20 MPa: (a) switch of type 1 at 11.5 V and (b) switch of type 2 at 9.0 V.

3.3.3 Electromechanical Modeling

The electromechanical modeling for the designed S-band MEMS shunt-capacitive switches has been carried out with the FEM simulator using the sequentially coupled method. Figure 3.17 shows the contour plots of the deformed membranes with a biaxial tensile stress of 20 MPa with actuation-voltages of 12 V and 9 V (very close to the pull-down voltage) for the switches of type 1 and type 2, respectively. It can be observed that the maximum deflection is at the contact location for both switches.

The contour plots of the stress intensity are depicted in Figure 3.18 (a, b). The maximum stress concentration has been observed at the sharp corners of the fixed meander suspensions, while the contact areas are almost unstressed. The maximum stress strength for both switches is less than 39 MPa and does not exceed the allowable value of aluminum.

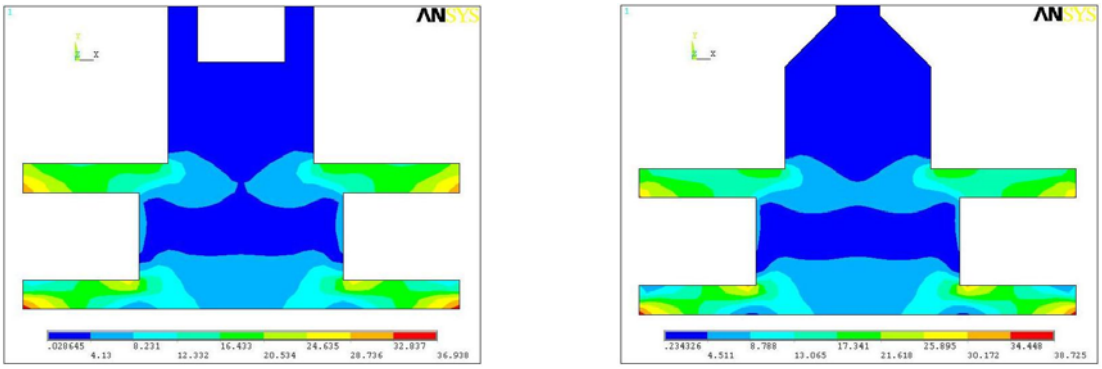

a) b)

Figure 3.18: Contour plot of the stress strength in the deformed membranes with biaxial tensile stress of 20 MPa: (a) switch of type 1 at 11.5 V and (b) switch of type 2 at 9.0 V.

Figure 3.19 shows the deflection of the center of the contact areas in dependence on the applied voltage for both types of the designed RF MEMS switches for different values of the biaxial tensile stress. It can be seen that the biaxial tensile residual stress increases the pull-down voltage but the voltage value dose not exceed 15 V even for a tensile stress of 40 MPa.

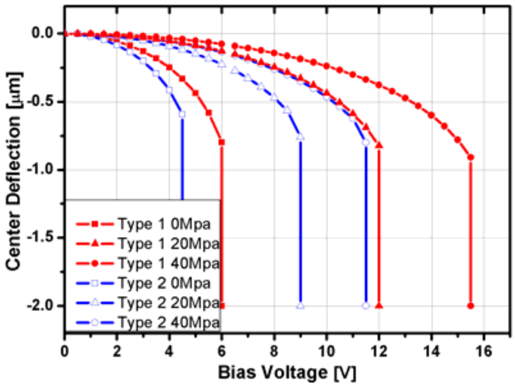

Figure 3.19: The membrane center deflection versus applied voltage for different values of the biaxial tensile stress.

The proposed design of MEMS shunt-capacitive switches is completely based on real fabrication facilities and requires five lithographic masks.

3.4 Design of Low Actuation-Voltage High Isolation L-Band MEMS DC-Contact Shunt-Capacitive Switches

In this section the design of a dc-contact shunt-capacitive L-band MEMS switch based on the geometry concept investigated in previous sections will be presented. The dielectric on ground (DOG) structure has been used to increase the capacitive coupling and, thus, to improve the switch isolation at low frequencies. A new approach to solve the stiction problem and to achieve the out-of-plane profile membrane is proposed.

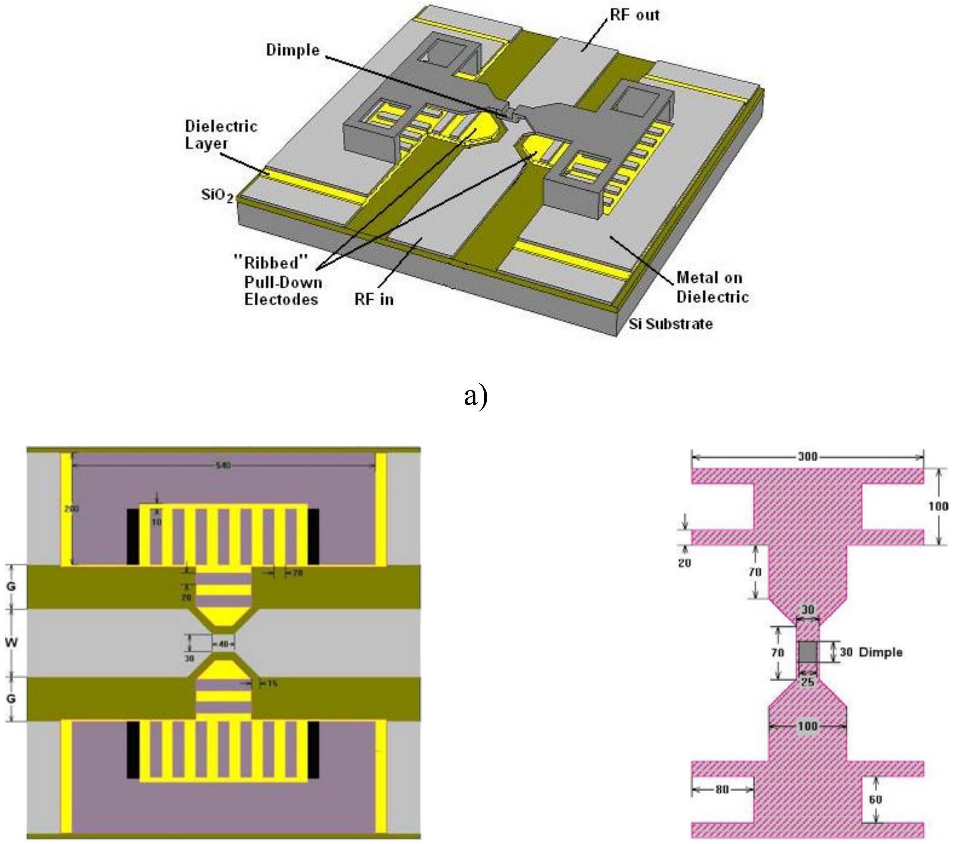

a)

b)

c)

Figure 3.20: Schematic diagram of the designed L-band MEMS dc-contact shunt-capacitive switch: (a) 3-D view, (b) top view and (c) moveable membrane. All dimensions in microns.

3.4.1 L-Band Switch Design and Description

Figure 3.20 shows the schematic diagram of the designed L-band RF MEMS dc-contact shunt-capacitive switch. It consists of the H-shaped membrane suspended above a coplanar waveguide line with an initial gap height of 2 μm described above. The moveable membrane with a thickness of 1.0 μm is depicted in Figure 3.20 (c). A 25×30 μm^2 rectangular dimple with a height of 0.6 μm is additionally located at the center of the contact area. This dimple forms an electrical contact with the center conductor when the switch is actuated. A silicon nitride layer with a thickness of 0.1 μm covers the ground planes as a dielectric layer for capacitive coupling. A 0.5 μm thick aluminum layer deposited on the dielectric layer represents the upper electrode of the resulting MIM structure. This metallization also forms the “ribs” on the lower actuation electrodes as shown in Figure 3.20 (b). Figure 3.21 (a, b) shows a schematic diagram of the predicted out-off-plane profile of the membrane after fabrication. The wave-shaped membrane and the ribbed pull-down electrodes decrease the contact area between the metal bridge and the lower electrodes reducing the risk of stiction. Moreover, the out-off-plane membrane decreases the influence of the residual stress. The driving voltage is applied between the ground planes of the CPW line and the upper metal films deposited on the dielectric layer.

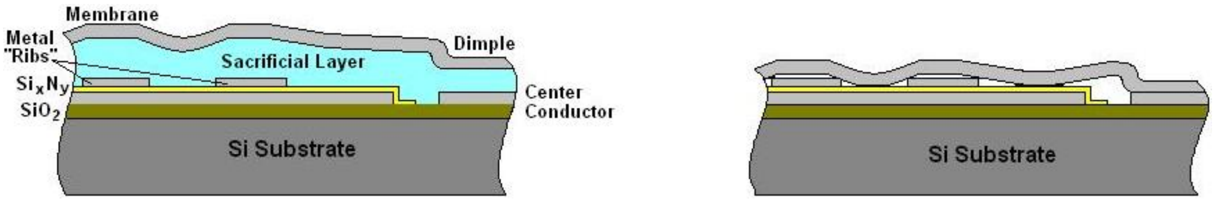

a) b)

Figure 3.21: Schematic diagram of the predicted shape of the membranes at the contact location: (a) on the sacrificial layer and (b) after fabrication when the switch is actuated.

3.4.2 Electromagnetic and Circuit Simulations

Figure 3.22 shows the equivalent circuit model of the designed L-band MEMS dc-contact shunt-capacitive switch. The up-state capacitance is mainly determined by the area of the metal bridge over the center conductor. For this reason and to decrease the up-state insertion loss the width of the bridge over the signal line and the RF central line at the contact location have been decreased, as shown in Figure 3.20. In the down-state the capacitance of the switch is determined by the MIM capacitors at the posts of the metal bridge while the capacitance C_{up} has to be removed from the lumped-element circuit model. In order to provide a low contact resistance between the bridge and the signal line a dimple has been formed at the contact location. A high contact resistance leads to an increase in the radiation loss and, thus, to a reduction of the stop-band rejection.

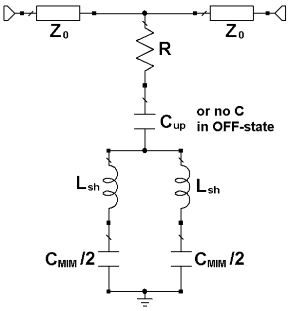

Figure 3.22: Equivalent circuit model for the designed L-band RF MEMS switch.

Figure 3.23 shows the simulated frequency response of the designed RF MEMS dc-contact shunt-capacitive switch using EM and equivalent circuit simulators. The ON-state return loss (S_{11}) is less than -40 dB while the insertion loss (S_{21}) is less than 0.8 dB from dc up to 40 GHz. The OFF-state isolation (S_{21}) of the designed switch is higher than -25 dB at 0.8 GHz and close to -20 dB at 40 GHz.

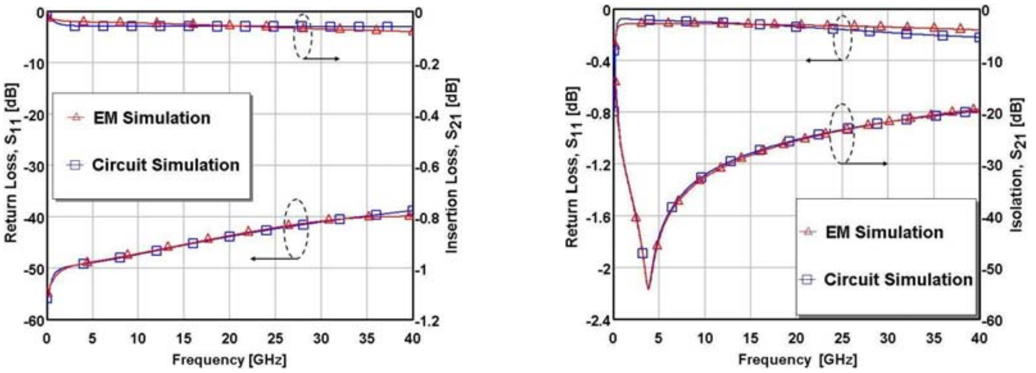

a) b)

Figure 3.23: EM and equivalent circuit simulations for the designed L-band MEMS dc-contact shunt-capacitive switch: (a) in the ON-state and (b) in the OFF-state.

Table 3.3 RF characteristics and extracted *RLC* values

	ON-state	OFF-state
• Return loss (dB)		
0.8 GHz	52	0.08
3.8 GHz	49	0.09
40 GHz	40	0.22
• Isolation (dB)		
0.8 GHz	0.03	26
3.8 GHz	0.04	54
40 GHz	0.08	19
Capacitance C_{up} (fF)	2.4	–
Capacitance C_{MIM} (pF)	150	150
Inductance *Lsh* (pH)	23.1	23.1
Resistance R (Ω)	1200	0.5

Table 3.3 summarises the lumped-element parameters extracted from the circuit simulation and the RF characteristics of the switch. The down-state capacitance determined by the MIM structure is 150 pF. According to Eqn. 3.4 the resonance frequency is shifted to lower frequencies and occurs at a 3.8 GHz. The inductance L_{sh} is relatively high as in this case the piece of the bridge located above the CPW slot is enlarged.

3.4.3 Electromechanical Modeling

The electromechanical modeling has been performed using FEM sequentially coupled analysis. Figure 3.24 (a) shows the contour plots of the deformed membrane with an applied voltage of 9.0 V (very close to the pull-down voltage) and with a biaxial tensile stress of 20 MPa. It can be seen that the required maximum deflection is at the contact location. The contour plot of the stress strength is depicted in Figure 3.24 (b). As in the previous cases the maximum stress concentrates in the meander suspensions at the fixed edges and is less than 39 MPa. The area between the fixed-fixed flexure suspensions is almost unstressed excluding the contact location where the metal walls in *z*-direction form the dimple. The vertical metal walls of the dimple introduce a stress gradient in the contact location from 4.2 MPa to 8.63 MPa. This value is several times less than the allowable value of aluminum.

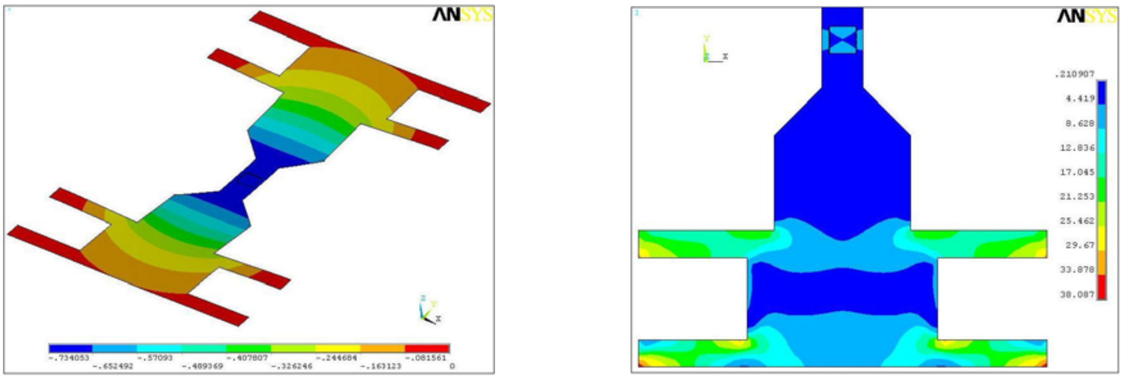

a) b)

Figure 3.24: Contour plot of the membrane with an applied bias voltage of 9 V and biaxial tensile stress: deformed shape (a), and stress strength (b).

Figure 3.25 shows the deflection of the center of the dimple versus the applied bias voltage for different values of biaxial tensile stress. It can be seen that even for a 40 MPa biaxial tensile stress the pull-down voltage does not exceed 12 V.

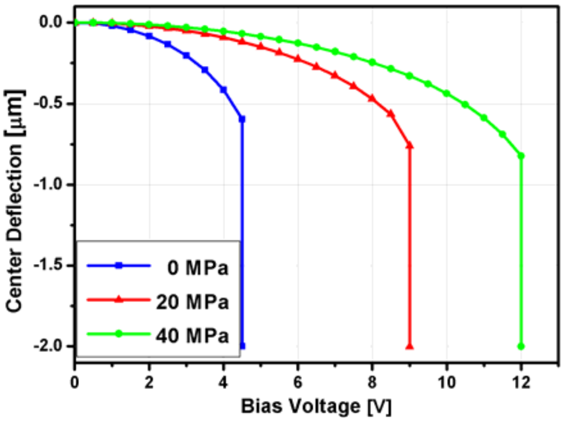

Figure 3.25: The displacement of the center of the dimple versus the applied voltage for different values of biaxial tensile stress.

3.5 Summary

The concept of low actuation-voltage, high isolation RF MEMS switches has been introduced and investigated in this chapter. The switches are based on the designed H-shape membrane with a low spring constant fixed-fixed flexure suspension. Shunt-capacitive and shunt-resistive modifications have been modeled and optimized using EM MoM and FEM simulation platforms. The simulated base-model of the H-shape RF MEMS switch is useful for X-band applications and provides an ON-state insertion loss less than 0.2 dB together with a return loss of more than -18 dB. The simulated OFF-state isolation is higher than -20 dB from 7.0 GHz up to 40 GHz for the shunt-capacitive switch and higher than -25 dB from dc up to 40 GHz for the shunt-resistive structure. The FEM simulated pull-down voltage is close to 14 V for the membrane without residual stress and less then 25 V for the pre-stressed membrane with a biaxial tensile stress of 20 MPa.

One of the main advantages of these switches is that the bias voltage has not to be applied between the center-conductor and the ground planes; hence no interference occurs with other semiconductor devices in a practical circuit. This separation between RF and dc signals allows modeling practical circuits more flexibly.

Dc-contact RF MEMS shunt-capacitive switches based on the proposed H-shape membrane have been introduced, simulated and optimized for S- and L-band applications. The S-band MEMS shunt-capacitive switch has been designed by forming a MIM structure directly on the center signal line so that the actuated bridge realizes a dc-contact with the top electrode of the MIM capacitor. The bridge shape and the conductor line at the contact location have been modified to reduce the up-state capacitance and avoid the stiction problem. The S-band switch provides an ON-state insertion loss less than 0.3 dB with a return loss higher than -25 dB from dc up to 35 GHz. The simulated OFF-state isolation is higher than -20 dB from 1.5 GHz up to 35 GHz. The predicted OFF/ON-state capacitance ratio is higher than 3.8×10^3. The simulated pull-down voltage lies in the range from 9.0 V to 12 V for a membrane with a biaxial tensile stress of 20 MPa. Even for a residual stress of 40 MPa the pull-down voltage does not exceed 15 V.

Finally, the base switch model has been redesigned to meet the requirements of a low-actuation voltage and a high isolation for L-band applications. The dielectric on ground (DOG) approach has been used to enlarge the capacitive coupling. The EM simulation shows an ON-state insertion loss less than 0.8 dB with a return loss higher than -40 dB from dc up to 40 GHz. The isolation in the OFF-state is higher than -20 dB from 0.8 GHz up to 40 GHz. A method to reach the out-of-plane profile of the membrane is proposed. The electromechanical simulation shows pull-down voltages of 9.0 V and 12.0 V for membranes with biaxial tensile stresses of 20 MPa and 40 MPa, respectively.

The proposed designs of RF MEMS switches are completely based on fabrication facilities.

Chapter 4

Fabrication of Fixed-Fixed Beam MEMS Shunt-Capacitive Switches

In this chapter, the fabrication process of conventional RF MEMS switches with a fixed-fixed beam configuration will be described. The fabrication of low-stress thin-film materials and high quality dielectric films is highly dependent on the process conditions and on the used equipment.

Two designs of fixed-fixed beam shunt-capacitive RF MEMS switches in CPW configuration presented in [76] and [24] have been fabricated on high resistivity (> 4 kΩ·cm) silicon substrates using standard fabrication processes compatible with complementary metal oxide semiconductor (CMOS) technology. Each fabrication step will be described and investigated in this chapter. The optimized process parameters will be presented. Finally, the fabricated switches are measured and the obtained results are compared to the simulations.

4.1 Fabrication Process

4.1.1 Switch Designs

The fabrication process of the conventional capacitive RF MEMS switches with a fixed-fixed beam configuration includes surface micromachining compatible with standard CMOS technology. Two designs of RF MEMS shunt-capacitive switches described in [76] (Figure 4.1 (a), labeled type A) and in [24] (Figure 4.1 (b), labeled type B) have been fabricated in a standard clean-room. The dimensions of the structures are listed in Table 4.1. The moveable membrane of the switch of type A has a simple rectangular shape. The movable membrane of the RF MEMS switch of type B has a bowtie shape as shown in Figure 4.1 (c). Notice that holes with a diameter of 2.0 μm (not shown in Figure 4.1) are added to the membrane in order to decrease the damping effect, to reduce the residual stress in the membrane and to facilitate a removal of the sacrificial layer. The switches have been fabricated on high-resistivity (> 4 kΩ·cm) silicon substrates.

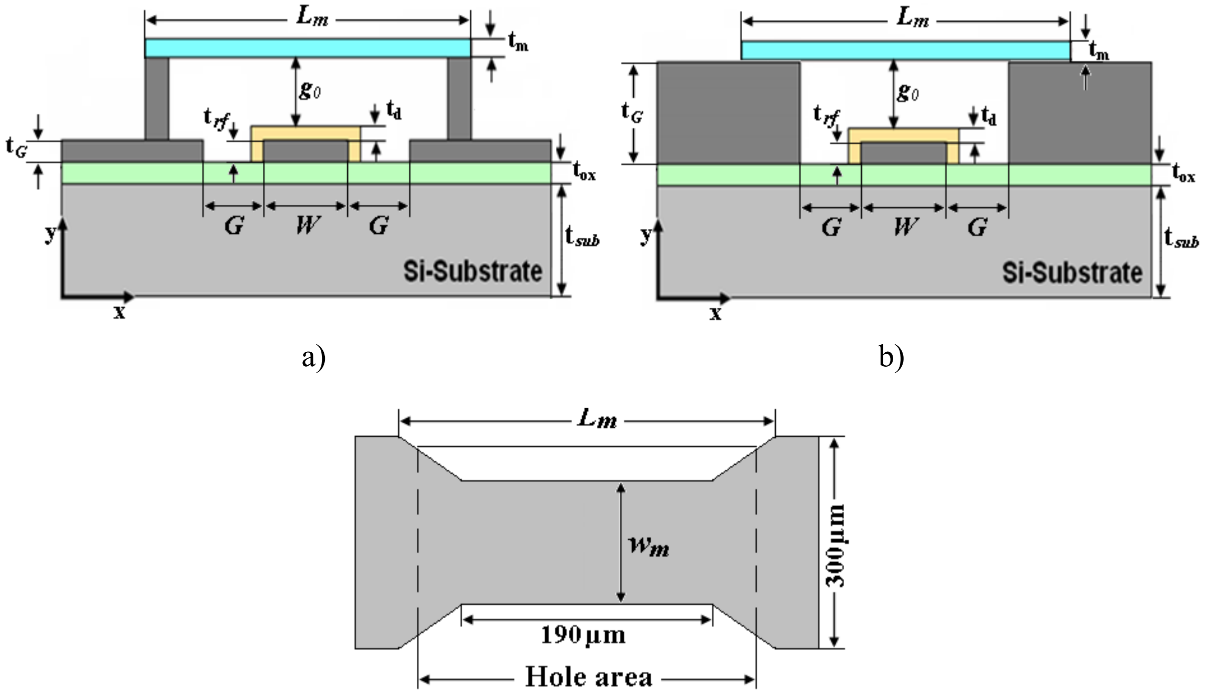

a) b)

c)

Figure 4.1: Schematic diagrams of the RF MEMS capacitive switch: (a) type A, (b) type B and (c) membrane shape of the switch of type B.

Table 4.1 Dimensions of RF MEMS switches of type A and type B

Parameters		**Switch Type A**	**Switch Type B**	**Materials**
$G/W/G$	(µm)	60/100/60	80/120/80	*Al*
t_{sub}	(µm)	625	625	*Si*
t_{ox}	(µm)	1.0	1.0	SiO_2
t_{rf}	(µm)	0.8	0.8	*Al*
t_G	(µm)	0.8	2.85	*Al*
g_0	(µm)	1.5	2.0	-
t_d	(nm)	60	60	*SiN*
L_m	(µm)	300	310	*Al*
t_m	(µm)	1.0	0.7	-
W_m	(µm)	60-100	100	-

4.1.2 Fabrication Steps

The switch designs need only four lithographic masks as shown in Figure 4.2. The following technology steps have been performed to fabricate the RF MEMS shunt-capacitive switches of type A and type B:

Step 1: Cleaning of the silicon substrate;

Step 2: Wet thermal oxidation to grow a silicon dioxide buffer layer;

Step 3: PVD of an *Al/Cr* thin metal bi-layer for the CPW lines;

Step 4: Patterning of the *Al/Cr* bi-layer by wet etching to form the CPW (Figure 4.2 (a));

Step 5: ECR-PECVD of silicon nitride as a dielectric layer for the capacitive coupling;

Step 6: Patterning of silicon nitride by dry etching (Figure 4.2 (b));

Step 7 (*Only for switch of type B)* PVD of *Al* for CPW ground planes;

Step 8 (*Only for switch of type B)* Patterning of Al to form CPW ground planes;

Step 9: Deposition and patterning of the sacrificial layer (Figure 4.2 (c));

Step 10: PVD of *Al* for the membrane;

Step 11: Patterning of *Al* film by dry etching to form the membrane shape (Figure 4.2 (d));

Step 12: Removal of the sacrificial layer by dry etching (Figure 4.2 (e)).

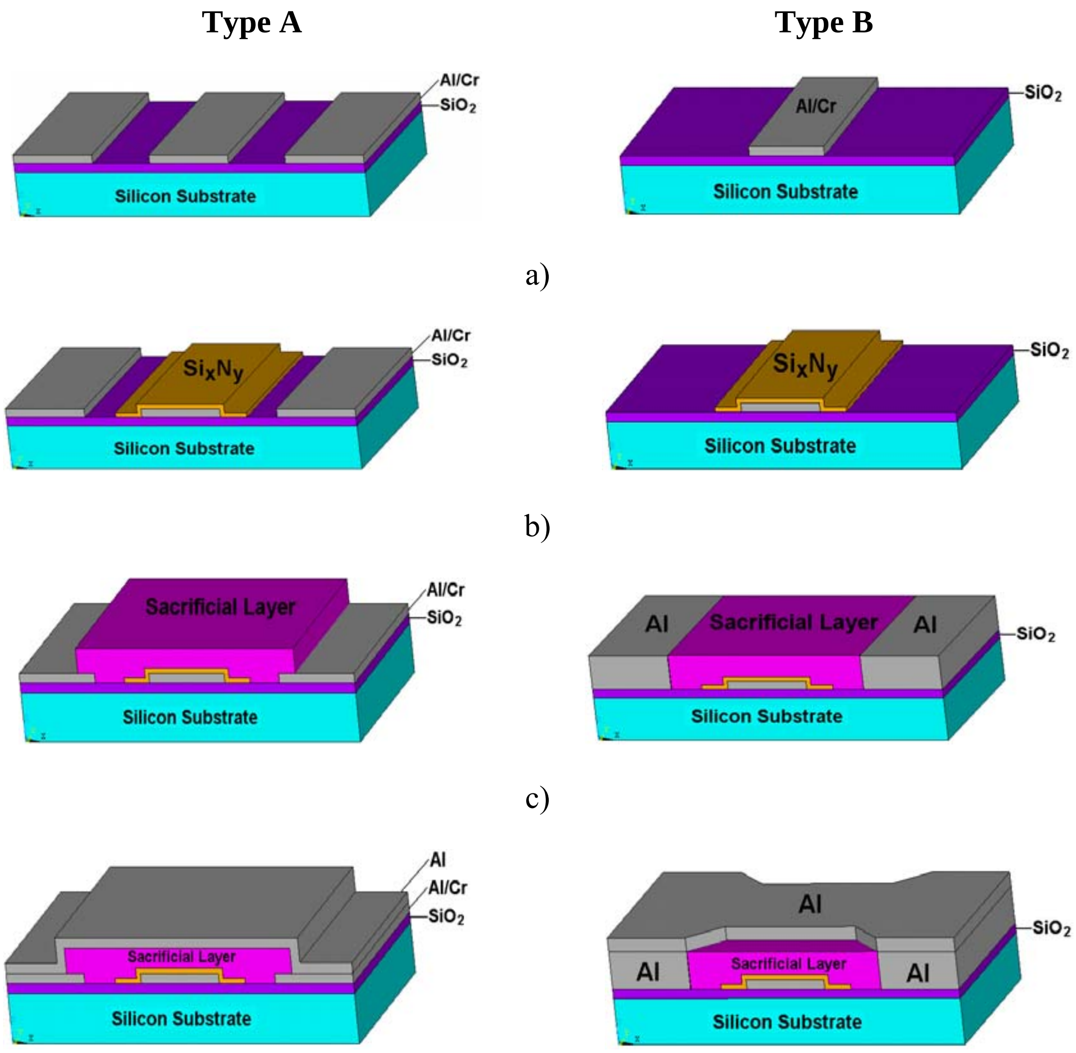

a)

b)

c)

d)

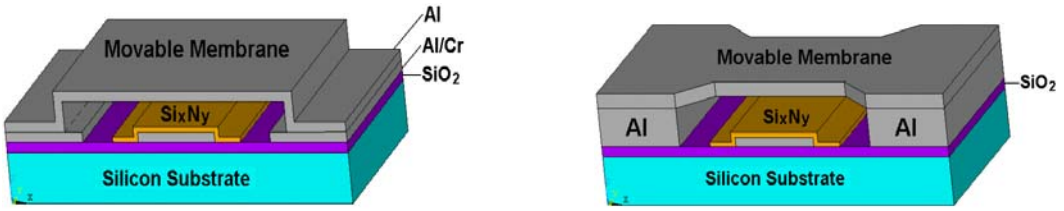

e)

Figure 4.2: Fabrication flow of RF MEMS capacitive switches: (a) PVD process for the CPW lines; (b) PECVD and patterning of the dielectric layer; (c) PVD of *Al* for the switch of type B, spin coating and patterning of the sacrificial layer for both switches; (d) PVD and dry etch processes to form the membrane; and (e) removal of the sacrificial layer by dry etching.

4.1.2.1 Cleaning and Wet Thermal Oxidation of the Silicon Substrate

The first step in the fabrication flow for both types of RF MEMS switches was cleaning of the silicon substrate by Caro’s acid (H_2SO_4:H_2O_2 ≡ 2:1; prepared using 96% H_2SO_4 and 32% H_2O_2) at T = 120 °C for 5 min. After the treatment with Caro’s acid, the wafers were dipped for 1 min in diluted hydrofluoric acid (0.5% HF). Then the silicon dioxide buffer layer was grown by wet thermal oxidation in a Centrotherm hot wall oxidation furnace. (T=1100 °C, t = 50 min, oxygen flow 3 slm and hydrogen flow 5 slm) (step 2).

4.1.2.2 PVD and Patterning of Al/Cr to Form the CPW Lines

The PVD equipment used in the switch fabrication was a Balzers BAK 600 [179] which is a conventional e-gun evaporation system. The metal deposition procedure was carried out at a base pressure of 10^{-6} mbar with a deposition rate of about 1.0 nm/sec. An *Al/Cr* bi-layer was evaporated and patterned to form the CPW lines (step 3). A thin layer of chromium was deposited on top of *Al* in order to avoid the formation of *Al* hillocks.

The wet etch process (step 4) was performed using a chromium etch mixture (ammonium nitrate – 20 mass% and acetic acid – 4 mass% in DI H_2O) to etch the *Cr* layer and a phosphorous acid mixture (ortho-phosphorous acid - 63 mass%, acetic acid - 20 mass% and nitric acid - 3 mass% in DI H_2O) to etch the *Al* layer. The wet etching is commonly an isotropic process and etches equally in all directions. Therefore, all the line widths were oversized by 2.0 µm to compensate a decrease after the wet etching. Sharp lines have been obtained as shown in Figure 4.3.

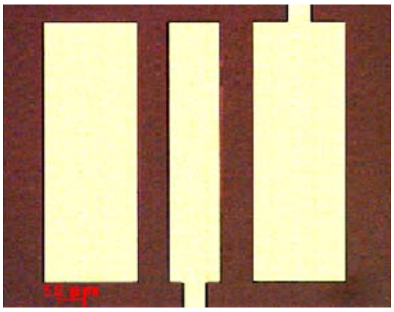

Figure 4.3: Microphotograph of *Al/Cr* metal lines patterned by wet etching.

4.1.2.3 Deposition and Characterization of the Dielectric Film

The step 5 in the fabrication flow for both types of MEMS switches is the deposition the dielectric layer. Silicon nitride was deposited on the center conductor line using a low temperature electron cyclotron resonance plasma enhanced chemical vapour deposition (ECR-PECVD) technique. Silane (SiH_4), nitrogen (N_2) gases were used as precursors of the deposition process and argon (*Ar*) as inert diluent.

Deposition Procedure of Silicon Nitride

The deposition equipment used in this work was a high-density plasma system equipped with an ECR source Roth&Rau MicroSys 350 [180]. Figure 4.4 shows a schematic diagram of the ECR-PECVD cluster module. In such a system a high density of ions and free radicals in the discharge is generated. It allows to significantly reduce the deposition temperature. In order to increase the energy of ions bombarding the surface the substrate chuck can be biased by applying RF (13.56 GHz) power.

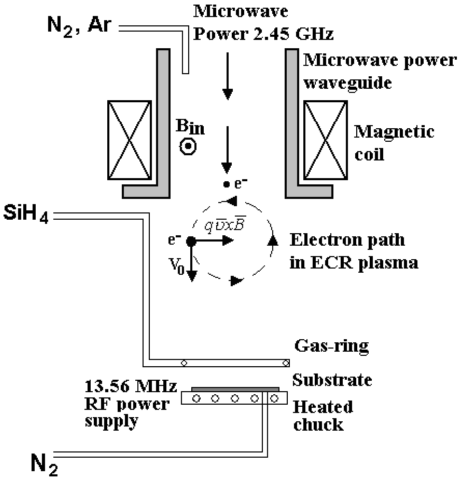

Figure 4.4: Schematic diagram of the ECR-PECVD system and the path of an electron in the plasma.

Nitrogen N_2 and argon Ar gases are fed directly into the ECR plasma, and silane SiH_4 is injected into the deposition chamber via a gas-ring around the perimeter of the substrate chuck. The substrate temperature is controlled by the heated chuck.

The deposition conditions used in this investigation are listed in Table 4.2. The microwave power, RF power, Ar flow and process pressure were 500 W, 1 W, 100 sccm, and approximately 2.5×10^{-2} mbar, respectively, and were kept constant for all experiments.

Table 4.2 Deposition parameters of silicon nitride films

Process	**SiH_4, (sccm)**	**N_2, (sccm)**	**T, °C**
1	5	30	50
2	7.5	30	50
3	30	30	50
4	15	30	20
5	15	30	100
6	15	30	200

Characterization of Deposited Silicon Nitride Thin Films

For an optimization of the deposition parameters and an investigation of the obtained silicon nitride film MIM capacitors were fabricated on *p*-type *Si* <100> substrates covered by a 1.0 μm thick silicon dioxide. Aluminum films with a thickness of 0.2 μm were used as electrode materials. The top contacts had circular-shapes with areas from 0.031 mm^2 up to 0.785 mm^2.

The dielectric properties of the deposited films were evaluated by current-voltage (*I-V*) and capacity-voltage (*C-V*) measurements. The *I-V* and *C-V* (at 1.0 MHz) measurements were carried out using a programmable sub-femtoampere electrometer (Keithley 6430) and a precision *LCR* meter (Agilent 4284A), respectively.

The thickness and the refractive index of the deposited films were measured by ellipsometry (SE 850, Sentech) in the wavelength range from 248 nm to 869 nm with an incidence angle of 70° and evaluated using Cauchy's model. The film thickness uniformity was estimated over the full wafer size using the "Wafermap" mapping software from Boin GmbH. The film composition was analyzed by X-ray photoelectron spectroscopy (XPS) with a Perkin Elmer PHI 5600 ESCA system, using Mg Kα (1253.6 eV) X-radiation with an input power of the excitation source of 400 W. The film roughness was measured using an atomic force microscope (AFM) (Nanotop-2006) operating in contact and tapping modes.

The deposition features, physical and electrical properties of the deposited silicon nitride films are summarized in Table 4.3. The average thickness of the deposited films is 50 nm.

Table 4.3 Deposition features, physical and electrical properties of deposited Si_xN_y films

Process	**Dep. rate, (nm/min)**	**Film thickness uniformity, (%)**	**Roughness, R_a (nm)**	**Refr. index**	***N/Si* ratio**	ε_r
1	6.8	2.3	≈ 2.25	1.79	1.34	6.2
2	8.1	2.1	≈ 2.17	1.87	1.29	6.6
3	14.6	1.96	≈ 1.15	2.22	0.89	7.9
4	11.8	1.92	≈ 2.1	1.89	1.17	6.9
5	11.4	2.0	≈ 2.2	1.9	1.19	7.0
6	10.3	2.1	≈ 2.2	1.9	1.20	7.0

One of the most important factors that influence the dielectric film quality is the silane to nitrogen ratio. In our experiments the nitride films were deposited with ratios of SiH_4/N_2 of 1:6, 1:4, 1:2 and 1:1.

XPS results summarized in Table 4.3 show that the concentration of nitrogen in the film was lowered when the silane flow was increased (see Tables 4.2). A higher silane flow, i.e. an increase of the SiH_4/N_2 ratio, increases the concentration of reactive silyl species (SiH_2) in the chamber. Due to the low process chamber pressure no significant gas phase reaction can occur between both precursors resulting in a reduction of the *N/Si* ratio in the deposited film. This was verified by experiments: silicon nitride deposited with $SiH_4/N_2 = 1:1$ is silicon-rich see process 3 in Tables 4.2 and 4.3. The deposition rate of the dielectric film increased if the N_2/SiH_4 ratio decreased indicating that the formation of the film was limited by the silane species in the ECR plasma. It could also be observed that the deposition rate slightly decreased if the process temperature was increased. This is due to more dense films at higher deposition temperatures as the concentration of hydrogen incorporated in the film decreases. The refractive index of the deposited silicon nitride also depended on the *N/Si* ratio in the film; at values higher than 1.9 the silicon nitride is silicon-rich what could be confirmed by ellipsometry and XPS measurements. The film uniformity over the whole wafer was measured for each of the deposition conditions and ranged from 1.92% to 2.3%. This satisfies the requirements of microfabrication. A radial variation of the thickness was observed with a maximum thickness at the center of the substrate. It is known that the uniformity of the deposited film depends on the uniformity of the plasma profile in an ECR-PECVD chamber [109]. Mapping of the thickness of the nitride film deposited with process 3 is shown in Figure 4.5 (a). Notice that the mapping was obtained by the measurement of 18 points in two perpendicular directions over the wafer (cross-measurement). The average roughness of the deposited films decreased from 2.25 nm to 1.15 nm as the SiH_4/N_2 ratio was increased from 1:6 to 1:1. This may be due to the higher surface diffusion of silicon atoms [181]. The better mobility of the adatoms leads to a smoother surface and a densification of the film; such phenomena have been observed and described in [181, 182]. The AFM image of the sample obtained with process 3 is shown in Figure 4.5 (b).

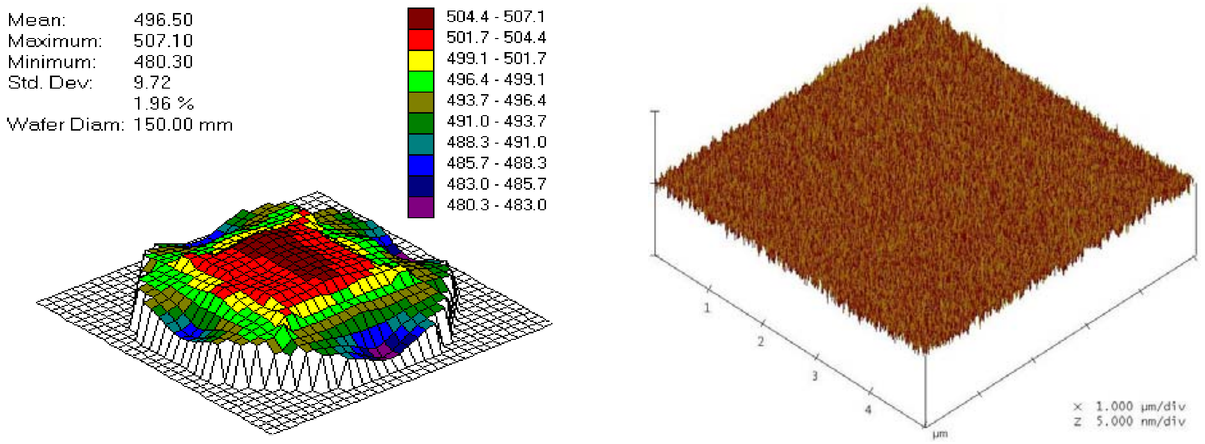

a) b)

Figure 4.5: Mapping of the thickness (a) and (b) AFM image of the silicon nitride film deposited by ECR-PECVD with process 3.

Figure 4.6 (a) shows the results of *C-V* measurements on MIM structures with an area of the top electrode of 0.785 mm^2 for different deposition conditions. It can be seen from the measurement results (see Figure 4.6 and 4.7 (a)) that the capacitance was substantially independent of the applied voltage (value and polarity), only depending on the dielectric properties of the film and the areas of the electrodes. The dielectric constant of the deposited film can be easily calculated using the conventional parallel plate model:

$$C = \frac{\varepsilon_0 \varepsilon_r A}{t_d} \tag{4.1}$$

where ε_r is the dielectric constant, ε_0 is the free space permittivity, A is the active area and t_d is the dielectric film thickness. Figure 4.7 (b) shows a plot of the capacitance as a function of the electrode area at zero bias voltage for the nitride film deposited with process parameters 3. It can be seen that there is a linear relationship between C and V and Eqn. (4.1) is valid. From the slope of the curve, giving a value of $\varepsilon_r\ \varepsilon_0/t_d$ of 1.4×10^{-3} F/m^2, the permittivity ε_r of the dielectric film was calculated to be 7.9. The same procedures were carried out to determine the dielectric constants for all samples (see Table 4.3).

Due to the higher silicon content the silicon-rich nitride had a higher dielectric constant than the nitrogen-rich one.

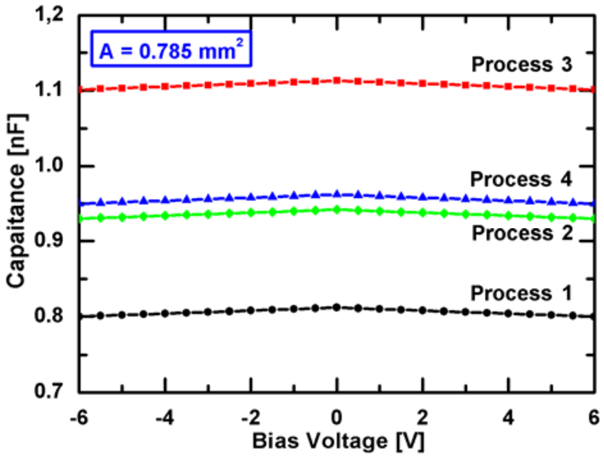

Figure 4.6: Dependence of capacitance on voltage for MIM structures with an area of the top electrode of 0.785 mm^2 fabricated with different deposition parameters.

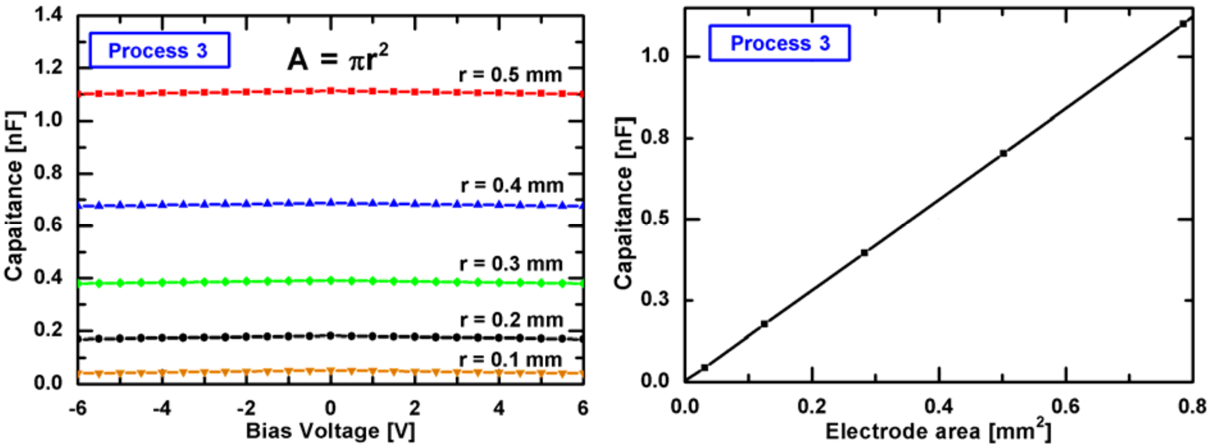

a) b)

Figure 4.7: Dependence of capacitance on voltage for MIM structures fabricated with process parameters 3 vs. top electrode areas (a) and capacitance as function of top electrode area at zero bias voltage for process 3 (b).

In order to study the insulating properties of the deposited films, current-voltage characteristics have been measured. Figure 4.8 shows the *I-V* characteristics obtained for a capacitor area of 0.785 mm^2 with silicon nitride films deposited with processes 1, 2 and 3. It was defined that the dielectric breakdown of the MIM structures had happened if a leakage current of 100 nA was reached. The corresponding average breakdown voltages of the nitrogen-rich films of processes 1 and 2 were 40 V and 37 V, respectively, and were higher than for the silicon-rich films having values of 29.5 V. For a capacitor area of 0.785 mm^2 and a film thickness of about 50 nm these voltages are corresponding to electric field strengths of 7.9 MV/cm, 7.4 MV/cm, and 5.9 MV/cm for the processes 1, 2 and 3, respectively. The breakdown field strength for the processes 4-6 is close 7.5 MV/cm. The silicon-rich nitride films had a higher conductivity and, thus, a lower breakdown voltage.

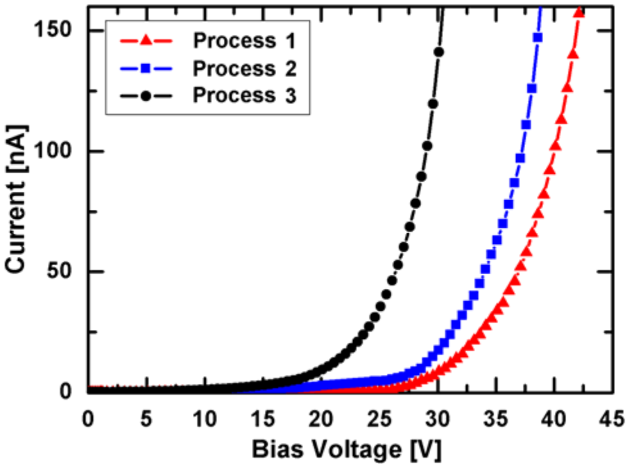

Figure 4.8: Dependence of leakage current on voltage for MIM structures with an effective area of 0.785 mm^2 fabricated with different process parameters.

The FEM predicted actuation-voltage of both types of RF MEMS switches with a 60 nm thick dielectric layer is not higher than 32 V even for a value of 30 MPa of residual stress in the metal membrane. This voltage value and the above film thicknesses correspond to an electric field strength of 5.3 MV/cm which is lower than the breakdown field of all investigated silicon nitride films. The silicon nitride film deposited in process 3 was chosen for the fabrication of the switches as it exhibited a higher dielectric constant and better physical properties such as a surface roughness in comparison to the films of the other processes.

4.1.2.4 Patterning of Silicon Nitride Film

Reactive ion etching (RIE) was carried out to etch the deposited silicon nitride layer (step 6). AZ6612 positive photoresist with a thickness of 1.2 µm was spin coated and patterned on the nitride surface.

RIE Process

A scheme of a parallel plate RIE system is shown in Figure 4.9. In this reactor the neutral electrode is attached to the chamber wall to enlarge its effective electrode area. Therefore, a higher potential can be created between the plasma and the powered electrode thus increasing the energy of the ion bombardment [183]. For a pressure in the reactor higher than 1 Torr the plasma compresses and loses contact with the walls. Therefore, RIE should be done with low pressure condition, where the mean free path is in the order of millimeters and the plasma stays in good contact with the chamber walls.

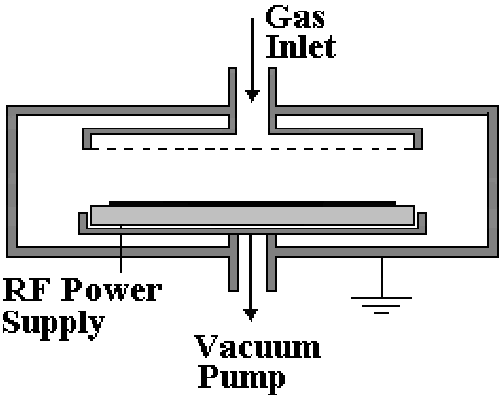

Figure 4.9: Conventional parallel plate RIE system.

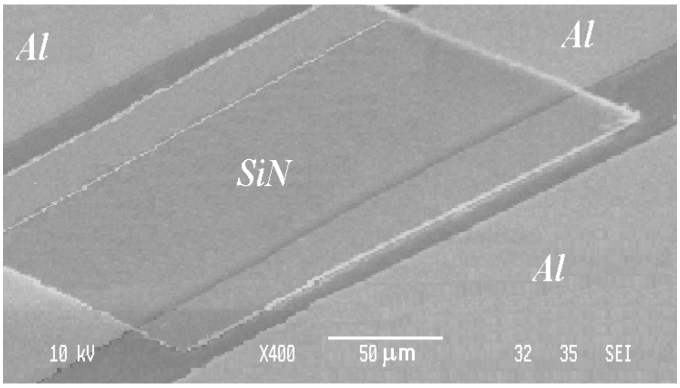

Figure 4.10: SEM image of a silicon nitride film deposited on the center conductor of a CPW and patterned by RIE.

In our case a high anisotropy of the etch process is not needed, because the dielectric layer is larger than the real capacitive contact area under the metal bridge. However, etch selectivity plays an important role as the undesired nitride has to be removed without damaging the metallization laying beneath the nitride. A CHF_3-CF_4-O_2 gas mixture was used to etch the silicon nitride in a STS C 071 RIE system [184]. The gas flows of CHF_3, CF_4 and O_2 were 70, 20 and 5 sccm respectively, the susceptor temperature was 20 °C, the process pressure 50 mTorr, the base pressure 1.0 mTorr, and the RF power 100 W. The measured etch rate was about 1.8 nm/sec. A SEM image of a RIE patterned silicon nitride film is shown in Figure 4.10.

4.1.2.5 PVD and Patterning of Aluminum to Form CPW Ground Planes (*Only for Switches of type B*)

The *Al* layer with a thickness of 2.85 µm has been deposited by PVD process and patterned by wet etching to form the ground planes of the RF MEMS switch of type B as shown in Figure 4.2 (c). The process parameters were the same as outlined in section 4.1.2.2.

4.1.2.6 Fabrication of the Membrane

Spin Coating and Patterning of the Sacrificial Layer

Step 6 in the fabrication flow of both switches is spin coating and patterning of the sacrificial layer. As sacrificial layer a positive photoresist film AZ6612 with a thickness of 1.6 µm for switch of type A and of 2.9 µm for switch of type B was spin coated, patterned and developed. In detail, the following steps were carried out:

- Dehydration bake for 120 min at 140 °C;
- HMDS evaporation for 10 min at 80 °C;
- Spin coating of the photoresist AZ6612 at 1800 rpm for 30 sec;
- Soft bake at 90 °C on a hotplate for 60 sec;
- Image exposure;
- Development in AZ 726 MIF;
- Post bake at 120 °C on a hotplate for 45 min.

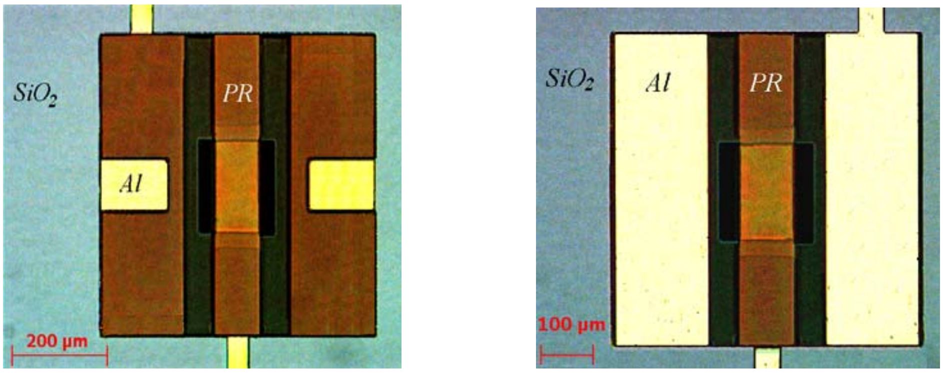

a) b)

Figure 4.11: Microphotographs of the RF MEMS switches with a patterned sacrificial layer: (a) the switch of type A and (b) the switch of type B.

Figure 4.11 shows the microphotographs of the RF MEMS switches of type A and B with the patterned sacrificial layer. The final thicknesses of the photoresist were approximately 1.55 µm and 2.85 µm for the switches of type A and B, respectively.

PVD and Patterning of the Al Layer

After patterning of the sacrificial photoresist, a layer of *Al* (1.0 µm – type A and 0.7 µm – type B) was evaporated and patterned forming a metal bridge with the last mask as shown in Figure 4.2 (d). The aluminum films were structured is a dry etching process to form the membrane shapes using a Sentech RIE cluster [185]. The following parameters were: process pressure 18 Pa, substrate temperature 60 °C, RF power 150 W and a gas flow ratio of Cl_2/BCl_3 of 1:6. The etch selectivity of the AZ6612 positive photoresist to aluminum was 1:1.

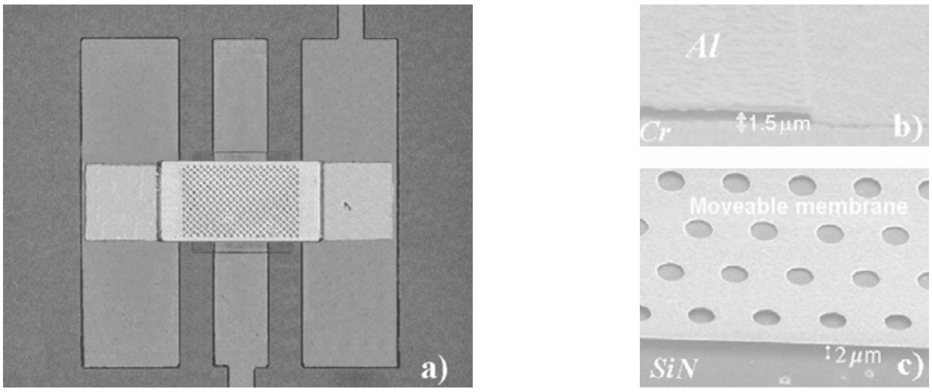

Figure 4.12: Microphotograph of the top view of the fabricated RF MEMS switch of type A (a). SEM images of the realised membrane of a switch of type A: (b) view on the post of the membrane and (c) view on the membrane over the substrate.

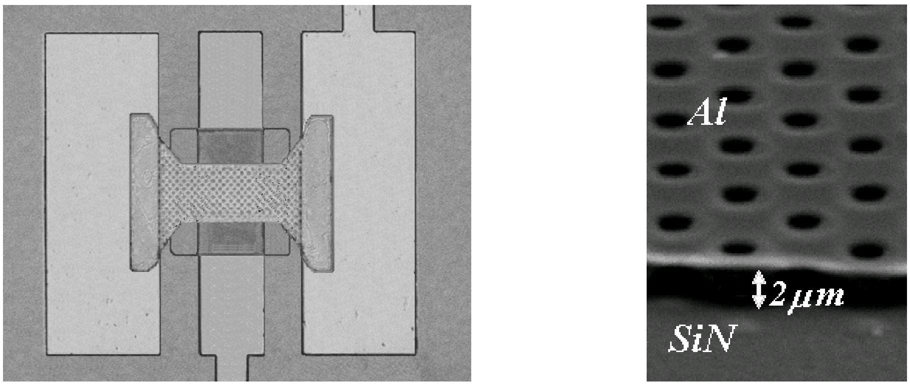

a) b)

Figure 4.13: Microphotograph of the fabricated RF MEMS switch of type B (a). SEM image of the realised membrane of a switch of type B over the central line (b).

Removal of the Sacrificial Layer

The final step in the switch fabrication flow is the etching step to remove the sacrificial layer and to release the metal membrane. A dry etching in an oxygen plasma was performed to remove the sacrificial layer in a Sentech RIE cluster. The total etching time was 45 min with an O_2 flow of 120 sccm. Microphotographs of the fabricated RF MEMS switches of type A and of type B are shown in Figure 4.12 and Figure 4.13, respectively. It can be seen that the suspended bridge structure is realised for both switches using the reported CMOS compatible technology.

4.2 Simulation and Measurement Results

In this section, the simulated and measured results of the fabricated RF MEMS switches of type A and type B are presented. The electrostatic-structural simulations were carried out with the FEM simulator ANSYS Multiphysics 9.0 [91] and the electromagnetic simulations with MoM EM simulators Sonnet [159] and Microwave Office [160], see chapters 2 and 3. The fabricated RF MEMS switches were contacted to a Suss MicroTec PM5 probe station [186] in order to measure the S-parameters. The RF measurements were performed with a HP 8722D vector network analyzer. External voltage for the switch actuation was applied by a Keithley 6430 source measurement unit. The *RLC* values of the switches were extracted from the S-parameter measurements by a fit to the simulated responses.

EM Measurements, Simulation and Fitting CLR Parameters

Both switches were implemented on CPW lines with a characteristic impedance of $Z_0 = 50\ \Omega$. The measured and the fitted frequency responses of the RF MEMS switch of type A for different bridge widths are shown in Figure 4.14. The measured and the fitted S-parameters of the switch of type B are depicted in Figure 4.15. The fit was carried out using the lumped-element model described in chapter 1 by changing the value of the shunt capacitance. The measurements show that the ON-state insertion loss S_{11} of all switches is less than 0.5 dB and the return loss is less than -10 dB up to 40 GHz. The OFF-state isolation is higher than -18 dB for the switch of type A and higher than -20 dB for the switch of type B for frequencies from 6.0 GHz up to 40 GHz.

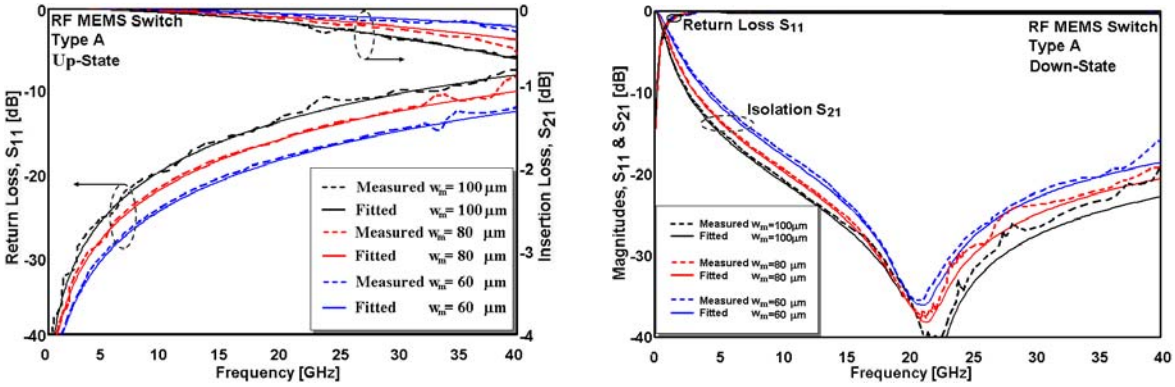

a) b)

Figure 4.14: Measured and fitted S-parameters of the RF MEMS shunt-capacitive switch of type A for different bridge width: (a) up-state and (b) down-state.

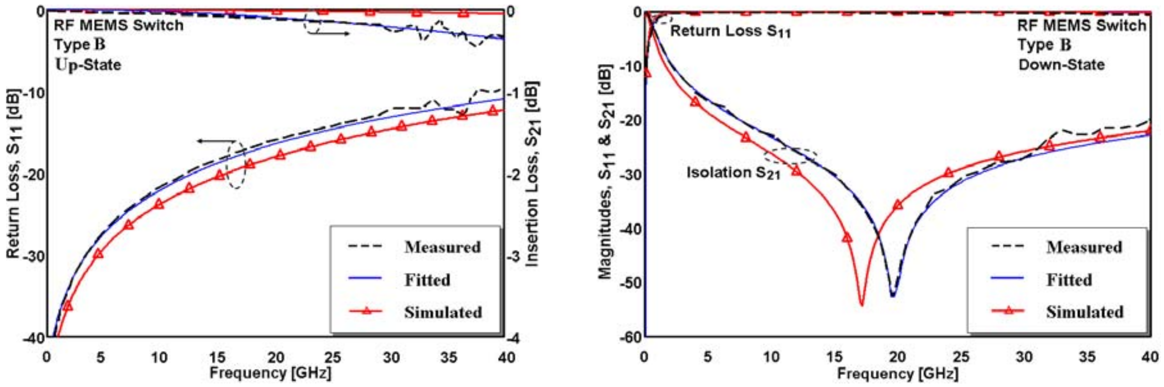

a) b)

Figure 4.15: Measured, simulated and fitted S-parameters of the RF MEMS shunt-capacitive switch of type B: (a) up-state and (b) down-state.

The up-state capacitance C_u can be extracted from the measured reflection coefficient S_{11} and for $S_{11} \leq -10$ dB it is given by [39]:

$$C_u \approx \frac{2|S_{11}|}{\omega Z_0} \tag{4.2}$$

Table 4.4 summarises the capacitance values extracted from the measurements (C_u) and calculated using a simple parallel plate model (C_{pp}). It can be seen that the difference between these values for the switch of type A increases from 29% to 40% as the bridge width decreases. This is due to the fringing capacitance which has a higher influence as the capacitance area is decreased. For this reason the diameter of holes in the membrane plane should be less than $2 \cdot g_0$ in order to not affect the total capacitance value. The bridge inductance and resistance were not fitted for the up-state because their influence on the frequency response is negligible.

Table 4.4 Calculated and measured capacitance values

	Up-state				Down-state	
w_m, µm	C_{pp}, fF	C_u, fF	ΔC, fF	$\Delta C/C_{pp}$, %	C_{pp}, pF	C_d, pF
100	56.5	72.8	16.3	29	11.66	8.8
80	45.2	60.9	15.7	35	9.33	6.17
60	33.9	47.4	13.5	40	7.0	4.7
Type B	51.4	65.3	13.9	27	14.0	11.63

The down-state capacitance C_d can be extracted from the measured transmission characteristic shown in Figure 4.14 (b) and Figure 4.15 (b). For S_{21} << -10 dB the down-state capacitance can be approximated as [39]:

$$C_d \approx \frac{2}{\omega Z_0 |S_{21}|} \tag{4.3}$$

The capacitance value must be extracted in the frequency range lower than $f_0/2$ (f_0 is the resonant frequency) because the response in this range is controlled by a pure capacitance. The down-state capacitance values calculated by using the parallel plate model and those extracted from the measurements are also listed in Table 4.4. The measured down-state capacitances were smaller than the calculated ones. The capacitance area of the experimental samples is reduced by the holes in the moveable membrane; additionally, the surface roughness will contribute to a not perfect contact of the membrane to the dielectric film resulting in a lower capacitance than calculated. With the down-state capacitance values, extracted from the measurements, the simulations were carried out to fit the simulated response to the measured S-parameters as depicted in Figure 4.14 (b) and in Figure 4.15 (b). The series inductance of the bridge controls the slope of S_{21}, therefore, it controls the position of the resonance frequency as shown in Figure 4.14 (b). Its value increases as the bridge width increases and depends on the portion of the bridge over the CPW slot. The series resistance of the bridge can be fitted best at resonance frequency where the switch impedance is $Z_s = R$ and S_{21} is given by [46]:

$$S_{21}\Big|_{f_0} \approx \frac{2R}{R+Z_0} \quad \Longrightarrow \quad R \approx \frac{S_{21} Z_0}{2-S_{21}} \tag{4.4}$$

The extracted values of bridge inductance and resistance are shown in Table 4.5. It is obvious that the resistance increases as the bridge width decreases. The bridge resistance controls the value of the rejection at the resonance frequency.

Table 4.5 Extracted inductance and resistance values

	Type A			Type B
w_m, μm	100	80	60	100
L, pH	6	9.2	11.8	5.7
R, Ω	0.15	0.33	0.4	0.065

Electromechanical Measurements and Analysis

The measured pull-down voltages were in the range of 24-26 V for the RF MEMS switch of type A and about 30 V for the switch of type B. As shown in chapter 1, the pull-down voltage can be calculated by the following expression [39]:

$$V_p = \sqrt{\frac{8k}{27\varepsilon_0 W w_m} g_0^3} \tag{4.5}$$

where k is the spring constant of the membrane. For the rectangular bridge it can be expressed as:

$$k = \frac{32 E t_m^3 w_m}{L_m^3} + \frac{8\sigma(1-v) t_m w_m}{L_m} \tag{4.12}$$

where E is Young's modulus (E = 70 GPa for *Al*), v is Poison's ratio (v = 0.35 for *Al*), and σ is the residual tensile stress in the membrane. Using the equations above the theoretically calculated spring constant of the membrane of the switch of type A for the bridge width of 100 μm is 55 N/m; this corresponds to a residual tensile stress of 31 MPa. The geometrical shape of the membrane of the switch of type B does not satisfy the requirements of the model described above. Therefore, 3-D FEM simulations were carried out for both types of MEMS switches in order to extract the residual stress value in the metal bridge. The simulated results gave values of the tensile stress of 27-28 MPa for both types of switches. It can be seen that the simulated stress is in 3-4 MPa less than the calculated one which was obtained using a first order expression where the stress only in one direction was taken into account.

4.3 Summary

In this chapter the fabrication process of conventional RF MEMS switches with a fixed-fixed beam configuration was described. The switches were fabricated in a clean-room using surface micromachined techniques compatible with standard CMOS technology. Each fabrication step was described in details. High quality silicon nitride films were deposited using the ECR-PECVD method at 50 °C deposition temperature. The deposition parameters were optimized to get silicon nitride films with a relatively high dielectric constant, a high breakdown electric field strength and a low surface roughness. MIM capacitor structures were fabricated to determine the electrical properties of the deposited dielectric films. The refractive index and the film thickness were measured by ellipsometry. The surface roughness was analyzed by AFM. The dielectric constant and the breakdown voltage were determined by *C-V* and *I-V* measurements, respectively. XPS analysis was used to analyse the film composition. The influence of the gas mixture, namely the SiH_4/N_2 ratio, on the film properties was studied. The films grown at SiH_4/N_2 ratios of 1:6, 1:4 and 1:2 were nitrogen-rich while the films deposited with a ratio of 1:1 were silicon rich. The deposition rate increased if the SiH_4/N_2 ratio was increased. The refractive index and the dielectric constant of the nitride films decreased if the SiH_4/N_2 ratio was reduced. The average surface roughness of deposited films was lower for silicon-rich films. The measured breakdown field of a sample processed with a SiH_4/N_2 ratio of 1:6 was 7.9 MV/cm at J = 12 $\mu A/cm^2$ and decreased to 5.9 MV/cm for a ratio of 1:1. The measurements showed that the substrate temperature had almost no influence on the film properties.

Electromagnetic and electromechanical measurements of the fabricated RF MEMS switches were carried out in order to determine their properties. The measured ON-state insertion loss S_{11} for the all switches was less than 0.5 dB with a return loss less than -10 dB up to 40 GHz. The OFF-state isolation S_{21} was higher than -18 dB for frequency ranging from 6 GHz up to 40 GHz.

The measured pull-down voltage of the switch of type A was in the range of 24-26 V; for the switch of type B it was about 30 V. A FEM analysis was performed to estimate the residual stress in the metal membrane. The simulations showed that a value of the residual stress in the thin *Al* film deposited by PVD was about 27 MPa.

Chapter 5

Coplanar Microwave Filters

At first in this chapter two different types of coplanar bandpass filters (BPF) will be studied. The first one is designed as end-coupled $\lambda/4$ open-stub resonator. The second type is a new compact coplanar BPF with an inductively shunt-coupled approach using meander serpentine-shape $\lambda/2$ shunt-stubs which allow to increase the inductive load and, thus, to reduce the size of the filter.

Then, three different designs of coplanar filters based on defected ground structures (DGS) are presented. Several DGS shapes as resonator structures are investigated. The first one is a 2-D quasi-fractal periodic defected ground structure (PDGS) based on a conventional rectangular dumbbell shape. The second DGS possesses triangular arrowhead slots which have been cascaded to realize low-pass filters (LPF). The last designed structure is a new compact DGS LPF. This structure is based on $\lambda/4$ open-end stub resonators combined with DGS slot resonators.

All filter structures have been designed and characterized by EM as well as by lumped-element equivalent circuit simulations using the full-wave EM MoM simulators Sonnet [159] and Microwave Office [160]. The optimized filters were fabricated on ceramic substrates Ro4003c produced by Rogers Corporation with a dielectric constant of 3.38 ± 0.05, a loss tangent of 0.0027 and a thickness of 0.813 mm. Copper with a thickness of 35 µm is used as metallization. The fabricated structures are measured using a Hewlett Packard 8722D Vector Network Analyzer.

5.1 Design of Coplanar Bandpass Filter composed on Open-End Stubs

This section treats design, fabrication, measurements and characterization of compact end-coupled coplanar bandpass filters. EM simulation shows that the filters introduce very low insertion losses and are well matched in the pass-band. These results have been verified by measurements. The filters have been developed for the pass-band of 1.7-5.2 GHz.

5.1.1 Bandpass Filter Topology

Figure 5.1 (a) shows a schematic diagram of the designed bandpass filter structure. It consists of two symmetrical parts. Each part is composed of a *λ/4* conductor section followed by two parallel open-stubs of length *b*. These two parts are capacitively coupled through the gap *c*. The dimensions are as follows: length L = 15.0 mm, width H = 17.0 mm, a = 5.1 mm, b = 5.75 mm, c = 0.2 mm.

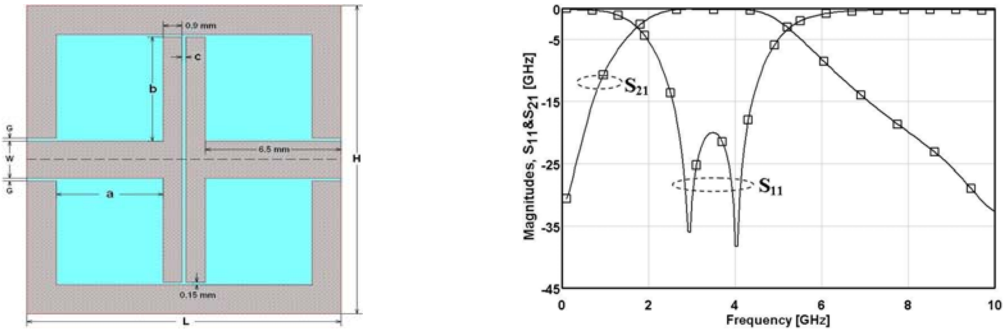

a) b)

Figure 5.1: Schematic drawing of the designed coplanar BPF (a) and its EM simulation results (b).

5.1.2 Electromagnetic and Equivalent Circuit Simulations

The CPW line used in this filter was designed for a characteristic impedance of 50 Ω. This impedance corresponds to $G = 0.2$ mm and $W = 2.8$ mm. The electromagnetic simulation result for the bandpass filter is shown in Figure 5.1 (b). The filter resembles two poles in the pass-band ranging from 1.7 GHz to 5.2 GHz and has a steep transition from the pass-band to the stop-band. The filter has a 3 dB bandwidth of 3.5 GHz. At the same time the filter shows a matching below -20 dB within a bandwidth of 1.5 GHz and has a reflection of less than -35 dB at the resonances. Figure 5.2 shows the current density distribution for the designed filter in the pass-band (4.0 GHz) and in the stop-band (10 GHz). It can be seen that at the pass-band the two ports are well coupled, while in the stop-band almost no RF power passes through the filter.

The filter structure has also been simulated with a lumped-element model which is shown in Figure 5.3. The conductor section is modeled as a series inductor L_s while the parallel *λ/4* stubs are modeled as an inductor L_p in series with a capacitance C_p. The gap between the two sections of the filter is modeled as a series capacitance C_0. Table 5.1 shows the values of the components of the equivalent circuit model. Figure 5.4 shows the simulation results obtained with EM and the lumped-element model. The results of both simulations are in good agreement.

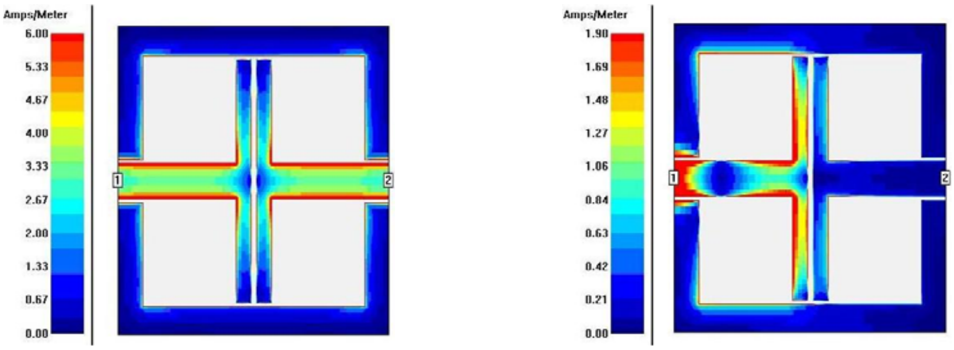

a) b)

Figure 5.2: Current density distribution in the designed BPF: (a) at 4 GHz and (b) at 10 GHz.

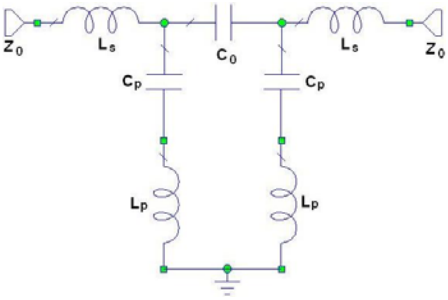

Figure 5.3: Equivalent circuit model for the designed BPF.

Table 5.1 Equivalent circuit parameters of the designed BPF	
Capacitance, C_0 (pF)	0.486
Capacitance, C_p (pF)	0.289
Inductance, L_s (nH)	3.46
Inductance, L_p (nH)	0.195

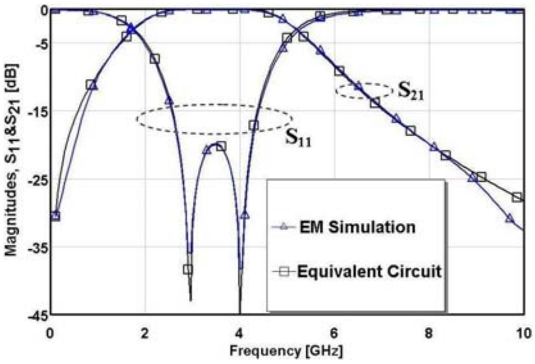

Figure 5.4: EM and equivalent circuit simulations of the designed BPF.

5.1.3 Effect of Geometrical Parameters

In order to investigate the dependence of geometrical dimensions on the filter properties, the EM simulation has been carried out for different values of the filter dimensions *a, b, c* (see Figure 5.1 (a)).

Figure 5.5 (a) shows the frequency response of the designed filter for values of the gap c = 0.1 mm, c = 0.2 mm and c = 0.3 mm, while values of a and b were kept constant. The gap c was changing by the change of the width of the open-stubs. Variation of the gap c affects only slightly the transmission within the pass-band, while the reflection significantly depends on c. In particular, a smaller value for c makes the transition from the pass-band to the stop-band steeper. The first resonance pole at 2.95 GHz is mainly controlled by the capacitive coupling between two resonators. Referring to the lumped-element model (Figure 5.3), an increase of the gap c almost linearly reduces the capacitance C_0 as shown in Figure 5.5 (b). Other lumped-element parameters do not change. The second pole in the pass-band at 4.0 GHz is slightly shifted due to the change of the open-stubs width. Consequently, the values of C_p and L_p in the equivalent circuit model change too.

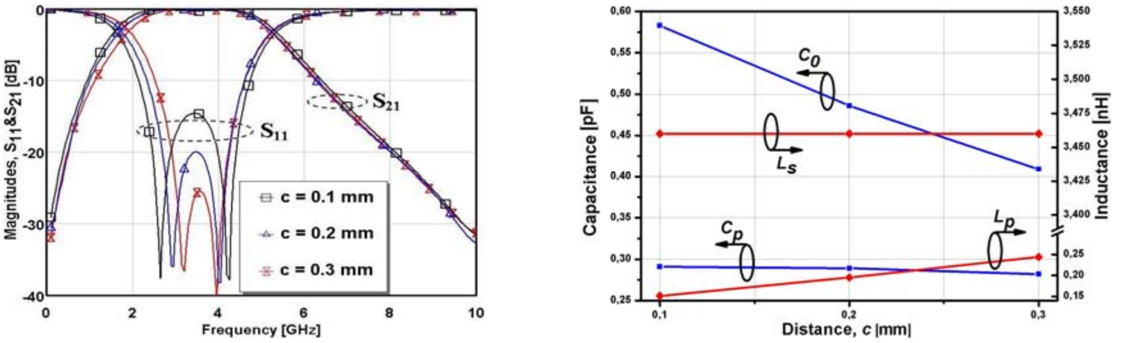

a) b)

Figure 5.5: EM simulations for different values of the gap c (a) and equivalent capacitances and inductances versus the gap c (b).

In Figure 5.6 (a) the impact of the open-stub length b on the filter response is presented. These simulations were carried out for the lengths b = 4.75 mm, b = 5.25 mm and b = 5.75 mm, while all other dimensions were kept constant. The length b affects the position of the pass-band but has very low influence on the bandwidth. Based on this result it can be concluded that the second resonance pole in the pass-band is controlled by the $\lambda/4$ open-stub resonators. As shown in Figure 5.6 (b), a change of the length b leads to a change of L_p and C_0 in the equivalent circuit model.

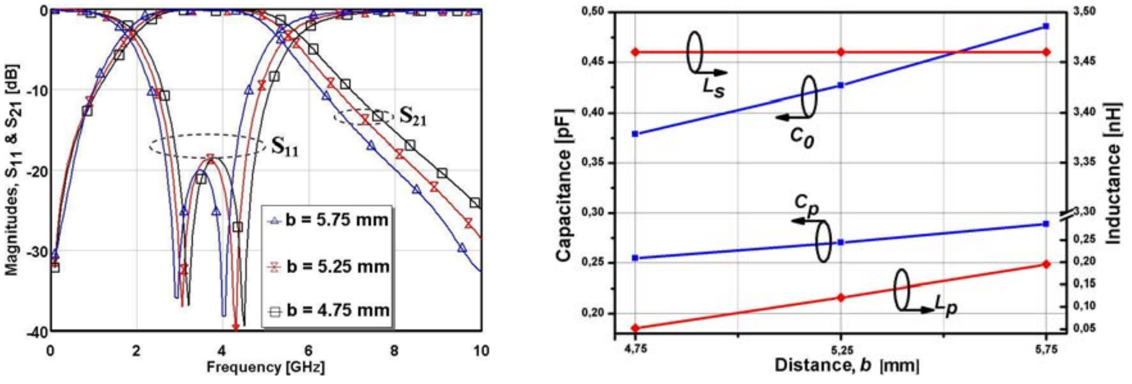

a) b)

Figure 5.6: EM simulations for different values of the length of the parallel open-stubs *b* (a) and equivalent capacitances and inductances versus the length *b* (b).

Finally, Figure 5.7 (a) shows the characteristics of the filter structure for three different values of the length of the conductor section *a* (see Figure 5.1 (a)). An increase of this geometric parameter leads to a slight decrease of the bandwidth, but the reflection is improved. *a* mainly affects the inductances L_s of the lumped-element model, as shown in Figure 5.7 (b). As *a* decreases the pass-band is shifted to higher frequencies. It should be mentioned that the width of the ground plane at the input and output ports are also changing with the parameter *a*.

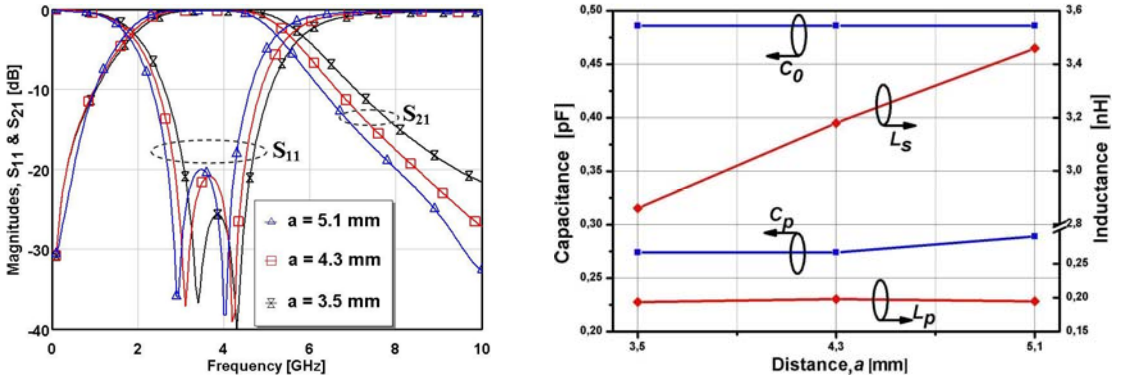

a) b)

Figure 5.7: EM simulations for different values of the *λ/4* conductor section *a* (a) and equivalent capacitances and inductances versus the conductor section *a* (b).

5.1.4 Measurement

The designed filter was fabricated and measured for frequencies from 0.5 GHz to 12.0 GHz. Figure 5.8 (a) shows a photo of the fabricated filter. The measurements can be seen in Figure

5.8 (b). The simulated results are in good agreement to the measured ones. The slight differences between both may be due to the tolerances in the fabrication procedure. The measured insertion loss in the pass-band is less than 1.0 dB with the return loss higher than -19 dB. The measured pass-band width is 3.8 GHz (1.8-5.6 GHz).

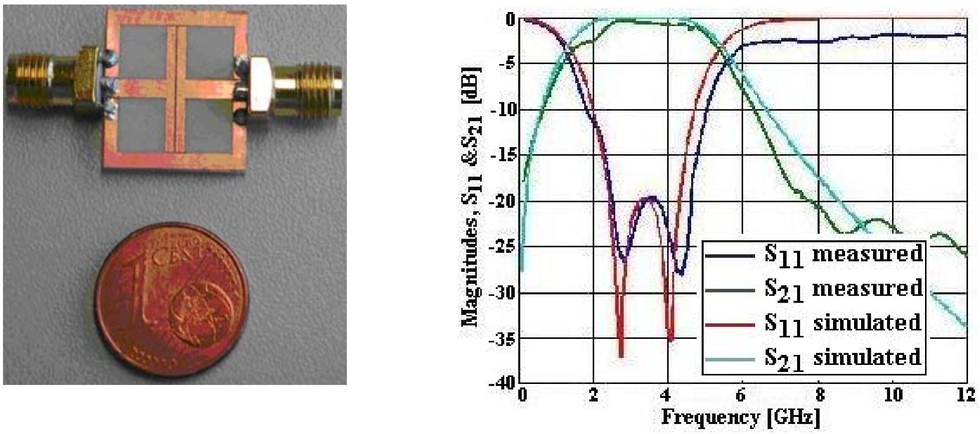

a) b)

Figure 5.8: Photo of the fabricated BPF (a) and its EM simulated and measured results (b).

5.2 Miniaturized Coplanar Bandpass/Bandstop Filter Using Meander Serpentine-Shape Shunt/Open-Stubs

In this section, a new type of compact coplanar bandpass filters with an inductively shunt-coupled approach using meander serpentine-shape shunt-stubs has been designed and investigated. The designed meander serpentine-shape shunt-stubs increase the inductive loading of the structure. Therefore, the resonant frequency is shifted to low frequencies. Finally, the designed bandpass filter has been transformed to the bandstop filter and described.

5.2.1 Bandpass Filter Structure

Figure 5.9 (a) shows a scheme of the designed bandpass filter structure. It consists of two symmetrical parts. Each part is composed of a $\lambda/2$ conductor section followed by two parallel meander serpentine-shape shunt-stubs. A detailed view of the meander serpentine-shape shunt-stub is shown in Figure 5.9 (b). These two parts are capacitively coupled through the gap c. The designed filter has the dimensions: a = 0.4 mm, b = 0.8 mm, h = 0.5 mm and c = 0.4 mm. The total area of the designed bandpass filter is 20×13.2 mm^2.

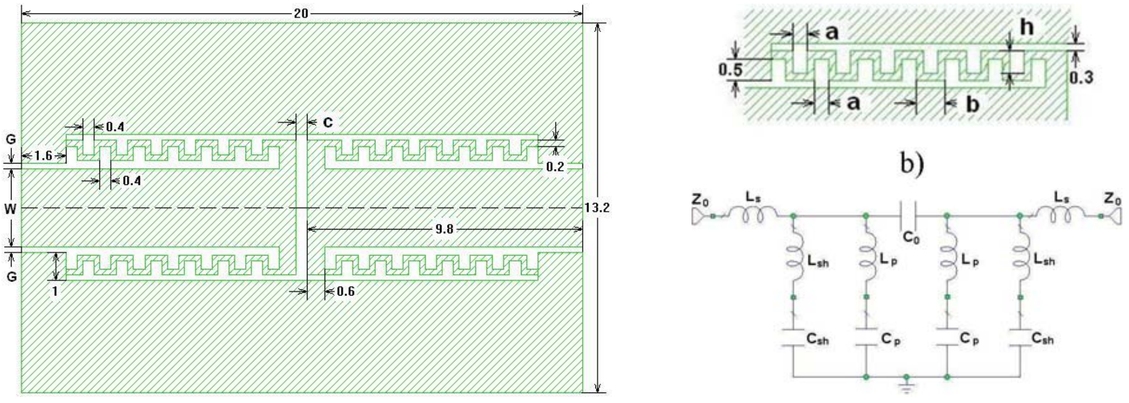

b)

a) c)

Figure 5.9: Scheme of the designed coplanar bandpass filter (a), detailed view of the serpentine-shape shunt-stub (b) and equivalent circuit model of the designed BPF (c).

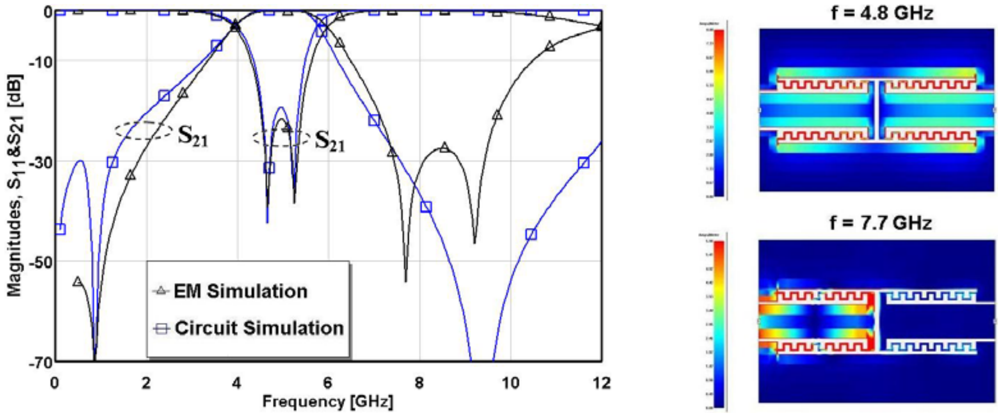

a) b)

Figure 5.10: EM and equivalent circuit simulations for the designed BPF (a) and current density distributions at 4.8 GHz and at 7.7 GHz (b).

5.2.2 Electromagnetic and Equivalent Circuit Simulations

The CPW line used in this filter was designed for a characteristic impedance of 50 Ω. This impedance corresponds to a signal line width of W = 2.8 mm and slot width of G = 0.2 mm. The simulation results for the filter are shown in Figure 5.10 (a). The designed filter has two poles and a steep transition from the pass-band to the stop-band. The 3 dB bandwidth of the BPF is 2.1 GHz (3.9-6.0 GHz); the filter shows a matching below -20 dB within a bandwidth of 1.0 GHz and has a reflection of less than -35 dB at the resonances. Figure 5.10 (b) shows the current distribution for the designed filter in the pass-band (4.8 GHz) and in the stop-band (7.7 GHz). At the pass-band the two ports are well coupled, while in the stop-band almost no

RF power passes through the filter. The simulated current density distribution at the transmission zero (7.7 GHz) in the upper stop-band clearly shows a minimum current at the middle of the serpentine-shape shunt-stubs. Therefore, according to the transmission line theory an inductively coupled shunt-stub has to be modeled as a series *LC* resonator. Figure 5.9 (c) shows the lumped-element model for the designed BPF. The *λ/2* transmission line conductor section is modeled as a series inductor L_s; the shunt-stubs are modeled as series connected inductor L_{sh} and capacitance C_{sh}. The open-end stubs are modeled as series connected capacitance C_p and inductance L_p. The gap between the two sections of the filter is modeled as a series capacitance C_0.

The shunt inductors can be modeled using the classical formula for ribbon inductors, which is given by [131]:

$$L_{sh} = 2l\left(\ln\left(\frac{2\pi}{w}\right) - 1 + \frac{w}{\pi l}\right) \quad \text{[nH]} \tag{5.1}$$

where *w* and *l* (in centimeters) are the width and the length of the inductor, respectively. The serpentine-shape ribbon inductor allows to increase the inductor effective length and, thus, to increase the shunt inductance. The shunt capacitance of the short circuit *λ/2* line can be calculated as [157]:

$$C_{sh} = \frac{1}{\omega_{z1}^2 L_{sh}} \tag{5.2}$$

where ω_{z1} is the transmission-zero frequency (0.85 GHz) in the lower stop-band extracted from the simulation. The capacitance of the *λ/4* open-end stubs can be expressed as [157]:

$$C_p = \frac{\pi}{4\omega_{z2} Z_p} \tag{5.3}$$

where ω_{z2} is the second transmission-zero frequency (9.2 GHz) in the upper stop-band extracted from the simulation and Z_p is the characteristic impedance of the loaded t-line section. The inductance of the open-end stubs can be calculated using Eqn. (5.2). The coupling capacitance C_0 between two conductor sections can be calculated as [112]:

$$C_0 = \frac{1}{2\omega_{01} Z_0} \tag{5.4}$$

where ω_{01} is the first resonance frequency (4.65 GHz) in the pass-band extracted from the simulation and Z_0 is the characteristic impedance of the CPW line. The series inductance of the transmission line can be evaluated from expression for the length of the loaded signal line *l* which is given by [112]:

$$l = \frac{\lambda}{2\pi} \sin^{-1}\left(\frac{\omega_{01} L_s}{Z_0} \right) \tag{5.5}$$

Table 5.2 Extracted equivalent circuit parameters

Capacitance, C_0 (pF)	0.104
Capacitance, C_p (pF)	0.163
Capacitance, C_{sh} (pF)	2.711
Inductance, L_{sh} (nH)	12.93
Inductance, L_p (nH)	1.835
Inductance, L_s (nH)	4.040

The extracted lumped-element parameters are listed in Table 5.2. Figure 5.10 shows a comparison between EM and equivalent circuit simulations. A good agreement is reached that confirms the designed equivalent circuit model.

5.2.3 Effect of Geometrical Parameters

The influence of the geometrical parameters on the filter response has been investigated using EM simulations. Figure 5.11 (a) shows the filter characteristics for fewer values of the gap *c* between two symmetrical sections.

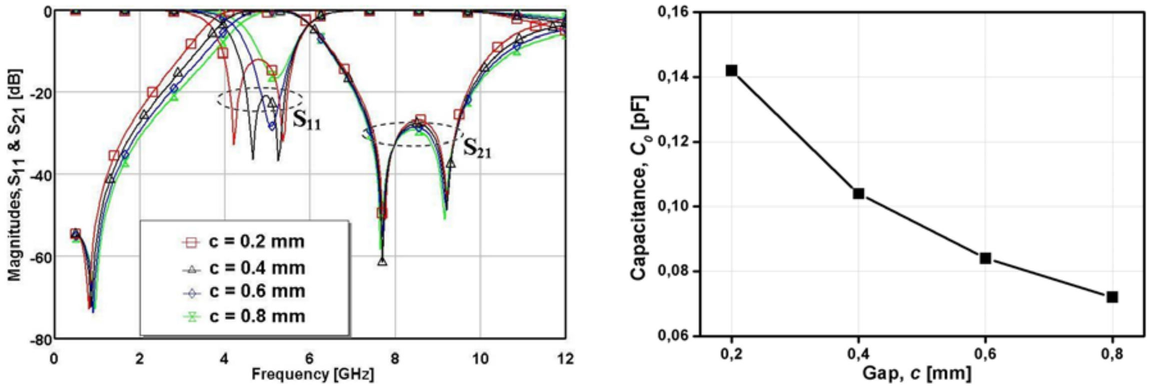

a) b)

Figure 5.11: EM simulations for different values of the gap *c* (a) and equivalent capacitance C_0 versus the gap *c* (b).

As can be seen n the figure, the value of the gap *c* has only an influence on the lower cut-off and on the first resonance pole within the pass-band, while the upper cut-off frequency is not changed. In particular, a smaller value of the gap *c* shifts the resonance pole and the lower cut-off to lower frequencies. Referring to the lumped-element model (see Figure 5.9 (c)), an increase of the gap *c* reduces the capacitance C_0, as shown in Figure 5.11 (b).

Figure 5.12 (a) shows the dependence of the simulated filter response on the section length *a* on the filter response. These simulations reveal that a variation of *a* changes the position of the pass-band while the bandwidth strongly depends on *a*. According to Eqn. (5.1), an increase of the length *a* results in an increase of the value of the shunt inductance L_{sh}. Consequently, the shunt capacitance C_{sh} will also changed. An increase of the distance *a* increases the shunt inductance L_{sh} and C_{sh} and slightly affects the other parameters as shown in Figure 5.12 (b).

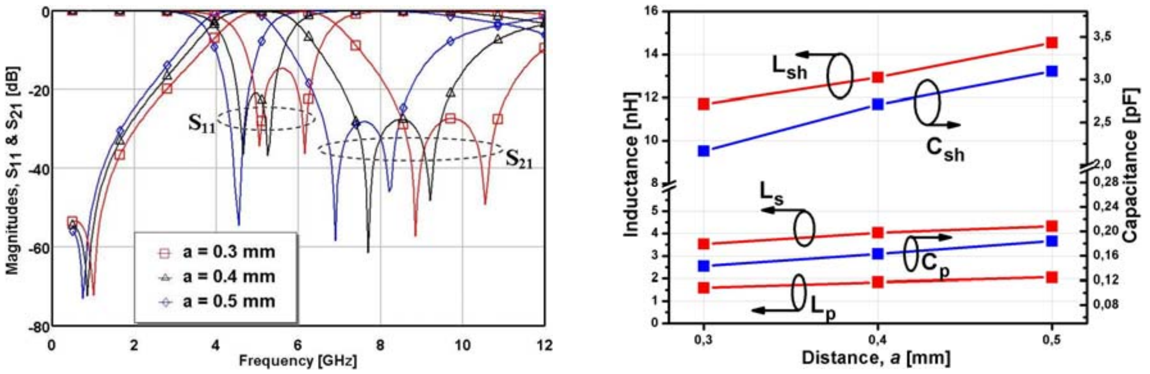

a) b)

Figure 5.12: EM simulations for different values of the length *a* (a), and equivalent capacitance and inductance versus the conductor section *a* (b).

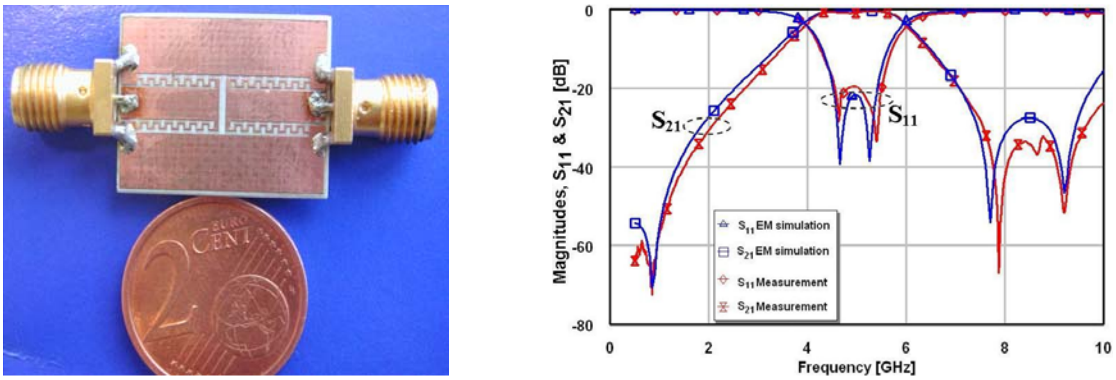

a) b)

Figure 5.13: Photo of the fabricated BPF (a), EM simulation and measurement for BPF (b).

5.2.4 Measurement

The designed bandpass filter was fabricated, Figure 5.13 (a) shows a photo of the fabricated filter, and measured with a vector network analyzer in the frequency range from 0.5 GHz to 10 GHz. The measurements are shown in Figure 5.13 (b). As can be seen, the simulated and measured results are in good agreement. The measured insertion loss in the pass-band is less than 0.7 dB, and the reflection loss is less than -20 dB.

5.2.5 Transformation from Bandpass Filter to Bandstop Filter

The designed coplanar bandpass filter can be easily transformed to a bandstop filter structure. Figure 5.14 (a) shows a schematic drawing of the transformed coplanar bandstop filter. The capacitive coupling through the gap *c* in the bandpass structure has been removed. The meander serpentine-shape shunt-stubs have been transformed to meander serpentine-shape open-stubs, as can be seen in Figure 5.14 (a). The lumped-element model of the coplanar bandstop filter is shown in Figure 5.14 (b). The gap capacitance C_0 was removed from lumped-element model and coupling capacitance C_c was added to the shunt branch of the equivalent circuit model, see Figure 5.14 (b).

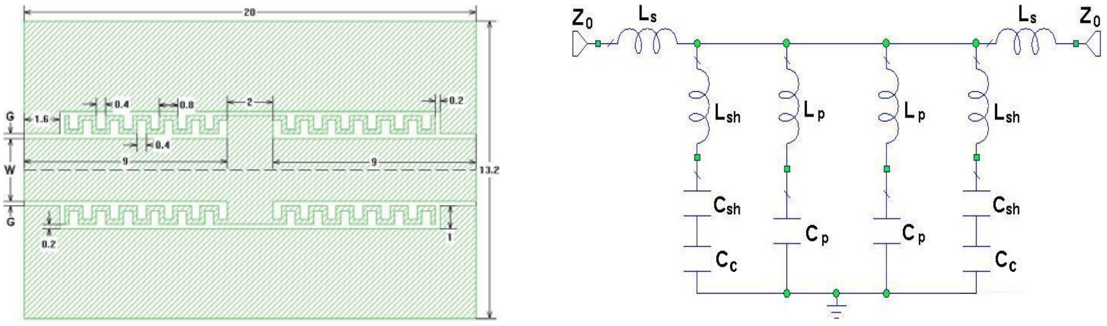

a) b)

Figure 5.14: Schematic diagram of the designed coplanar bandstop filters (a) and equivalent circuit model of the designed BSF (b).

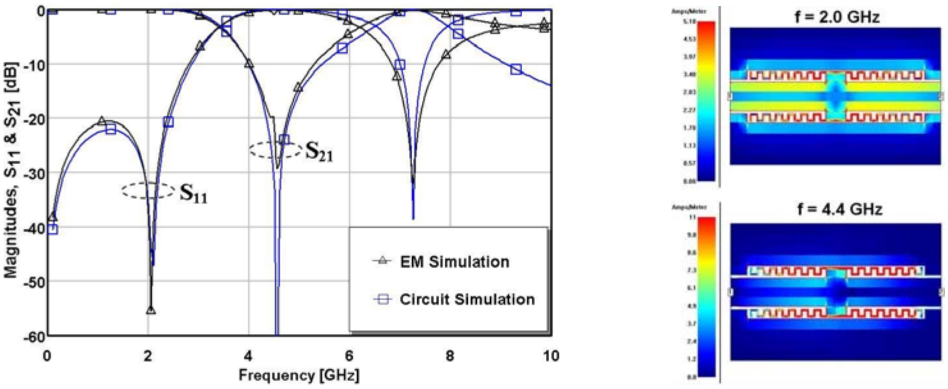

a) b)

Figure 5.15: EM and equivalent circuit simulations for the designed BSF (a) and current density distribution at 2.0 GHz and at 4.4 GHz (b).

The results of electromagnetic and lumped-element model simulations are presented in Figure 5.15 (a). A good agreement between these simulations has been reached. Figure 5.15 (b) shows the current density distribution in the bandstop structure in the stop-band at 4.4 GHz and in the pass-band at 2.0 GHz. It can be seen that at the pass-band the two ports are well coupled, while in the stop-band almost no RF power passes through the filter.

5.3 2-D Quasi-Fractal Periodic Defected Ground Structure for Coplanar Waveguide

This section is dedicated to a 2-D quasi-fractal periodic dumbbell DGS. A conventional rectangular dumbbell DGS has been modified in order to improve the RF performance by using a fractal geometry approach. The quasi-fractal DGS slot is added as a unit-cell in a systematic way in both horizontal and vertical directions to construct the 2-D periodic DGS as proposed in [150]. This method allows to use the structure area more effectively and to shift the transmission zero to lower frequencies.

5.3.1 Structure Design Methodology

The quasi-fractal periodic DGS structure in CPW environment is based on the standard dumbbell structure (Figure 5.16 (a)). The quasi-fractal DGS cell is designed by adding eight open-end rectangular stubs within the (Figure 5.16 (c)). The cells are symmetrically added along the axes (A-A). Thus, the two-cell structure is realised by adding the next cell above the first one in vertical direction, see Figure 5.17 (a). The three cells are located in the horizontal direction to the left and to the right of the first cell. A larger number of cells is realised in the same way. The schematic diagrams of 2, 3, 4, 5 cells are shown in Figure 5.17.

5.3.2 Electromagnetic Simulation and Circuit Modeling

The unit dumbbell DGS has been designed for a 50-Ω coplanar waveguide line where the strip and slot widths are 2.8 mm and 0.2 mm, respectively. The geometrical parameters of the rectangular unit-cell have been optimized to get a resonance frequency close to 11.5 GHz. This corresponds to unit-cell dimensions of $a \times b = 2.0 \times 1.8 \text{ mm}^2$. The cells are symmetrically etched in the ground planes on both sides of the center conductor at distance $a/2$ and are connected to the CPW slots by a gap with width $t = 0.2$ mm. The quasi-fractal cell with the same geometrical parameters exhibits a resonance frequency at 10 GHz. The optimized dimensions of the open-end stub within the quasi-fractal DGS unit-cell are 0.9×0.2 mm^2.

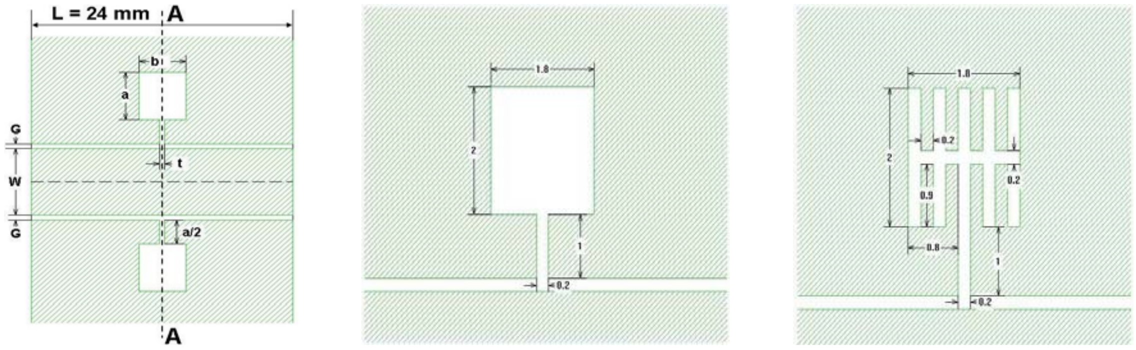

a) b) c)

Figure 5.16: Schematic diagram of the standard dumbbell structure (a), rectangular DGS cell (b) and quasi-fractal cell (c).

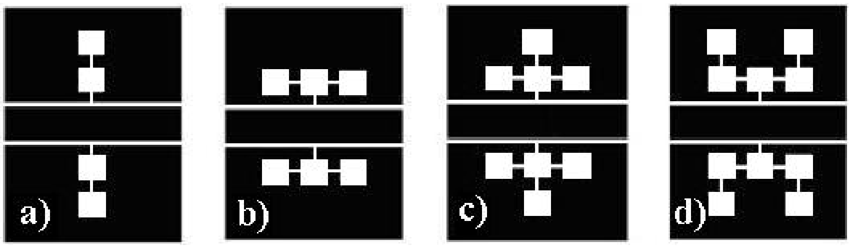

Figure 5.17: The designed periodic DGS: 2-Cells (a), 3-Cells (b), 4-Cells (c), and 5-Cells (d).

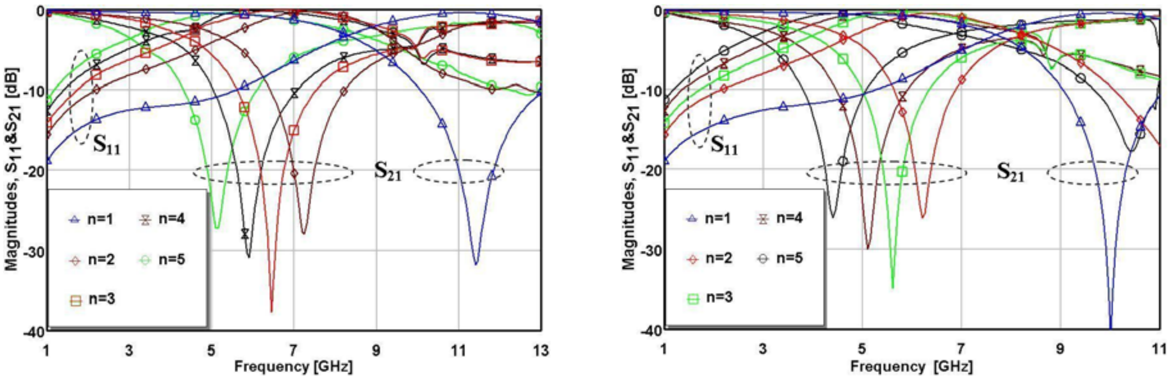

a) b)

Figure 5.18: Frequency response for DGS with different number of cells n: rectangular cells (a) and quasi-fractal DGS cells (b).

Two, three, and up to five-cells are arranged as outlined above and shown in Figure 5.17. The frequency responses of the five rectangular and five quasi-fractal cells can be seen in Figure 5.18 (a) and (b), respectively. The transmission coefficient S_{21} shows a minimum at a frequency determined by the structure geometry. Its value increases as the number of cells decreases. For one cell (n = 1) the resonance frequencies are 11.4 GHz and 10.0 GHz, while for five cells, these frequencies are shifted to 5.15 GHz and 4.4 GHz for the rectangular and the quasi-fractal DGS cell, respectively. The stop-band rejection for all structures is higher than -20 dB.

The lumped-element equivalent circuit model (in Figure 5.19 (a)) has been used to describe the behaviour of the periodic DGS. It consists of parallelly connected *R*, *L* and *C* elements representing the DGS region and two sections of transmission line which are connected in series at both sides. The characteristic impedance and the effective dielectric constant of the transmission line sections determined by the EM simulator are 50.6 Ω and 1.935, respectively. EM and equivalent circuit model simulations for the rectangular and quasi-fractal DGS are can be seen in Figure 5.19 (b). This equivalent circuit model is valid for any number of repeated cells, only the values of the circuit parameters have to be varied.

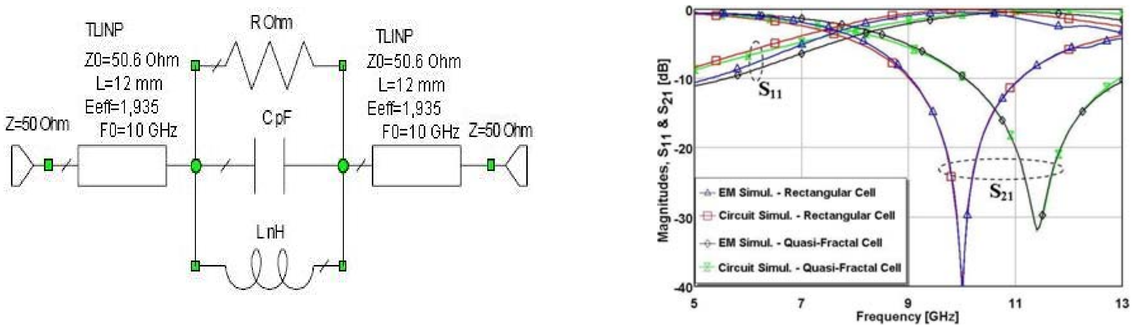

a) b)

Figure 5.19: Equivalent circuit model of the DGS (a) and EM and circuit simulations for both DGS cells (b).

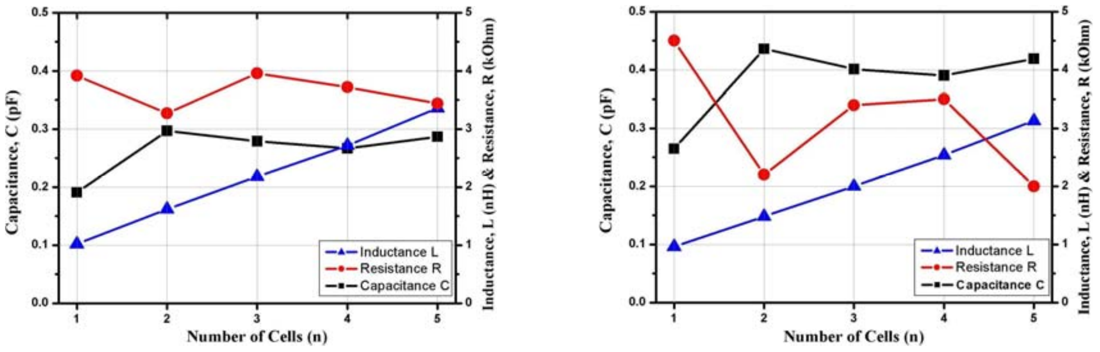

a) b)

Figure 5.20: Equivalent capacitance, inductance, and resistance versus the number of repeated cells for the 2-D periodic DGS structure: rectangular cells (a), quasi-fractal cells (b).

Variations of the R, L and C values as a function of the cell number of the rectangular and quasi-fractal structures are depicted in Figure 5.20 (a) and Figure 5.20 (b), respectively. It can be seen that the equivalent capacitance is approximately constant independent of the number of cells. For the quasi-fractal slots, however, its value is more than 30 % higher. The equivalent inductance linearly increases with the number of cells and is almost the same for both DGS cells.

The results can be interpreted with respect to the structure topology as follows: The current path increases as the number of cells is increased resulting in an increase of the inductance L. Due to the constant area of all cells the parallel inductance changes linearly with a number of cells. The capacitance is mainly determined by the gap capacitance of the first cell, which remains the same for all structures. For the quasi-fractal cell the gap is extended inside the cell by the open-end stubs. Therefore, the equivalent capacitance of the quasi-fractal DGS is higher than for the rectangular one, thus, the resonant frequency is shifted to lower frequencies. The resistance changes due to radiation, conductor and dielectric losses in the DGS.

5.3.3 Experimental Verifications

The quasi-fractal DGS devices with the geometric dimensions investigated in the previous section were fabricated. The photos of the fabricated quasi-fractal periodic DGS with two, three, four and five cells are shown in Figure 5.21 (a). The enlarged view of the three cells geometry is illustrated in Figure 5.21 (b). The measurements were carried out at frequencies from 2.0 GHz to 8.0 GHz. The measured S-parameters together with EM and equivalent circuit model simulations are shown in Figures 5.21 (c-g). A good agreement between measurements and simulations could be obtained.

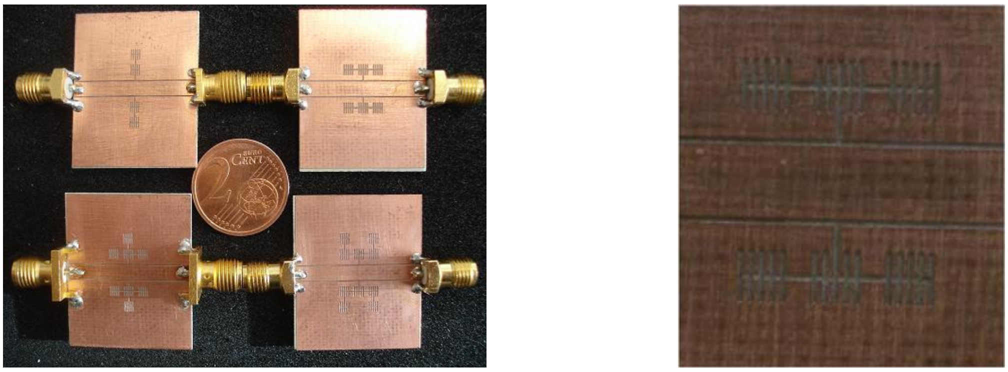

a) b)

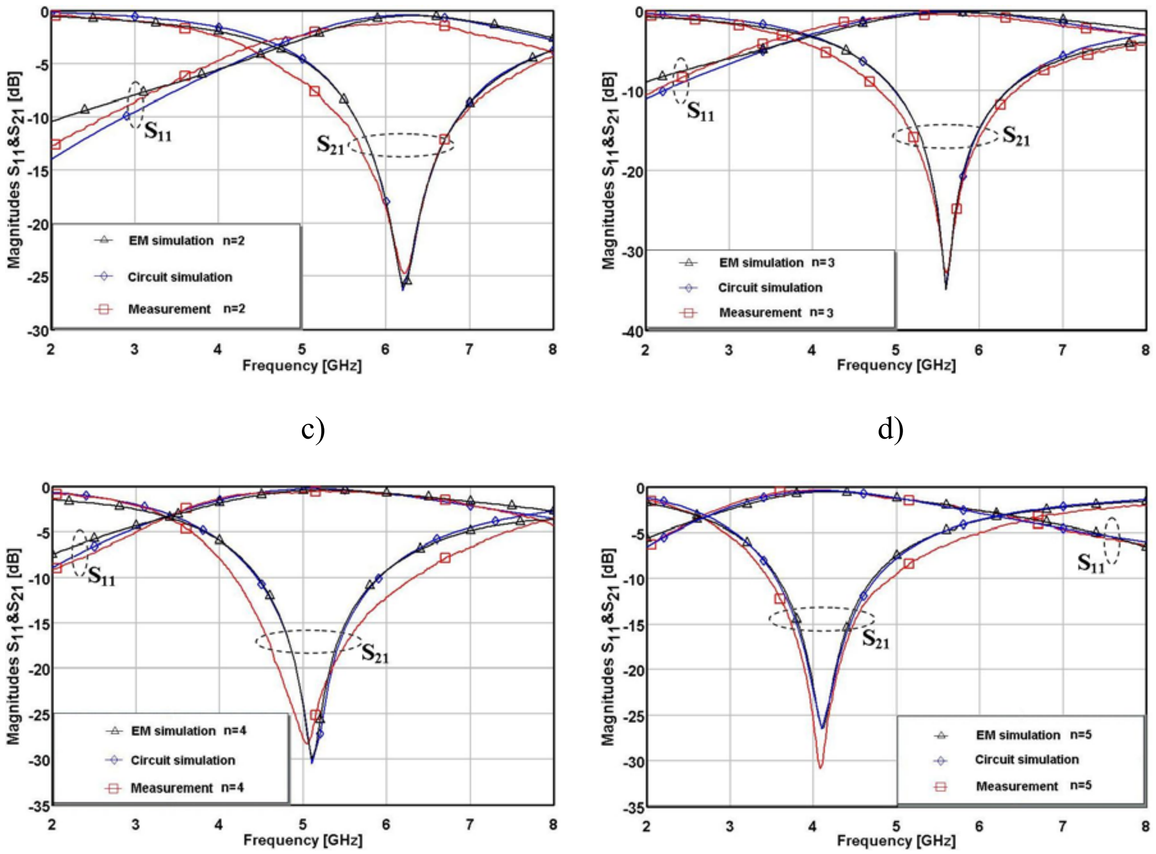

c) d)

e) g)

Figure 5.21: Photo of the fabricated quasi-fractal periodic DGS with 2, 3, 4 and 5 cells (a), scaled fragment of the quasi-fractal 3-cells DGS (b). Measurements, EM and equivalent circuit simulated results: 2 cells (c), 3 cells (d), 4 cells (e) and 5 cells (g).

5.4 Coplanar Low-Pass Filter Using Cascaded Arrowhead DGS

A cascaded DGS low-pass filter in CPW environment is presented in this section. The filter structure is designed by using triangular arrowhead DGS slots symmetrically etched in the ground metallization on both sides of the center conductor. The one-cell arrowhead DGS slot was designed and optimized using EM simulations as well as a lumped-element equivalent circuit model.

5.4.1 One-Cell Triangular Arrowhead DGS Slot

A scheme of the one-cell triangular arrowhead DGS slot is shown in Figure 5.22 (a). This structure is implemented in CPW environment with a characteristic impedance of 50 Ω; this corresponds to strip and slot widths of 2.8 mm and 0.2 mm, respectively. The dimensions of

DGS are: a = 5.5 mm, g = 0.5 mm and l = 2.0 mm. The structure resonates at 8.1 GHz. The equivalent circuit model of the one-cell DGS slot is depicted in Figure 5.22 (b).

The resonance frequency ω_0 of the parallel resonant circuit elements is given by:

$$\omega_0 = \frac{1}{\sqrt{L_1 C_1}} \tag{5.6}$$

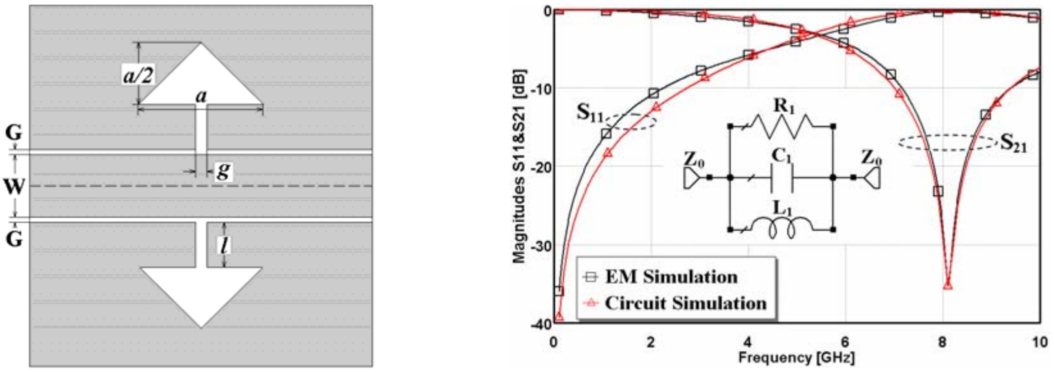

a) b)

Figure 5.22: Schematic drawing of the coplanar triangular arrowhead DGS slot (a) and its EM and equivalent circuit simulated frequency responses (b).

The equivalent impedance is given by:

$$Z_{DGS} = \frac{1}{1/R_1 + 1/j\omega L_1 + j\omega C_1} \tag{5.7}$$

The transmission coefficient S_{21} is easily shown to be given by [157]:

$$S_{21} = \frac{2Z_0}{2Z_0 + Z_{DGS}} = \frac{2Z_0}{2Z_0 + \dfrac{1}{1/R_1 + 1/j\omega L_1 + j\omega C_1}} \tag{5.8}$$

The 3 dB cut-off frequency location ω_c is defined through [157]:

$$|S_{21}| = \frac{2Z_0}{\sqrt{4Z_0^2 + \left(\dfrac{\omega_c / C_1}{\omega_0^2 - \omega_c^2}\right)^2}} = \frac{1}{\sqrt{2}}, \quad \text{assuming that } R_1 >> Z_0 \tag{5.9}$$

Rearranging (5.9), the capacitance of the parallel RLC resonator is given by [83]:

$$C_1 = \frac{\omega_c}{2Z_0(\omega_0^2 - \omega_c^2)} \tag{5.10}$$

Substituting the capacitance value back into (5.6), the inductance value L_1 can be determined.

The parallel resistance R_1 of the DGS can be best fitted at the resonance frequency where the structure equivalent impedance is $Z_s=R_1$, S_{21} is then given by [83]:

$$S_{21}|_{\omega_0} = \left|\frac{2Z_0}{2Z_0+Z_s}\right| = \frac{2Z_0}{2Z_0+R_1} \qquad \Longrightarrow \qquad R_1 = 2Z_0\frac{1-S_{21}|_{\omega_0}}{S_{21}|_{\omega_0}} \tag{5.11}$$

The 3 dB cut-off frequency ω_c and the resonance frequency ω_0 are extracted from an EM simulation. To validate the circuit model, the one-cell triangular arrowhead DGS has been simulated using the EM MoM simulator. The frequency responses of the one-cell DGS slot obtained by using EM and equivalent circuit model simulations are presented in Figure 5.22 (b). The EM simulation results show the transmission zero at 8.1 GHz with more than -30 dB rejection, a cut-off frequency of 5.5 GHz and a S_{21} at ω_0 of 0.15 dB. The extracted R_1, L_1, and C_1 values are 5.77 kΩ, 1.72 nH, and 0.224 pF, respectively. The resistance R_1 is much higher than the characteristic impedance of the CPW line and represents the radiation loss in the structure. Both, the EM and the equivalent circuit model simulations are in good agreement as can be seen in Figure 5.22 (b).

Figures 5.23 (a) and (b) show the frequency responses for the one-cell triangular arrowhead DGS slot for different values of the triangular area and different gap widths *g*. An increase of the triangular area shifts cut-off and transmission-zero to lower frequencies, see Figure 5.32 (a). A change of the gap width *g* shifts the resonance frequency and slightly affects the cut-off frequency (Figure 5.32 (b)). The triangle area represents a magnetic loading and is responsible for the parallel inductance in the equivalent circuit model, while the gap *g* represents an electric loading and is responsible for the parallel capacitance.

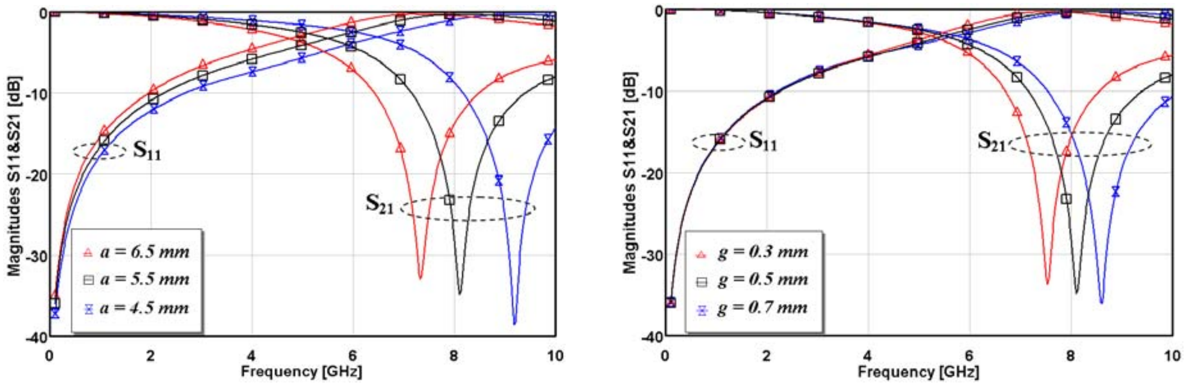

a) b)

Figure 5.23: Simulated frequency response of the triangular arrowhead DGS slot for different values of the parameter *a* (a) and the gap width *g* (b).

5.4.2 Design of Cascaded Arrowhead DGS Low-Pass Filter

Figure 5.24 (a) shows the schematic diagram of coplanar cascaded DGS low-pass filter. It consists of three pairs of arrowhead triangular DGS slots. A low impedance conductor section is added to the center line in order to increase the capacitive loading of the CPW structure. This section is periodically loaded by parallel *LC* resonators modeled by DGS. In order to reduce the undesired coupling between the DGS resonators the area of the DGS slots at the filter ports is smaller than the area of the DGS in the middle as is shown in Fig. 5.24 (a).

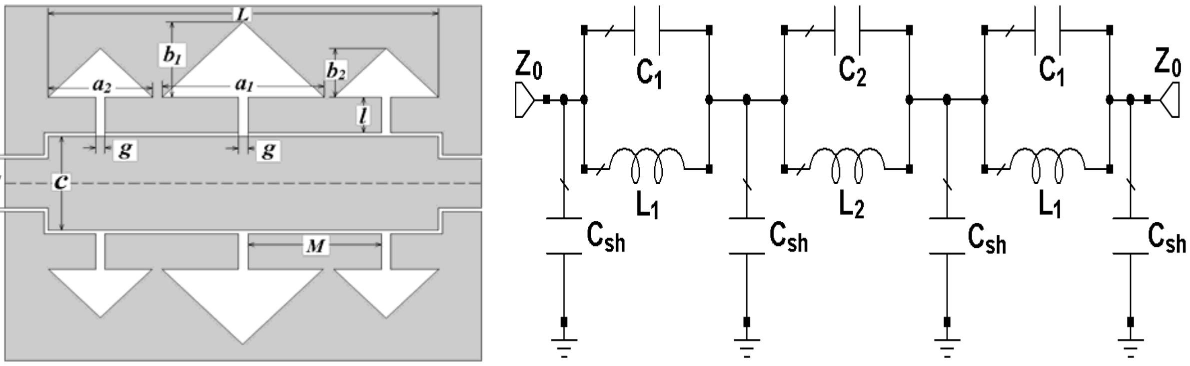

a) b)

Figure 5.24: Schematic diagram of the cascaded coplanar triangular arrowhead DGS LPF (a) and its lumped-element equivalent circuit model (b).

The equivalent circuit model of the capacitively coupled CPW DGS LPF is shown in Figure 5.24 (b). Parallel L_iC_i resonators represent the DGS slots per-section, and C_{sh} are the coupling capacitances. Due to the structure symmetry the smaller DGS slots are modeled by identical values of the elements L_1C_1.

The equivalent impedance of the DGS can be determined using Eqn. 5.7 while the characteristic impedance of the transmission line between adjacent DGS resonators at low frequency is given by [157]:

$$Z_T = \sqrt{\frac{L_i}{C_{sh}}} \tag{5.12}$$

where L_i is the inductance of the unloaded line. The filter designed according to these equations provides a cut-off frequency of 4.4 GHz. Since the stop-band width of the filter increases as well as the ratio Z_{DGS}/Z_T, the characteristic impedance of the unloaded line has been set equal to $Z_T = 35\ \Omega$. Using these equations the parameters of the equivalent circuit model are inferred. The lateral dimensions of the low impedance section, as well as the distance between adjacent resonators, can be obtained using the transmission line simulator. Full-wave EM simulations with parameter variation have been carried out to fit the dimensions of the CPW to those required for the nominal value of the capacitance C_{sh}. The results of these simulations are depicted in Figure 5.25 (a). The result clearly illustrates that the filer response in the pass-band strongly depends on the electric coupling between the center line and the ground planes. In the equivalent circuit model this coupling is modeled by the shunt capacitances C_{sh} which decreases as the line width decreases. The optimised center conductor line and gap width are c = 7.6 mm and G = 0.15 mm, respectively.

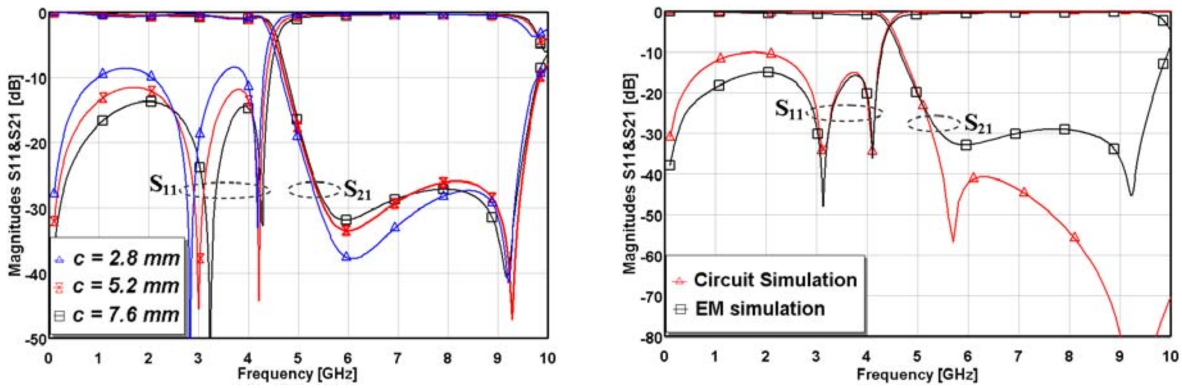

a) b)

Figure 5.25: Simulated frequency response for the different values of the line width c (a) and EM and equivalent circuit model simulations of the cascaded arrowhead DGS LPF (b).

The dimensions of the triangular arrowhead DGS slots are: a_1 = 6.0 mm, b_1 = 5.3 mm, a_2 = 9.6 mm, b_2 = 1.8 mm, c = 7.6 mm, g = 0.2 mm, l = 1.0 mm, M = 8.7 mm and L = 27.4 mm.

A comparison between EM and circuit simulation is shown in Figure 5.25 (b). A good agreement is achieved that validates the designed lumped-element equivalent circuit model. The simulated return loss in the stop- and pass-band is better than -0.4 dB and -15 dB, respectively. The 3 dB cut-off frequency is at 4.4 GHz and the stop-band rejection is higher than - 28 dB.

5.4.3 Experimental Verification

The designed cascaded coplanar arrowhead DGS low-pass filter was optimized by using full-wave EM MoM simulators and was fabricated. A photo of this filter structure is shown in Figure 5.26 (a). The total size of the LPF is 28.0×25 mm^2. The fabricated filter was measured using a vector network analyzer in the frequency range from 0.5 GHz to 12 GHz. The measured and simulated frequency responses are presented in Figure 5.26 (b). Both results agree rather well. The slight differences between both may be due to tolerances in the fabrication process. The measured insertion and return losses in the pass-band are better than 0.7 dB and -12 dB, respectively. The designed LPF provides a -20 dB stop-band width of 4.7 GHz within the frequency range from 5.7 GHz up to 10.4 GHz. A good cut-off transition is reached as can be seen in Figure 5.26 (b).

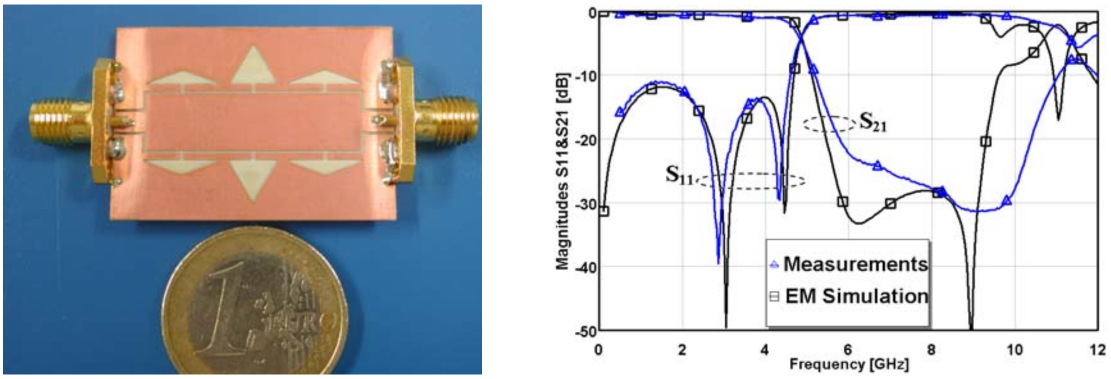

a) b)

Figure 5.26: Photo of the fabricated coplanar cascaded triangular arrowhead DGS LPF (a) and its measured and simulated frequency responses (b).

5.5 Design of Compact Coplanar UWB DGS Low-Pass Filter

In this section, the design of a new compact ultra wideband (UWB) DGS low-pass filter is pesented. The designed structure is based on coplanar waveguide (CPW) lines and $\lambda/4$ resonators. The filter provides three transmission zeros within the stop-band and offers a bandwidth of 8.3 GHz, namely from 3.1 GHz to 11.4 GHz. The stop-band rejection is higher than -20 dB. The filter area is as low as 17.6×23.4 mm^2. The cascade method was used to increase the stop-band width and to improve the pass-band characteristics. The cascaded LPF provides a stop-band width of more than 20 GHz, namely from 3.7 GHz up to more than 22.0 GHz with a rejection higher than -15 dB.

5.5.1 Low-Pass DGS Filter Topology

Figure 5.27 (a) shows a scheme of the designed low-pass DGS filter structure. It has been constructed by combining $\lambda/4$ open-ended stub resonators with DGS resonators. Two DGS slots are etched in the ground plane and located on both sides of the center conductor. The designed DGS slot consists of two square heads and a connecting slot with a gap of 1.0 mm. The CPW lines used for this filter have been designed for a characteristic impedance of 50 Ω. This impedance corresponds to a strip width of W = 2.8 mm and to a slot width of G = 0.2 mm, see Figure 5.27 (a). The geometrical parameters of the filter structure are: a = 6.3 mm and l = 7.7 mm. Figure 5.27 (b) shows the insertion and return losses of the simulated structure with the above dimensions.

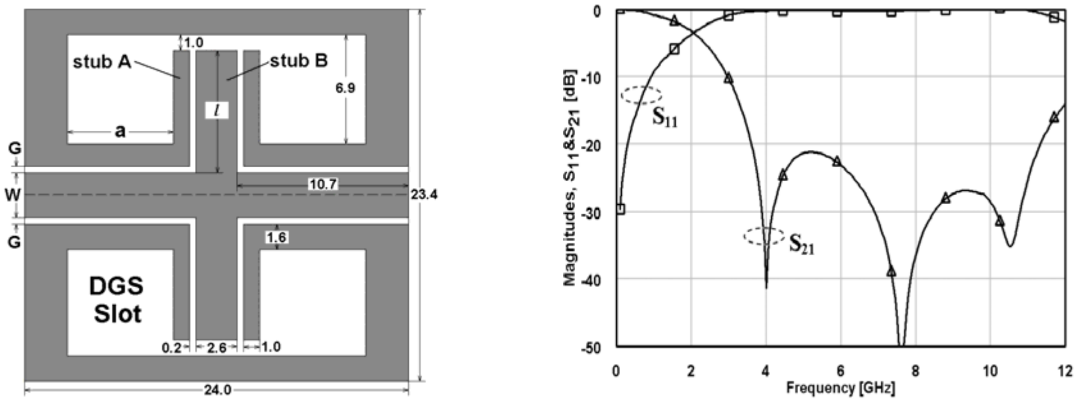

a) b)

Figure 5.27: Scheme of the designed coplanar low-pass DGS filter (a) and the EM simulation result for the designed low-pass filter (b).

The slot-head areas basically control the inductance, whereas the width of the connecting rectangular slot controls the capacitance. The series inductance has been increased by adding the open-end sections of the transmission line between the two DGS heads in the ground plane (Figure 5.27 (a)).

5.5.2 EM and Equivalent Circuit Simulations

Figure 5.28 (a) shows the lumped-element equivalent circuit model for the designed low-pass DGS filter. Due to the stubs A, (Figure 5.27 (a)), the DGS slots operate as a shunted series resonator at the corresponding *λ/4*. These stubs resonate when their length is equal to *λ/4* that is responsible for the transmission zero occurring at 4.0 GHz. In order to verify that, the physical length of the stub A is compared to the effective wavelength at the first transmission-zero frequency, which is given by [118]:

$$\lambda_g = \frac{c}{\sqrt{\varepsilon_{eff}}\, f_z}, \tag{5.13}$$

where c is the speed of light in free space, ε_{eff} is the effective dielectric constant, and f_z is the transmission-zero frequency.

The effective dielectric constant ε_{eff} and the transmission-zero frequency have been extracted from the electromagnetic simulation. The theoretically calculated effective wavelength λ_g at the first transmission-zero frequency is 49.2 mm. The physical length of the stub A is approximately equal to $\lambda_g/4$.

Similarly the stubs B which are connected to the central transmission line operate as shunted series resonator at the corresponding $\lambda/4$, which is responsible for the transmission zero that occurs at 7.6 GHz.

In order to understand the reason behind the transmission zero occurring at 10.55 GHz, the current density distribution in the filter metallization has been calculated using the EM MoM simulator. Figure 5.28 (b) shows this distribution at the third transmission-zero frequency of 10.55 GHz.

From Figure 5.28 (b) it can be clearly seen that there is a coupling between the open-end stubs and the stubs within the DGS slots, since the current density has maxima and minima at the stub metallization. Such a coupling is a mixed one, i.e. an inductive and a capacitive coupling together. Therefore, a parallel *LC* resonator can represent this coupling.

The equivalent circuit of the designed low-pass structure has two shunted series resonators coupled to each other by a mixed coupling element (parallel resonator). As shown in Figure 5.28 (a), the first resonator C_1L_1 represents the stubs inside the DGS slots, while C_2L_2 represents the open-end stubs connected to the center line. The parallel resonator C_cL_c represents the mixed coupling between these stubs.

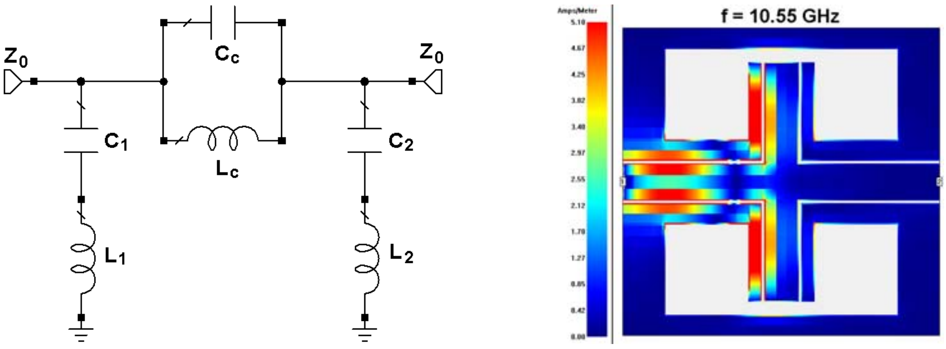

a) b)

Figure 5.28: Equivalent circuit model of the designed coplanar low-pass DGS filter (a) and simulated current density distribution at the third transmission zero at 10.55 GHz (b).

The equivalent circuit extraction method has been used to extract the values of the circuit parameters. The resonance frequency ω_{0i} given in term of the resonant circuit elements can be determined by Eqn. (5.6).

The shunted series resonator L_1C_1, corresponded to the first transmission zero at 4.0 GHz, has an impedance given by:

$$Z_1 = j\omega L_1 + \frac{1}{j\omega C_1} \tag{5.14}$$

The transmission coefficient S_{21} is easily shown to be given by [157]:

$$S_{21} = \frac{2Z_0}{2Z_0 + Z_1} = \frac{2Z_0}{2Z_0 + j\omega L_1 + \frac{1}{j\omega C_1}} \tag{5.15}$$

The 3 dB cut-off frequency ω_c is defined through [157]:

$$|S_{21}| = \frac{2Z_0}{\sqrt{4Z_0^2 + \left(\frac{\omega_c^2 - \omega_0^2}{\omega_0^2 \omega_c C_1}\right)^2}} = \frac{1}{\sqrt{2}} \tag{5.16}$$

Rearranging (5.16), the capacitance of the equivalent circuit model is:

$$C_1 = \frac{(\omega_c^2 - \omega_0^2)}{2\sqrt{2}Z_0(\omega_0^2\omega_c)} \tag{5.17}$$

Substituting back in the expression for the resonance frequency Eqn. (5.6), the inductance value L_1 can be determined as:

$$L_1 = \frac{2\sqrt{2}Z_0\omega_c}{(\omega_c^2 - \omega_0^2)} \tag{5.18}$$

A similar calculation can be used to extract the element parameters for the shunted series resonator L_2C_2 which is responsible for the transmission zero at 7.6 GHz.

At high frequencies the equivalent circuit is represented by the parallel coupled resonator L_cC_c while the series resonators are in the rejection state. The equivalent capacitance and inductance of the parallel resonator can be determined as in section 5.4.1 of this chapter.

The extracted circuit parameters are: L_1 = 3.95 nH; C_1 = 0.40 pF; L_2 = 0.87 nH; C_2 = 0.56 pF; and L_c = 1.45 nH; C_c = 0.15 pF. Equivalent circuit simulations have been carried out and the lumped-element parameters have been adjusted to meet the EM response. Both EM and equivalent circuit simulation results for the designed low-pass filter are in good agreement as can be seen in Figure 5.29.

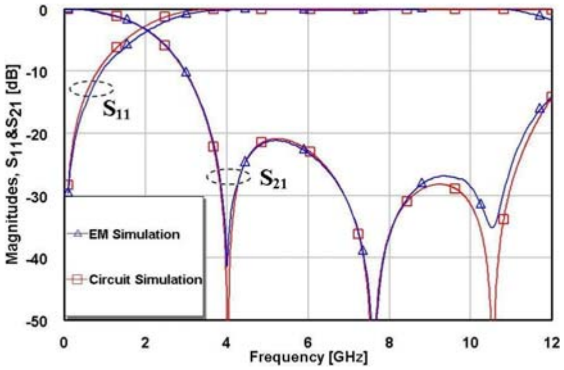

Figure 5.29: EM and equivalent circuit simulations for the designed coplanar DGS LPF.

5.5.3 Control of the Low-Pass Filter Characteristics

Some parameters are influencing the transmission-zero frequency positions such as the geometrical parameters *a* and *l,* (see Figure 5.27 (a)). Figure 5.30 (a) shows the filter response for three values the length *l* of the open-end sections. As can be seen, an increase of the length of the stub shifts the second and third transmission zeros to lower frequencies, and vice versa. A change of the length of these stubs should only affect the second transmission zero. Due to the narrow gap between the stubs, however, any change of the dimensions of each affects the coupling between them. Therefore, the third transmission zero is also shifted to a lower frequency band.

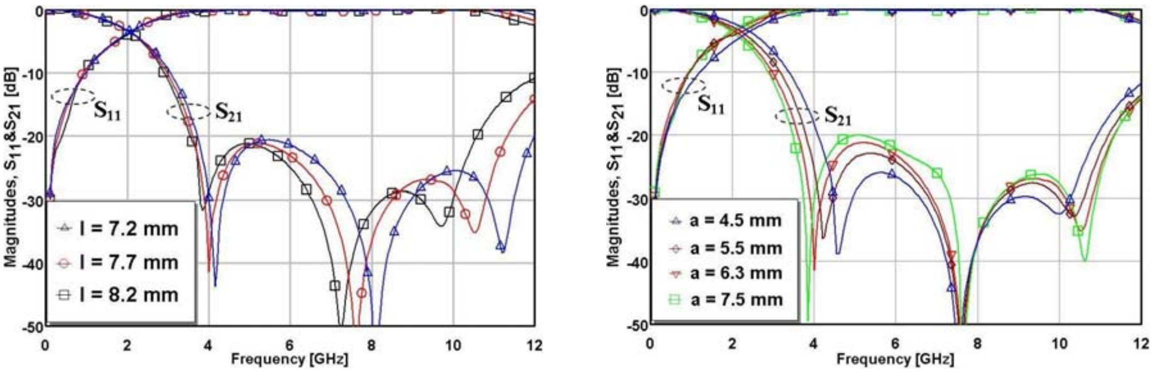

a) b)

Figure 5.30: EM simulations for the different values of the geometrical parameters: for the length of the open-stubs *l* (a) and for the distance *a* (b).

By changing the value *a* (see Figure 5.27 (a)) the length of the stubs that are responsible for the first transmission zero is changing. Therefore, by increasing the distance *a* the first transmission zero is shifted to a lower frequency band while the other two transmission zeros remain at the same position. Figure 5.30 (b) shows the filter response with different values of the distance *a*.

5.5.4 Experimental Results

The designed filter was optimized and then fabricated. The dimensions of the fabricated and investigated filter are a = 7 mm, l = 7.7 mm, see Figure 5.27 (a). The filter has a 3 dB cut-off frequency of 1.5 GHz, and three transmission zeros located at 4.0 GHz, 7.6 GHz, and 10.55 GHz. The highest insertion loss in the pass-band is better than 0.8 dB, and the highest group delay is better that 0.21 ns. Figure 5.31 (a) shows a photo of the fabricated filter. The measurements are depicted in Figure 5.31 (b). A very good agreement between the simulated and measured result could be achieved with the exception of the third transmission-zero position which is shifted to a lower frequency. This is most probably due to the thickness of the metallization which has not been taken into account in the simulation.

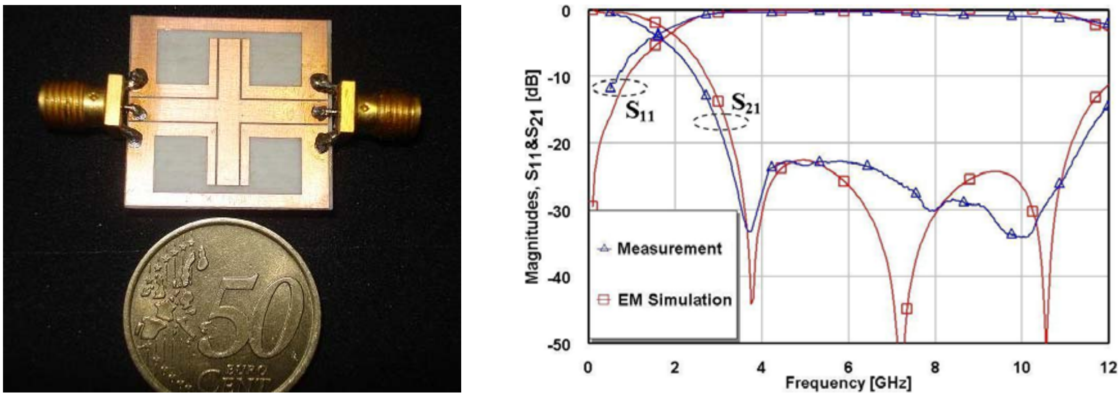

a) b)

Figure 5.31: Photo of the fabricated coplanar low-pass UWB DGS filter (a) and its EM simulated and measured results (b).

5.5.5 Cascaded UWB Low-Pass Filter

In order to increase the stop-band width and to improve the pass-band performance the cascade approach has been implemented. Figure 5.32 depicts a schematic drawing of the cascaded UWB DGS LPF. To meet the requirement of compactness the dimensions of the structure were changed as shown in the figure. The simulated frequency response for the designed UWB DGS LPF is shown in Figure 5.33. It can be seen that the transmission pole appears in the lower pass-band. Therefore, the transition characteristic is improved. It can be understood by increased total capacitances of the open-stubs resonators. The highest reflection coefficient S_{11} in the pass-band is better than 0.5 dB. The optimized dimensions with regard to the performed simulations are: $a = 3.6$ mm, $l = 5.0$ mm and $g = 2.6$ mm. The total area of the cascaded structure is 23.4×24.0 mm^2.

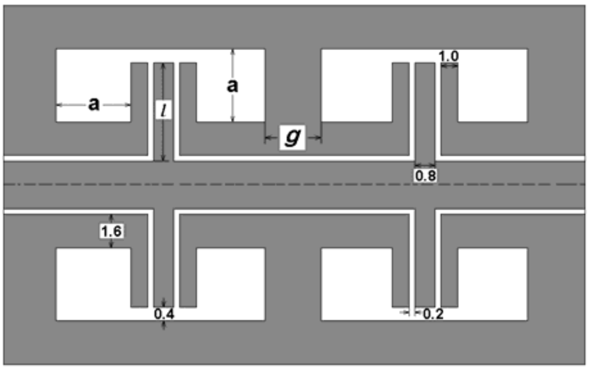

Figure 5.32: Schematic drawing of the designed coplanar cascaded UWB DGS LPF.

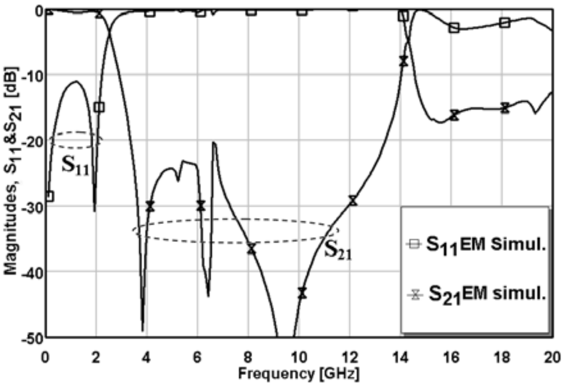

Figure 5.33: EM simulation results for the designed cascaded UWB DGS LPF.

The lumped-elements equivalent circuit model of the cascaded UWB DGS LPF is depicted in Figure 5.34. Both resonator structures are coupled with each other through an inductance L_0. Thereby, the coupling between open-stubs and DGS slots is presented by a Π-junction of series connected L_2C_2 and parallel inductance L_0, as can be seen in Figure 5.34.

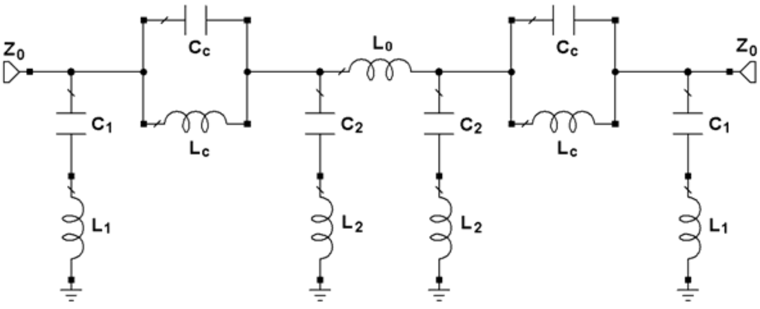

Figure 5.34: Equivalent circuit model of the cascaded CPW UWB DGS LPF.

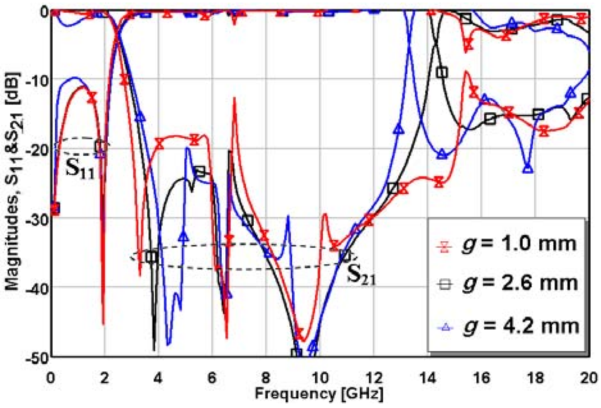

Figure 5.35: EM simulations for the different values of the distance *g*.

Figure 5.35 shows the simulated frequency responses of the cascaded UWB DGS low-pass filter for different values of the distance *g*. As can be seen, increasing this distance decreases the electromagnetic coupling between two DGS slots leading to a shift of the first transmission zero to higher frequencies. But if the distance *g* exceeds certain limiting values the transmission characteristics in the pass-band become worse. The optimum distance is 2.6 mm.

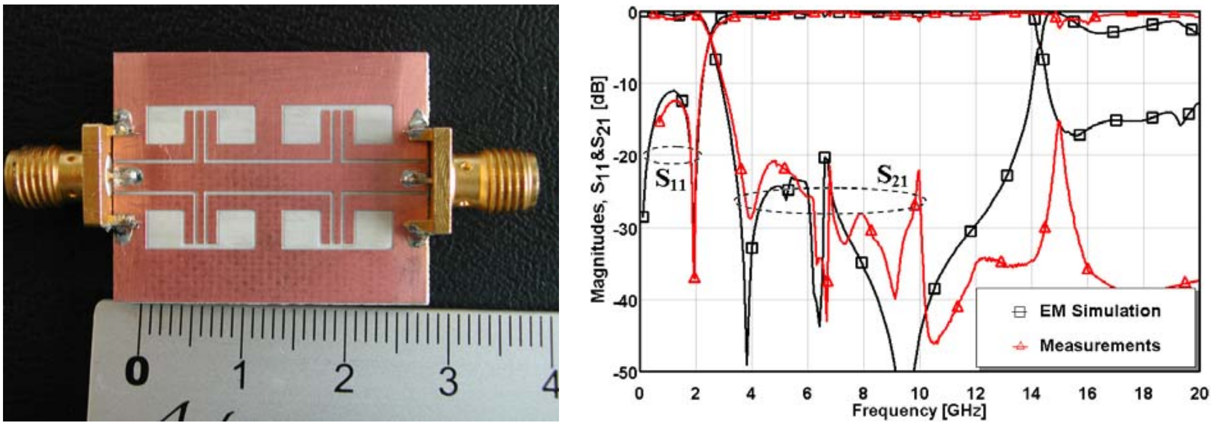

a) b)

Figure 5.36: Photo of the fabricated coplanar cascaded UWB DGS LPF (a) and (b) its simulated and measured frequency responses.

The designed cascaded CPW UWB DGS PPF was fabricated on the same substrate as the filter described above. The photo of it is shown in Figure 5.36 (a), the frequency response in Figure 5.36 (b). A very good agreement between the simulated and the measured results is achieved. The measured frequency response is superior to the simulated one. Namely, the stop-band width is increased up to 22.0 GHz with a rejection of more than -15 dB. This may be due to the thickness of the metallization which has not been taken into account in the simulation as in the case of one-cell UWB DGS LPF. The highest measured reflection coefficient in the pass-band is better than 0.9 dB. The highest measured insertion loss in the stop-band ranging from 3.5 GHz to 15.0 GHz is better than 0.7 dB.

5.6 Summary

In this chapter several designs of RF filters constructed in CPW environment have been presented. Different approaches were used to realize the filter structures. Two bandpass filters were designed using the capacitively end-coupled method and the inductively shunt-coupled line approach. The first BPF was realized by using *λ/4* open-end stub resonators for the pass-band of 1.7-5.2 GHz. The second BPF was designed for the pass-band of 3.9-6.0 GHz. using meander serpentine-shape *λ/2* shunt-stubs that reduced the filter size and improved its RF performance. Additionally, the designed BPF was transformed to bandstop structure.

The performance of the conventional dumbbell DGS was been improved by using fractal geometry. A 2-D quasi-fractal DGS structure was periodically repeated in order to control the resonance frequency. The designed quasi-fractal DGS had a capacitance value more than 30 % higher than the capacitance of the standard rectangular DGS. It allowed to shift the resonance pole to lower frequencies.

A coplanar capacitively coupled DGS low-pass filter was designed and optimized. The filter was constructed on a CPW line, which was periodically loaded with triangular arrowhead DGS slots realizing slow-wave effect. One-cell arrowhead triangular DGS slot was investigated using an equivalent circuit extraction method in addition to EM simulations. The measured stop-band width was close to 5.0 GHz with a stop-band rejection higher than -20 dB.

A new compact high performance coplanar UWB low-pass DGS filter with improved stop-band was introduced in the last section of this chapter. The structure was based on *λ/4* open-end stub resonators combined with novel shape DGS. The designed filter showed wide and deep stop-band characteristics. The designed one-cell DGS LPF provided three transmission zeros within the stop-band and a bandwidth of 8.3 GHz, ranging from 3.1 GHz to 11.4 GHz. The stop-band width and the pass-band characteristic were improved further by using the cascade method. The bandwidth of the cascaded DGS LPF was more than 20 GHz with a stop-band rejection higher than -15 dB.

All filter structures were fabricated and measured. A very good agreement between the electromagnetic simulated results, the lumped-element equivalent circuit model simulations and the measured results could be obtained.

Chapter 6

A Compact MEMS-Switch Controlled Tunable Quasi-DGS Coplanar Bandpass Filter

This chapter introduces the design of a new compact microwave RF MEMS-Switch controlled, tunable, quasi defected ground structure (DGS) coplanar bandpass filter (BPF), which operates from 18 GHz to 26 GHz (K-band). The designed structure can be redesigned for an other frequency range by changing the geometrical parameters of the CPW. The bandpass filter occupies an area of 2.8×1.3 mm^2 and consists of *λ/4* open-end stub resonators coupled with a series gap capacitance. The use of MEMS series-resistive contact switches between the additional external metal stubs and the metallic ground planes permits systematic control of the resonance frequency and the pass-band width, thus, the control of the transmission zero in the frequency domain. Therefore, the designed bandpass filter has a wide upper stop-band and an improved symmetry of the pass-band response. The equivalent circuit model has also been developed. Simulations based on the proposed circuit model are in good agreement with the electromagnetic (EM) simulation. The BPF has been designed in CPW environment for high-resistivity silicon substrates and is, therefore, compatible with is suitable for standard MIS and MMIS technologies.

6.1 2-D Coplanar Bandpass Filter

The new 2-D coplanar quasi-DGS bandpass filter has been designed and analyzed using the full-wave 2.5-D planar MoM EM simulator Sonnet [159]. Figure 6.1 (a) shows a schematic drawing of the proposed 2-D resonant structure constructed on the open-end-coupled CPW line. The structure has been modeled on a high-resistivity (> 4 kΩ·cm) silicon substrate with a thickness of 735 µm and a dielectric constant of 11.9. The substrate is covered by a 1.0 µm thick silicon dioxide buffer layer. An aluminum layer of 2.0 µm thickness has been used as structure metallization. The CPW was designed for a characteristic impedance of 50 Ω which corresponds to a signal line width of W = 90 µm and slot width of G = 60 µm. Two external microstrip lines have been added on both sides of the structure. These stubs represent something like a defected ground structure but with a very low capacitive coupling.

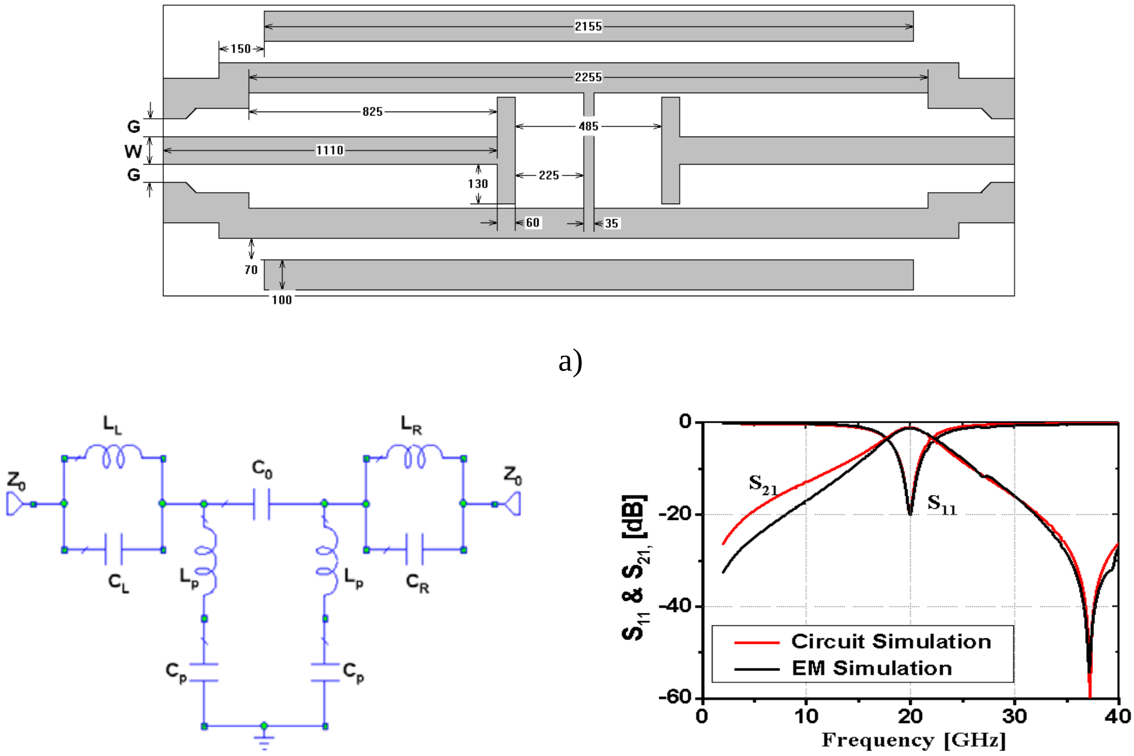

a)

b)

c)

Figure 6.1: Schematic drawing of the proposed 2-D coplanar bandpass filter (a); its lumped-elements equivalent circuit model (b); EM and equivalent circuit simulation results (c).

In order to suppress unwanted modes it is necessary to hold the ground planes at equal potential. Therefore, a thin metal line is added between the two resonators connecting the ground planes. The $\lambda/4$ open-end stubs are modeled as series L_pC_p resonators as shown in Figure 6.1 (b). The dominating central capacitive coupling is modeled with the capacitance C_0. The parallel C_LL_L and C_RL_R resonators represent the coupling between the center signal line and the ground planes including the external metal planes. The passive coplanar bandpass filter has been designed and optimized for the K-band with a resonant frequency of 20.0 GHz with two symmetrical cut-off frequencies and one transmission zero in the upper stop-band. The simulated insertion loss in the pass-band is about 1.0 dB with a stop-band rejection of more than -20 dB. A comparison between EM and equivalent circuit simulated responses are shown in Figure 6.1 (c). Both simulation results are in good agreement, therefore, the derived equivalent circuit can be used to design practical circuits. Figures 6.2 (a) and (b) show the simulated current density distribution at the transmission-zero frequency of 37.9 GHz and at the resonance frequency of 20.0 GHz, respectively. The transmission through the CPW signal line at the resonance frequency is observed while at the transmission zero no RF power passes through the filter.

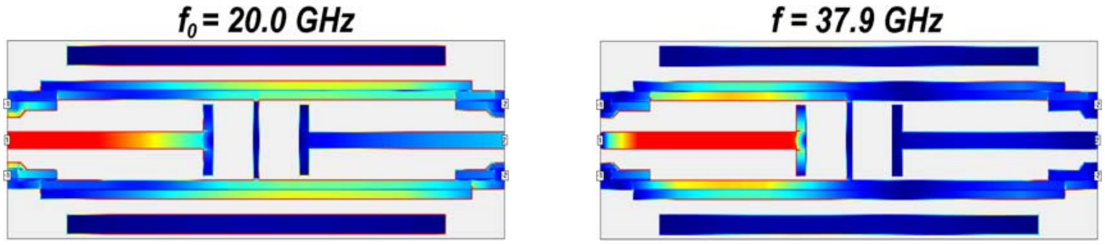

b) c)

Figure 6.2: Current density distribution in the designed 2-D coplanar BPF at the resonance frequency of 20.0 GHz (a) and at the transmission-zero frequency of 37.9 GHz (b).

6.2 Control of Resonance Frequency and Bandwidth of BPF

A new method to control the resonance frequency and the bandwidth of the proposed coplanar bandpass filter has been investigated. Due to the symmetry the filter structure can be segmented into four symmetrical quarters as shown in Figure 6.3 (a). The thin metal line “jumper” with an area of 20×70 μm^2 has been added between the ground and the external ground plane in the first quarter of the filter structure (see Figure 6.3 (a)). This jumper forms an electrical contact and, thus, changes the inductive and capacitive loading in the structure. Figure 6.3 (b) shows the current density distribution in the filter at the resonance frequency of 22.3 GHz. It can be clearly seen that the magnetic current, propagating through the ground plane, concentrates in the metal jumper and in the external metal line. It results in an increase of the magnetic coupling on one side of the center signal line. Corresponding to the equivalent circuit model the jumper adds the parallel inductances and capacitances to the parallel resonators L_LC_L and L_RC_R. Therefore, the total inductance of each parallel resonator is less than the initial inductance value. The inductances L_L and L_R on the left and the right sides of the structure, respectively, have different values. On the other hand the capacitances C_L and C_R of the parallel resonators are increased due to the increased area of the ground plane and have identical values. As the inductive loading dominates, the 3 dB bandwidth is decreased and the resonance frequency is shifted to higher frequencies, see Figure 6.3 (c). By variation of the distance a it is possible to control the inductive and the capacitive loading and, thus, to control the resonance frequency and the bandwidth of the designed BPF, as shown in Figure 6.3 (d) and (e). Figure 6.3 (f) shows the dependence of the equivalent circuit capacitances and inductances, extracted from the equivalent circuit model simulation, versus the distance a. With the presence of the metal jumper the equivalent capacitances C_L and C_R are equal and remain almost constant. The equivalent inductances L_L and L_R have different values, namely the inductance L_L at the metal jumper location is higher than L_R. The values of the both inductances increase as the distance a is increased and become equal at the center of the external metal line. The difference between them reduces with the displacement of the metal jumper toward the center of the structure and disappears when the jumper is removed as shown in Figure 6.3 (f).

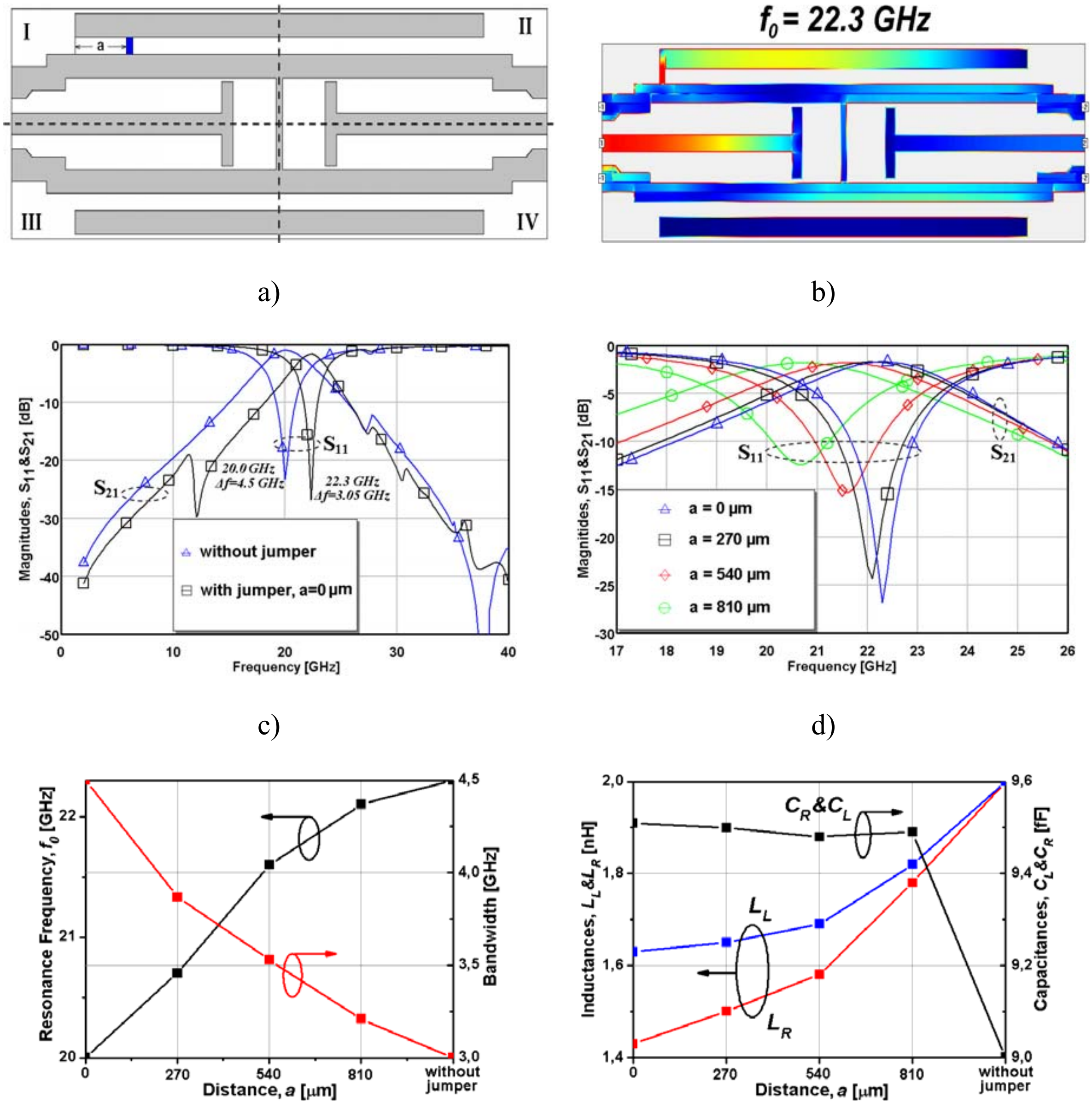

a) b)

c) d)

e) f)

Figure 6.3: Schematic drawing of the designed 2-D coplanar BPF with the metal jumper on one side (a). Simulated current density distribution at resonance (b), frequency responses of the BPF without and with metal jumper in the first quarter of the structure for a = 0 µm (c) and for different distances a (d). Resonance frequency and the bandwidth in dependence on the distance a (e) and equivalent inductances and capacitances vs. a distance a (e).

6.3 Tunable MEMS-Switch Controlled Quasi-DGS BPF

Figure 6.4 shows a schematic diagram of the proposed MEMS-switch controlled tunable, quasi-DGS coplanar BPF. It consists of the 2-D bandpass structure, investigated in the previous section, and eight RF MEMS series-resistive switches based on a fixed-fixed beam configuration. The tuning range of the filter covers almost the whole K-band for automotive application and transceivers, e.g. All RF MEMS switches are placed symmetrically on both sides of the signal line between the ground planes and the external metal lines as shown in Figure 6.5. Every switch in the down-state forms an electrical contact and joins the metal planes together in the certain locations.

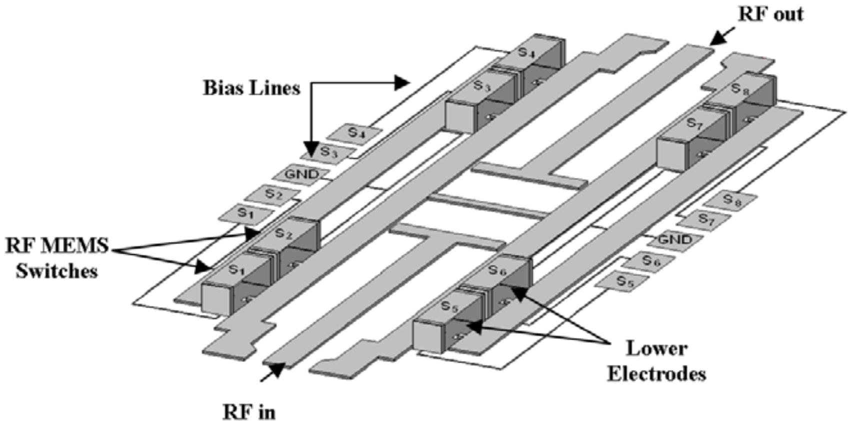

Figure 6.4: Scheme of the designed MEMS-switch controlled tunable BPF.

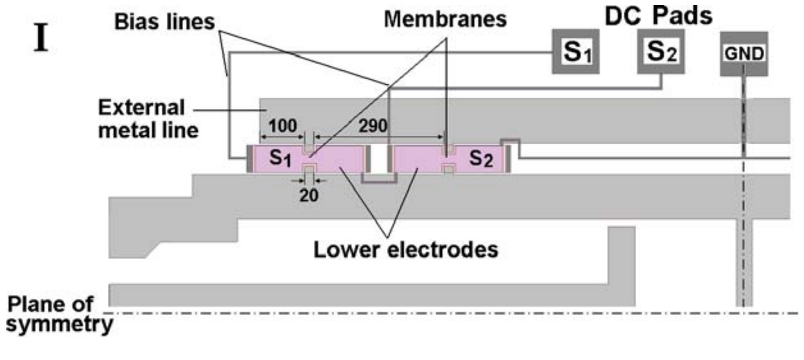

Figure 6.5: 2-D view of the first quarter of the MEMS-switch controlled tunable BPF, which is depicted in Figure 6.4.

Figure 6.6 (a) shows a scheme diagram of the fixed-fixed beam RF MEMS series ohmic-contact switch, which has been presented in [61]. These switches are combined with the 2-D bandpass filter structure, as shown in Figure 6.4. If they are actuated, the ohmic contact between the ground and the external metal plane is realised and, consequently, the properties of the bandpass structure will change. This results in a change of the resonance frequency and of the bandwidth of the filter. Length, width, and thickness of the MEMS membrane are 250 µm, 60 µm and 1.0 µm, respectively. The initial gap height over the lower electrode is 1.3 µm and 1.2 µm over the RF signal line. The MEMS switches are made of aluminum. The design of this switch allows to increase the areas of the lower electrodes and does not require dumbbells at the contact locations. It reduces the pull-down voltage and simplifies the fabrication process of the MEMS switches. The contact area is 20×20 µm^2. A highly doped polysilicon with a sheet resistance higher than 1400 Ω/□ can be used as material for the lower electrodes. Figure 6.6 (b) shows the FEM simulated result for the center deflection of the MEMS membrane versus the applied bias voltage for different values of the tensile residual stress.

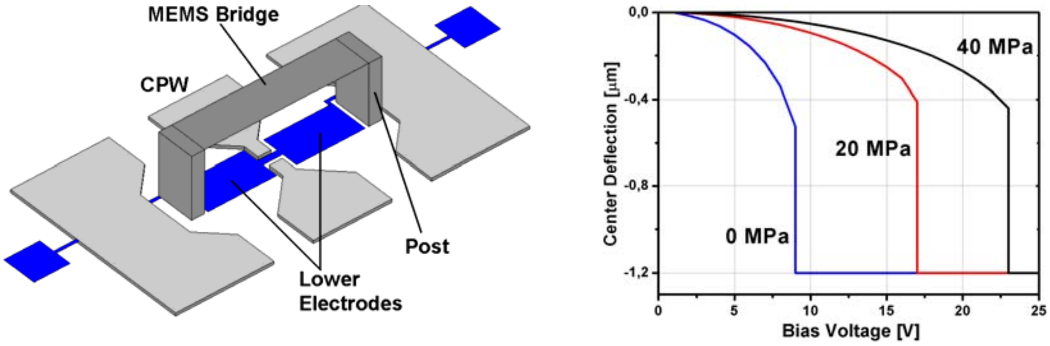

a) b)

Figure 6.6: Schematic drawing of the fixed-fixed beam RF MEMS series-resistive switch (a) and simulated center deflection vs. applied voltage for different values of tensile stress (b).

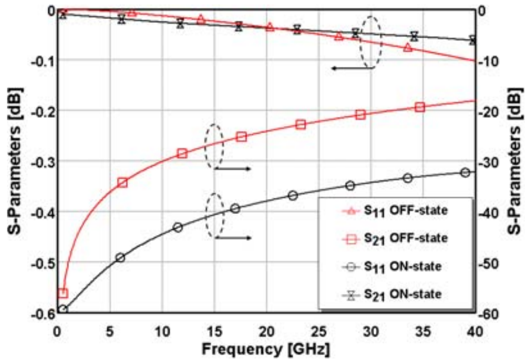

Figure 6.7: Simulated RF frequency response of the single-separate RF MEMS series-resistive switch in the ON- and in the OFF-states.

In the OFF-state the switch isolation is determined by the gap in the signal line under the bridge, which has a width of 20 µm in our case. In the ON-state the membrane is pulled down on the contact locations realising an electrical contact between them. The RF signal now passes through the switch structure. The simulated RF frequency responses of the RF MEMS series resistive-contact switch in both, the ON- and OFF- states are shown in Figure 6.7. In the ON-state, the insertion loss is less then 0.1 dB with a return loss higher than -30 dB up to 40 GHz. While in the OFF-state, the isolation is higher than -17 dB.

A system of RF MEMS switches controls the parameter values of the cascaded parallel L_LC_L and L_RC_R resonators in the equivalent circuit model shown in Figure 6.1 (b). The RF frequency response of the tunable coplanar BPF in the case of a zero applied bias voltage to all RF MEMS switches is almost the same as in the case of the 2-D coplanar BPF investigated in section 6.2 and shown in Figure 6.1 (c), but the bandwidth is reduced a little bit. The resonance frequency is at 20 GHz with a rejection higher than -20 dB. The simulated pass-band width is 4.3 GHz. The filter quality factor can be determined by [157]:

$$Q = \frac{\omega_0}{\Delta\omega} \tag{6.1}$$

where ω_0 is the resonance frequency and $\Delta\omega$ is the bandwidth. The calculated Q-factor including the effect of the CPW line length and the RF MEMS switches is about 4.65.

The eight RF MEMS switches, which can be actuated individually, allow to obtain 2^8 independent states. Due to the structure symmetry, only 2^6 states are available. The lowest (20.0 GHz) and the highest (22.5 GHz) resonance frequencies are obtained by “no switches are actuated” and “switches S_1, S_2, S_3, S_5, and S_6 are actuated”, respectively. Between these 64 states can be realised providing a small discrete frequency steps between the upper and lower limit.

The loaded filter structure has been simulated for combinations of differently actuated RF MEMS switches in order to get the RF frequency response.

The following combinations have been chosen to describe the performance of the tunable filter in different states of the MEMS switches:

Combination 1: The MEMS switches S_2 and S_4 are actuated. In this case the loading is changed on one side in two quarters of the filter structure. As a result, the resonance frequency is shifted from 20 GHz to 22 GHz.

Combination 2: The MEMS switches S1 and S2 are actuated. The loading is applied to one side and the first quarter of the structure is loaded. The filter in this case operates with a resonance frequency of 22.3 GHz.

Combination 3: The MEMS switches S1, S4 and S7 are actuated. In this case the loading is applied to both sides of the structure, whereby the quarters I, II and IV are loaded. Therefore, the resonance frequency is changed an amount to 22.7 GHz.

Combination 4: The MEMS switches S1, S3 and S7 are actuated. As in the previous case the structure is loaded on both sides, so that the resonance frequency increases further to 22.9 GHz.

Combination 5: The MEMS switches S1, S2 and S4, S8 are actuated. In this case the bandpass filter is loaded in three quarters of the structure. The resonance frequency in this case is 23.1 GHz.

Combination 6: The MEMS switches S1, S2 and S3, S8 on both sides are actuated. Three quarters are loaded, the resonance frequency has a value of 23.3 GHz.

Combination 7: The MEMS switches S1 and S6 are actuated. In this case the quarters I and III on both sides of the structure are loaded. As a result, the resonance frequency increases to 23.7 GHz.

The simulated reflection coefficient S_{11} and the simulated transmission coefficient S_{21} in all these cases are presented in Figure 6.8 (a) and (b), respectively. The rejection in the pass-band is higher than -30 dB for all the cases.

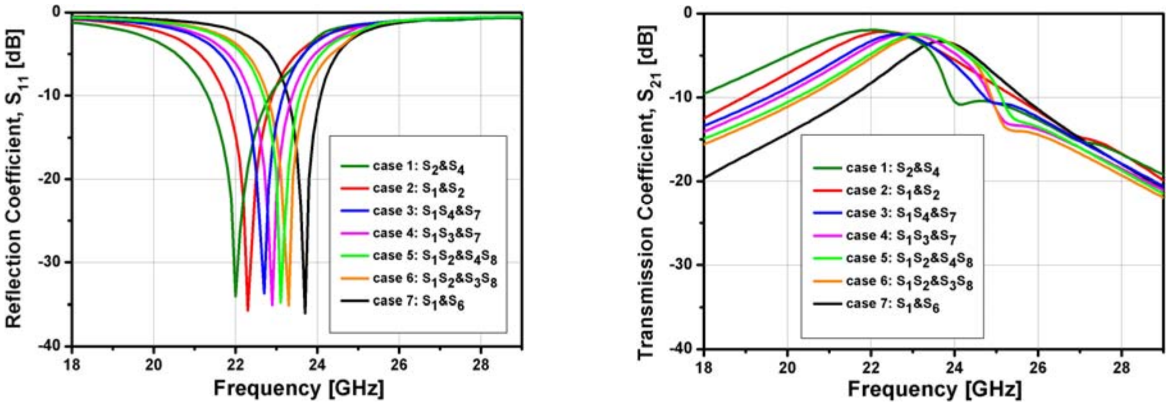

a) b)

Figure 6.8: Simulated RF frequency responses of the proposed tunable BPF for the different cases of actuated MEMS switches, as outlined above: (a) reflection coefficient S_{11} and transmission coefficient S_{21} (b).

The simulated resonance frequency and the filter pass-band width for the combinations of the actuated MEMS switches mentioned above are shown Figure 6.9. As can be seen for the combinations 3, 4, 5, and 6 the bandwidth of the filter structure remains almost constant, namely around 2.15 GHz. In these cases more than two MEMS switches are actuated and at least tree quarters of the structure are loaded. These findings can be understood that the capacitive loading of the cascaded parallel resonators is constant and more stable as more than two quarters are loaded. Therefore, it can be concluded that the presented tunable bandpass filter for these combinations operates as an inductively controlled structure.

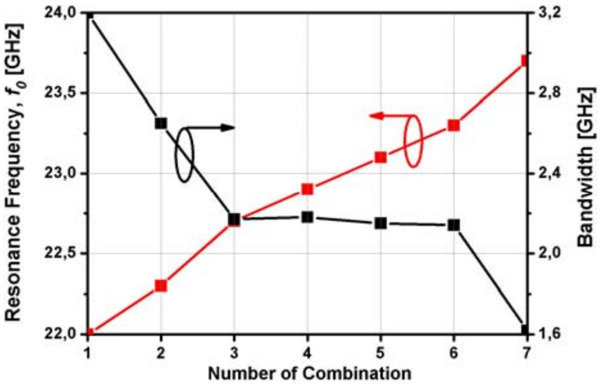

Figure 6.9: Variations of the resonance frequency and the bandwidth of the tunable BPF for different cases of actuated MEMS switches.

6.4 Summary

In this chapter, a RF MEMS-switch controlled, tunable bandpass filter for K-band applications has been designed and investigated. The filter structure is based on two-dimensional quasi defected ground structure in CPW environment and fixed-fixed beam RF MEMS series-resistive switches. The structure has been designed on high-resistivity silicon substrate that is suitable for monolithic integration using CMOS compatible surface micromachining technology. The tuning of the designed filter structure has been provided using a system of RF MEMS series-resistive switches which controls the inductive-capacitive loading of the filter structure. An equivalent circuit has been developed to describe the behavior of the bandpass filter by modeling. The EM and circuit simulations are in a good agreement validating the proposed equivalent circuit model. Simulations have shown that it is possible to control the resonance frequency as well as the bandwidth of the filter. The properties of the filter depend on the number of the loaded quarters of the structure. The designed structure is very flexible to be designed for different frequency bands since the resonance frequency and the bandwidth can be controlled by the geometrical parameters of the 2-D coplanar bandpass structure.

Chapter 7

Conclusions

Design, modeling, simulation and fabrication of radio-frequency (RF) micro-electro-mechanical system (MEMS) switches were the matter of this thesis. It also introduced design and characterization of RF filters in coplanar waveguide (CPW) implementation. Defected ground structures (DGS) were investigated in order to improve the characteristics of coplanar filters. Finally, both MEMS switches and DGS were combined to design a tunable coplanar bandpass filter.

The electromechanical modeling was carried out by using the finite element method (FEM). The ANSYS FEM simulation platform was used in this investigation. Two algorithms to solve the electrostatic problem were implemented. One is the sequential coupling method which allowed the combination of the strength of single field simulators. The electrostatic problem is based on the solution of the Laplace's equation in the different homogenous regions. The second method to solve the electrostatic problem was the lumped or reduced order model. This method was implemented using lumped transducer elements which converted the stored electrostatic energy into mechanical energy and vice versa. The mechanical model to determine the deformation of the membrane under acting of the electrostatic force was obtained following the plate/shell theory. The sequential coupling algorithm led to results of high accuracy as the fringing field effect was taken into account. But this algorithm required much more computational time than the lumped or reduced order model.

The effect of the residual stress on the structure behaviour was also investigated. It was shown the initial biaxial tensile stress could increase the pull-down voltage significantly.

The concept of a low actuation-voltage, high isolation RF MEMS switches was introduced and investigated in chapter 3. The switches were based on the proposed H-shape membrane with a low spring constant fixed-fixed flexure suspension. Shunt-capacitive and shunt-resistive modifications were modeled and optimized. The simulated base-model of the H-shape RF MEMS switch was useful for X-band applications and provided an ON-state insertion loss less than 0.2 dB with a return loss of more than -18 dB. The simulated OFF-state isolation was higher than -20 dB for frequencies from 7.0 GHz up to 40 GHz for the shunt-capacitive switch and higher than -25 dB for frequencies from dc up to 40 GHz for the shunt-resistive structure. The FEM simulated pull-down voltage was less than 25 V for the membrane with biaxial tensile stress of 20 MPa.

A dc-contact RF MEMS shunt-capacitive switches based on the proposed H-shape membrane was introduced, simulated and optimized for S- and L-band applications. The S-band MEMS shunt-capacitive switch provided an ON-state insertion loss less than 0.3 dB with a return loss higher than -25 dB from dc up to 35 GHz. The simulated OFF-state isolation was higher than -20 dB from 1.5 GHz up to 35 GHz. The predicted OFF/ON-state capacitance ratio was higher than 3.8×10^3. The simulated pull-down voltage lied in the range from 9.0 V to 12 V for the membrane with a biaxial tensile stress of 20 MPa. Even for a residual stress of 40 MPa the pull-down voltage did not exceed 15 V. The designed L-band MEMS switch had an ON-state insertion loss less than 0.8 dB with a return losses higher than -40 dB from dc up to 40 GHz. The OFF-state isolation was higher than -20 dB from 0.8 GHz up to 40 GHz. The simulated pull-down voltage was 9.0 V and 12.0 V for the membranes with a biaxial tensile stress of 20 MPa and 40 MPa, respectively.

The proposed designs of RF MEMS switches were completely based on CMOS compatible fabrication steps and processes.

The fabrication process of conventional RF MEMS switches in the fixed-fixed beam configuration was described in chapter 4. The switches were fabricated in a clean-room using surface micromachined techniques compatible with standard CMOS technology. Each fabrication step was described in details. High quality silicon nitride films were deposited using the electron cyclotron resonance plasma enhanced chemical vapor deposition (ECR-PECVD) method at 50 $^\circ$C. The influence of the gas mixture, namely the SiH_4/N_2 ratio, on the film properties was studied. The dielectric constant of the nitride films obtained with optimized deposition conditions was 7.9, the average surface roughness 1.15 nm. The measured breakdown field strength of a sample processed with the SiH_4/N_2 ratio of 1:6 was 7.9 MV/cm at $J = 12$ µA/cm^2 and deceased to 5.9 MV/cm as the ratio was increased to 1:1.

The measured ON-state insertion loss of the fabricated switches was less than 0.5 dB with a return loss less than -10 dB up to 40 GHz. The OFF-state isolation was higher than -18 dB for frequencies from 6 GHz up to 40 GHz. The measured pull-down voltage of the fabricated switches was in range of 24-30 V.

In chapter 5, designs of RF filters constructed in CPW environment were presented. Several different approaches were proposed to realize the filter structures. Two bandpass filters (BPF) were designed using capacitively end-coupled method and inductively shunt-coupled line approach. The first bandpass filter was designed by using *λ/4* open-end stub resonators coupled by gap capacitance. The second BPF was designed using meander serpentine-shape *λ/2* shunt-stubs that reduced the filter size and improved its RF performance.

The performance of the conventional dumbbell DGS slots was improved by using the fractal geometry. For the designed quasi-fractal DGS the capacitance value was more than 30 % higher than for the capacitance of the standard rectangular DGS. It allowed to shift the resonance pole to lower frequencies.

A coplanar capacitively coupled DGS low-pass filter was designed and optimized. The filter was constructed on coplanar line, which was periodically loaded with arrowhead triangular DGS slots. A new compact high performance coplanar ultra wideband low-pass filter (UWB LPF) with improved stop-band characteristic was designed by using *λ/4* open-end stub resonators combined with novel shape DGS. The designed filter showed wide (more than 20 GHz) and deep stop-band characteristics.

In chapter 6, RF MEMS-switch controlled tunable bandpass filter for K-band applications was designed and investigated. The filter structure was based on quasi-DGS in CPW environment and RF MEMS series-resistive switches. The tuning of the designed filter structure was performed by the control of the inductive-capacitive loading of the structure. Simulations showed that it was possible to control the resonance frequency as well as the bandwidth of the filter. It depended on the number of the loaded quarters of the filter structure.

Bibliography

[1] James J. Allen, *Micro electro mechanical system design*, Taylor & Francis Group, LLC, 2005.

[2] J. J. Yao, “Topical Review: RF MEMS From a Device Perspective,” *J. Micromech. Microeng.*, Vol. 10, No. 4, pp. R9-R38, December 2000.

[3] S. Beeby, G. Ensell, M. Kraft, and N. White, *MEMS Mechanical Sensors*, Nordwood, Artech Hous, Inc., 2004.

[4] S. Lucyszyn, “Review of Radio Frequency Microelectromechanical Systems Technology,” *IEE Proceedings - Science, Measurement and Technology*, Vol. 151, No. 2, pp. 93-103, March 2004.

[5] G. M. Rebeiz and J. B. Muldavin, “RF MEMS Switches and Switch Circuits,” *IEEE Microwave magazine*, pp. 59-71, December 2001.

[6] E. R. Brown, “RF-MEMS Switches for Reconfigurable Integrated Circuits,” *IEEE Trans. Microwave Theory Tech.*, Vol. 46, No. 11, pp. 1868-1880, November 1998.

[7] H. A. C. Tilmans, W. D. Raedt, and E. Beyne, “MEMS for Wireless Communications: from RF-MEMS Components to RF-MEMS-SiP,” *J. Micromech. Microeng.*, Vol. 13, No. 4, pp. S139-S163, July 2003.

[8] H. J. D. L. Santos and R. J. Richards, “MEMS for RF/Microwave Wireless Applications: The Next Wave Part I,” *Microwave Journal*, March 2001.

[9] L. P. B. Katehi, E. Harvey, and E. Brown, “MEMS and Si Micromachined Circuits for High-Frequency Applications,” *IEEE Trans. Microwave Theory Tech.*, Vol. 50, No. 3, pp. 858-866, March 2002.

[10] R. Mahameed, M. B. Pisani, N. Sinha, G. Piazza, “Dual-Beam Actuation of Piezoelectric AlN RF MEMS Switches Monolithically Integrated with AIN Contour-Mode Resonators,” *Journal of Micromech. Microeng.*, Vol. 18, Issue 10, October 2008.

[11] Y. Choi, K. Kim, M. G. Allen, “High standoff dual-mode-actuation MEMS switches,” *Microsyst Technol.,* Vol. 15, pp. 777-787. 2009.

[12] Y. Kwon and S. Lee, “RF MEMS - Enabling Technology for Millimeter-Waves,” IEICE *Trans. Electron.*, Vol. E89–C, No.7, pp. 898-905, July 2006.

[13] K. Entesari and G. M. Rebeiz, “A 12–18-GHz Three-Pole RF MEMS Tunable Filter,” *Microwave Theory and Techniques*, Vol. 53, No. 08, August 2005.

[14] K. M. Strohm, F. J. Schmückle, B. Schauwecker, J.-F. Luy, W. Heinrich: “Silicon Micromachined RF MEMS Resonators,” *Digest of IEEE MTT-S, Int. Microwave Symposium*, Seattle, Vol. 2, pp. 1209-1212, 2002.

[15] Ch. W. Jung, B. Lee, F. D. Flaviis, “In-Line RF-MEMS Series Switches for Reconfigurable Antenna Applications,” *Microwave and Optical Technology Letters*, Vol. 49, No. 12, pp. 3130- 3134, December 2007.

[16] Bo-Shi Jin, Yu-Ming Wu, Qun Wu, Hao-Yuan She, and Le-Wei Li, “An Improved Design for Ka-Band Phase Shifter Using An Improved Design for Ka-Band Phase Shifter Using,” *Progress In Electromagnetics Research Symposium 2005*, Hangzhou, China, August 2005.

[17] W. Palei, A. Q. Liu, A. B. Yu, A. Alphones, Y. H. Lee, “Optimization of design and fabrication for micromachined true time delay (TTD) phase shifters,” *Sensors and Actuators* A, Vol. 119, pp. 446-454, March 2005.

[18] E. Burte, R. Mikuta, G. Kuhlemann, J. Urban, “128 Pixel Infrared Focal Plane Array Produced in Pure CMOS Technology,” EUORSENSORS 2006, Gothenburg (Sweden), Bd. 2, pp. 66 – 67, September 2006.

[19] Y. Cheng, B.-Y. Shew, M.K. Chyu, P.H. Chen, “Ultra-deep LIGA process and its applications,” *Nuclear Instruments and Methods in Physics Research,* A 467–468, pp. 1192–1197, 2001.

[20] L. E. Larson, R. H. Hackett, M. A. Melendes, and R. F. Lohr, “Micromachined microwave actuator (MIMAC) technology - a new tuning approach for microwave integrated circuits,” in *Microwave and Millimeter-Wave Monolithic Circuits Symposium Digest*, Boston, MA, pp. 27–30, June 1991.

[21] K. E. Petersen, “Micromechanical Switches on Silicon,” *IBM Journal of Research and Development*, Vol. 23, No. 4, pp. 376–385, July 1971.

[22] K. E. Petersen, “Silicon as a Mechanical Material,” *Proceedings of the IEEE*, Vol. 70, No. 5, pp. 420–457, May 1982.

[23] P.J. French, “Polysilicon: A Versatile Material for Microsystems,” *Sensors and Actuators A Physical*, Vol. A 99, No. 1-2, pp. 3–12, April 2002.

[24] C. L. Goldsmith, Z. Yao, S. Eshelman, and D. Denniston, “Performance of Low-loss RF MEMS Capacitive Switches,” *IEEE Microwave and Guided Wave Letters*, Vol. 8, No. 8, pp. 269–271, August 1998.

[25] R. N. Tait, “An IC Compatible Process for Fabrication of RF Switches and Tunable Capacitors,” *Journal of Elect and Comp. Eng.*, Vol. 25, pp. 245-253, Jan. 2000.

[26] J. B. Muldavin and G. M. Rebeiz, “Novel DC-Contact MEMS Shunt Switches and High-Isolation Series/Shunt Designs,” *European Microwave Conference*, Excel, London, U.K., pp. 275-277, September 2001.

[27] L. Wang, Z. Cui, J.-S. Hong, E. P. McErlean, R. B. Greed, D. C. Voyce, “Fabrication of high power RF MEMS switches,“ *J. Microelectronic Engineering*, Vol. 83, pp. 1418–1420, February 2006.

[28] D. Balaraman, S. K. Bhattacharya, F. Ayazi, J. Papapolymerou, “Low-Cost Low Actuation Voltage Copper RF MEMS Switches”, *IEEE MTT-S Int. Microwave Symp. Dig.*, Seattle, Washington, Vol. 2, pp. 1225-28, June 2002.

[29] Y.-T. Song, H.-Y. Lee, and M. Esashi**, “**Low Actuation Voltage Capacitive Shunt RF-MEMS Switch Having a Corrugated Bridge,” *IEICE Trans. Electron.*, Vol. E89–C, No.12, pp. 1880-1887, December 2006.

[30] P. Ekkels, X. Rottenberg, R. Puers and H. A. C. Tilmans, “Evaluation of platinum as a structural thin film material for RF-MEMS devices,” *J. Micromech. Microeng.*, Vol. 19, pp. 1-8, May 2009.

[31] R. Chan, R. Lesnick, D. Becher and M. Feng, “Low-Actuation Voltage RF MEMS Shunt Switch With Cold Switching Lifetime of Seven Billion Cycles,” *J. Micromech. Systems*, Vol. 12, No. 5, pp. 713-719, October 2003.

[32] S. P. Pacheco, L. P. B. Katehi and C. T.-C. Nguyen, “Design of Low Actuation Voltage RF MEMS Switch,” *2000 IEEE MTT-S Int. Microwave Symp. Dig.,* Boston, Vol. 1, pp. 165-168, June 2000.

[33] S. Touati, N. Lorphelin, A. Kanciurzewski, R. Robin, A.-S. Rollier, O. Millet, K. Segueni, “Low Actuation Voltage Totally Free Flexible RF MEMS Switch With Antistiction System,” *Design, Test, Integr. & Packag. MEMS/MOEMS (DTIP) Symp.,* French Riviera, April 2008.

[34] S.-D. Lee, B.-C. Jun, S.-D. Kim and J.-K. Rhee, “A Novel Pull-Up Type RF MEMS Switch with Low Actuation Voltage,” *IEEE Microw. Wirel. Comp. Lett*., Vol. 15, No. 12, pp. 856-858, December 2005.

[35] R. Robin, S. Touati, K. Segueni, O. Millet, L. Buchaillot, “A new four states high deflection low actuation voltage electrostatic MEMS switch for RF applications,” *Design, Test, Integr. & Packag. MEMS/MOEMS (DTIP) Symp.,* French Riviera, April 2008.

[36] D. Peroulis, S. P. Pacheco, K. Sarabandi and L. P. B. Katehi, “Electromechanical Considerations in Developing Low-voltage RF MEMS Switches,” *IEEE Trans. Microwave Theory Tech.*, Vol. 51, No. 1, pp. 259-270, January 2003.

[37] L. L. Mercado*,* S.-M. Kuo, T.-Y. (Tom) Lee*,* R. Lee, “Analysis of RF MEMS Switch Packaging Process for Yield Improvement,” *IEEE Transactions on Advanced Packaging*, Vol. 28, No. 1, February 2005.

[38] M. E. Khatib, A. Pothier, A. Crunteanu, P. Blondy, “A novel packaging approach for RF MEMS switching functions on alumina substrate,” *J. Microsys. Technol.,* Vol. 13, pp. 1457-1461, January 2007.

[39] G. M. Rebeiz, *RF MEMS Theory, Design, and Technology*, 1st ed. Hoboken, New Jersey: John Wiley & Sons, Inc., June 2003.

[40] Scotten W. Jones, “Understanding the costs of MEMS products,” IC Knowledge LLC, http://www.icknowledge.com, 2009.

[41] J.Y. Park, G.H. Kim, K.W. Chung, J.U. Bu, “Monolithically integrated micromachined RF MEMS capacitive switches,” *Sensors and Actuators A: Physical*, Vol. 89, pp. 88–94, 2001.

[42] C.-L. Dai and Y.-L. Chen, “Modeling and Manufacturing of Micromechanical *RF Switch* with Inductors,” *Sensors 2007,* Vol. 7 (11), pp. 2660-2670, November 2007.

[43] Y. Liu, “High Isolation BST MEMS Switches,” in *IEEE MTT-S International Microwave Symposium Digest*, Vol. 1, pp. 227-230, 2002.

[44] Z. Wang, J. Liu, T. Ren, L. Liu, “Fabrication of organic PVP doping-based $Ba_{0.5}Sr_{0.5}TiO_3$ thick films on silicon substrates for MEMS applications,” *Sensors and Actuators A: Physical*, Vol. 117*,* Issue 2, pp. 293-300, January 2005.

[45] G. Wang, T. Polley, A. Hunt, and J. Papapolymerou, “A High Performance Tunable RF MEMS Switch Using Barium Strontium Titanate (BST) Dielectrics for Reconfigurable Antennas and Phased Arrays,” *IEEE Antennas and Wireless Propagation Letters*, Vol. 4, pp. 217-220, 2005.

[46] M. Fernández-Bolaños, J. Perruisseau-Carrier, P. Dainesi and A.M. Ionescu, “RF MEMS capacitive switch on semi-suspended CPW using low-loss high-resistivity

silicon substrate," *J. Microelectronic Engineering,* Vol. 85, Issues 5-6, pp. 1039-1042, May-June 2008.

[47] Y. Liu, *MEMS and BST Technologies for Microwave Applications*, Ph.D. thesis, University of California, Electrical and Computer Engineering, Santa Barbara, 2002.

[48] A. B. Yu, A. Q. Liu, Q. X. Zhang, A. Alphones, H. M. Hosseini, "Micromachined DC contact capacitive switch on low-resistivity silicon substrate," *Sensors and Actuators* A, Vol. 127, pp. 24-30, 2006.

[49] R. E. Mihailovich, M. Kim, J. B. Hacker, E. A. Sovero, J. Studer, J. A. Higgins, and J. F. DeNatale, "MEM Relay for Reconfigurable RF Circuits," *IEEE Microwave Wireless Comp. Lett.*, Vol. 11, No. 2, pp. 53-55, February 2001.

[50] V. K. Varadan, K. J. Vinoy, and K. A. Jose, *RF MEMS and Their Applications*, 1st ed. Pennsylvania State University, USA: John Wiley & Sons, Inc., December 2002.

[51] L. Chen, H. Lee, Z.J. Cuo, N. E. McGruer, K. W. Gilbert, K. D. Leedy, G. G. Adams, "Contact resistance study of noble metals and alloy films using a scanning probe microscope test station," *J. of Applied Physics*, Vol. 102, 074910, October 2007.

[52] S. Majumder, N. E. McGruer, G. G. Adams, P. M. Zavravsky, "Study of contacts in an electrostatically actuated microswitch," *Sensors and Actuators A: Physical*, Vol. 93, pp. 19-26, 2001.

[53] E. Hamad, A. Elsherbeni, A. Safwat, and A. Omar, "Two-dimensional Coupled Electrostatic-Mechanical Model for RF MEMS Switches," *Applied Computational Electromagnetic Society (ACES) Journal*, Vol. 21, No. 1, pp. 26-36, March 2006.

[54] J. A. Wright, Y.-C. Tai, "Magnetostatic MEMS Relays for the Miniaturization of Brushless DC Motor Controllers," *Digest of 12th IEEE Int. Conf. on Micro Electro Mech. Sys.*, pp. 594-599, 1999.

[55] J.-H. Park, H.-C. Lee, Y.-H. Park, Y.-D. Kim, C.-H. Ji, J. Bu and H.-J. Nam, "A fully wafer-level packaged RF MEMS switch with low actuation voltage using a piezoelectric actuator," *J. Micromech. Microeng.*, Vol. 16, pp. 2281–2286, September 2006.

[56] D. Girbau, L. Pradell, A. Lázaro, and À. Nebot, "Electrothermally Actuated RF MEMS Switches Suspended on a Low-Resistivity Substrate," *J. Microelectromech. Syst.,* Vol. 16, No. 5, pp. 1061–1070, October 2007.

[57] J. Wibbeler, G. Pfeifer, M. Hietschold, "Parasitic charging of dielectric surfaces in capacitive microelectromechanical systems (MEMS)," *Sensors and Actuators A: Physical*, Vol. 71, pp. 74–80, 1998.

[58] W. M. Spengen, R. Puers, R. Mertens and I. D. Wolf, "A comprehensive model to predict the charging and reliability of capacitive RF MEMS switches", *J. Micromech. Microeng*. Vol. 14, pp. 514-521., 2004.

[59] S. T. Patton, J. S. Zabinski, "Effects of dielectric charging on fundamental forces and reliability in capacitive microelectromechanical systems radio frequency switch contacts," *J. Appl. Phys.,* vol. 99, issue 9, pp. 1700-1710, May 2006.

[60] C. Goldsmith, J. Ehmke, A. Malczewski, B. Pillans, S. Eshelman, Z. Yao, J. Brank, M. Eberly, "Lifetime Characterization of Capacitive RF-MEMS Switches," *IEEE MTT-S, Int. Microwave Symposium Dig.,* Phoenix, AZ, USA, pp. 227-230, May 2001.

[61] J. B. Muldavin and G. M. Rebeiz, "All-Metal High-Isolation Series and Series/Shunt MEMS switches," *IEEE Microwave Wireless Comp. Lett.*, Vol. 11, pp. 373-375, September 2001.

[62] M. Jahanbakht, M. N. Moghaddasi, and A. A. Lotfi Neyestanak, "Low Actuation Voltage Ka-Band Fractal MEMS Switch," *Progress In Electromagnetics Research C,* Vol. 5, pp. 83-92, 2008.

[63] S. Majumder, J. Lampen, R. Morrison, and J. Maciel, "A Packaged, High-Lifetime Ohmic MEMS RF Switch," *IEEE MTT-S Int. Microwave Symp. Dig.,* Philadelphia, Pennsylvania, USA, pp. 1935-39, June 2003.

[64] J. B. Rizk, G. M. Rebeiz, "W-Band CPW RF MEMS Circuits on Quartz Substrates," *IEEE Trans. Microwave Theory Tech.*, Vol. 51, No. 7, pp.1857-1862, July 2001.

[65] M. Tang, A. B. Yu, A. Q. Liu, A. Agarwal, S. Aditya, Z. S. Liu, "High isolation X-band MEMS capacitive switches," *Sensors and Actuators A: Physical*, Vol. 120, Issue 1, pp. 241-248, April 2005.

[66] R. Chan, R. Lesnick, D. Caruth, and M. Feng, "Ultra Broadband MEMS Switch on Silicon and GaAs Substrates", *Dig. Int. Conference on Compound Semiconductor Manufacturing Technology,* Tampa, Florida, USA, 2003.

[67] W.-B. Zheng, Q.-A. Huang, X.-P. Liao, F.-X. Li, "RF MEMS Membrane Switches on GaAs Substrates for X-Band Applications," *IEEE/ASME J. Microelectromech. Syst.*, Vol. 14, No. 3, pp. 464-471, June 2005.

[68] iSuppli Applied Market Intelligence, http://www.isuppli.com/

[69] J.-H. Park, "Fabrication and measurements of direct contact type RF MEMS switch," *IEICE Electronics Express*, Vol. 4, No. 10, pp. 319-325, May 2007.

[70] Z. J. Yao, S. Chen, S. Eshelman and C. Goldsmith, "Micromachined Low-Loss Microwave Switches," *IEEE/ASME J. Microelectromech. Syst.*, Vol. 8, No. 2, pp. 129-134, June 1999.

[71] S. Timoshenko, S. Woinowsky-Kreiger, *Theory of Plates and Shells*, McGraw-Hill, New York, 1959.

[72] E. Ventsel and T. Krauthamme, *Thin Plates and Shells: Theory, Analysis, & Applications*, 1st ed. New York: Marcel Dekker, Inc., 2001.

[73] P. Osterberg, H. Yie, X. Cai, J. White, and S. Senturia, "Self-Consistent Simulation and Modeling of Electrostatically Deformed Diaphragms," *17th IEEE Int. Conference on Microelectromech. Syst., MEMS'94,* Oiso, Japan, pp. 28-32, January 1994.

[74] P. M. Osterberg, and S. D Senturia, "M-test: A Test Chip for MEMS Material Property Measurement using Electrostatically Actuated Test Structures," *Journal of Microelectromech. Syst.,* Vol. 6, pp. 107-118, June 1997.

[75] P. Osterberg, R. Gupta, J. Gilbert, and S. Senturia, "Quantitative Models for the Measurement of Residual Stress, Poisson's Ratio, and Young's Modulus Using Electrostatic Pull-in of Beams and Diaphragms," *Tech. Digest of Solid-State Sensor and Actuator Workshop*, pp. 184-188, 1994.

[76] J. B. Muldavin and G. M. Rebeiz, "High-Isolation CPW MEMS Shunt Switches-Part 1: modeling," *IEEE Trans. Microwave Theory Tech.*, Vol. 48, No. 6, pp.1045-52, June 2000.

[77] S. Pacheco, C.T. Nguyen, L.P.B. Katehi, "Micromechanical electrostatic K-band switches," *Digest of IEEE MTT-S, Int. Microwave Symposium*, pp. 1569–1572, 1998.

[78] J.B. Rizk, G.M. Rebeiz, W-Band microstrip RF-MEMS switches and phase shifters, *Digest of IEEE MTT-S, Int. Microwave Symposium,* pp. 1485–1488, 2003.

[79] J. B. Muldavin and G. M. Rebeiz, "High-Isolation CPW MEMS Shunt Switches-Part 2: design," *IEEE Trans. Microwave Theory Tech.*, Vol. 48, No. 6, pp.1053-1056, June 2000.

[80] J.-M. Huang, K. Liew, C. Wong, S. Rajendran, M. Tan, and A. Liu, "Mechanical Design and Optimization of Capacitive Micromachined Switch," *Sensors and Actuators A: Physical*, Vol. 93, No. 3, pp. 273-285, October 2001.

[81] B. Choi and E. G. Lovell, "Improved Analysis of Microbeams Under Mechanical and Electrostatic Loads," *J. Micromech. Microeng.*, Vol. 7, No. 1, pp. 24-29, March 1997.

[82] L. Zhang, T. Yu, and Y. Zhao, "Numerical Analysis of Theoretical Model of the RF MEMS Switches," *Acta Mechanica Sinica*, Vol. 20, No. 2, pp. 178-184, April 2004.

[83] E. K. I. Hamad, Modeling, *Design, and Optimization of Radio-Frequency Microelectromechanical Structures*, Ph.D. thesis, University of Magdeburg, FEIT, IESK, 2006.

[84] H. D. Espinosa, M. Fischer, Y. Zhu, and S. Lee, "3-D Computational Modeling of RF MEMS Switches," *Technical Proceedings of the 4th Int. Conf. on Modeling and Simulation of Microsystems,* South California, USA, Vol. 4, pp. 402-405, March 2001.

[85] Matlab™, http://www.matlab.com

[86] Spice Resources, http://sss-mag.com/spice.html

[87] VisSim, http://www.vissim.com

[88] http://www.analogy.com

[89] CoventorWare, Coventor, Inc., http://www.coventor.com

[90] IntelliSuite, IntelliSense Software Corp, http://www.intellisensesoftware.com

[91] Ansys Release 9.0, ANSYS Inc., http://www.ansys.com

[92] Abaqus, ABAQUS, Inc., http://www.hks.com

[93] MEMSCAP, http://www.memscap.com

[94] M. Gyimesi and D. Ostergaard, "Electro-Mechanical Transducer for MEMS Analysis in ANSYS," *Int. Conf. Modeling/Simulation of Microsystems MSM99*, Chapter 7, pp. 270-273, 1999.

[95] Y. Zhu and H. D. Espinosa, "Electromechanical Modeling and Simulation of RF MEMS Switches," *4th International Symposium on MEMS and Nanotechnology, Charlotte*, North Carolina, Paper 190, pp. 8-11, June 2003.

[96] I. V. Avdeev, *New Formulation for Finite Element Modeling Electrostatically Driven Microelectromechanical Systems*, Ph.D. thesis, University of Pittsburgh, School of Engineering, 2003.

[97] V. Rochus, *Finite element modeling of strong electro-mechanical coupling in MEMS*, Ph.D. thesis, Universite de Liege, 2006.

[98] G. Rezazadeh, H. Sadeghian, E. Malekpour, “A Comparison Simulation of Fixed-Fixed Type MEMS Switches,” *J. Physics*: *Conference Series*, Vol. 34, pp. 500-505, 2006.

[99] C. F. Herrmann, F. W. Del Rio, S. M. George, and V. M. Bright, “Properties of Atomic Layer Deposited Al_2O_3/ZnO Dielectric Films Grown at Low Temperature for RF MEMS,” *Proc. of SPIE*, Vol. 5715, pp. 159-166, 2005.

[100] H. A. C. Tilmans, M. D. J. van de Peer, and E. Beyne, “The indent reflow sealing (IRS) technique - a method for the fabrication of sealed cavities for MEMS devices,” *J. Microelectromech. Syst.,* Vol. 9, pp. 206–217, June 2000.

[101] J. A. Thornton and D.W. Hoffman, “Stress Related Effects in Thin Films,” *J. Thin Solid Films*, Vol. 171, No. 1, pp. 5–31, April 1989.

[102] S. M. Hu, “Stress Related Problems in Silicon Technology,” *Journal of Applied Physics*, Vol. 70, No. 6, pp. R53–80, September 1991.

[103] S. Chen, T. V. Baughn, Z. J. Yao, and C. Goldsmith, “A New *In Situ* Residual Stress Measurement Method for a MEMS Thin Fixed-Fixed Beam Structure,” *IEEE J. Microelectromech. Syst.*, Vol.11, No. 4, pp. 309-316, December 2002.

[104] Y. Zhu and H. D. Espinosa, “Effect of temperature on capacitive RF MEMS switch performance—a coupled-field analysis,” *J. Micromech. Microeng.*, Vol. 14, No. 8, pp. 1270-1279, June 2004.

[105] V. L. Rabinov, R. J. Gupta and S. D. Senturia, “The effect of release etch-holes on the electromechanical behavior of MEMS structures,” *Tech. Digest, Int. Conf. on Solid-State Sensors and Actuators*, pp 1125–1128, 1997.

[106] Y.-T. Song, H.-Y. Lee, M. Esashi, “A corrugated bridge of low residual stress for RF-MEMS switch,” *Sensors and Actuators* A, Vol. 135, pp. 818-826, September 2007.

[107] S. Moshkalyov, J.A. Diniz, J.W. Swart, P.J. Tatsch, and M. Machida, “Deposition of silicon nitride by low-pressure electron cyclotron resonance plasma enhanced chemical vapor deposition in $N_2/Ar/SiH_4$,” *J. Vac. Sci. Technol. B*, Vol. 15 (6), pp. 2682-2687, 1997.

[108] A. J. Flewitt, A. P. Dyson, J. Robertson, and W. I. Milne, “Low temperature growth of silicon nitride by electron cyclotron resonance plasma enhanced chemical vapor deposition,” *J. Thin Solid Films*, Vol. 383, Issue 1-2, pp. 172-177, February 2001.

[109] S. Bae, D. G. Farber, and S. J. Fonash, “Characteristics of low-temperature silicon nitride SiNx(H) using electron cyclotron resonance plasma,” *J. Solid-State Electronics,* Vol. 44, Issue 8, pp. 1355-1360, August 2000.

[110] S. Garcia, J. M. Martin, I. Martil, G. Gonzalez-Diaz, “Dependence of the physical properties of SiN_x:H films deposited by the ECR plasma method on the discharge size,” *J. Thin Solid Films*, Vol. 315, pp. 22-28, 1998.

[111] R. Daigler, E. Papandreou, M. Koutsoureli, G. Papaionannou, J. Papapolymerou, “Effect of deposition conditions on charging processes in SiN_x: Application to RF-MEMS capacitive switches,” *J. Microelectronic Eng.,* Vol. 86, pp. 404-407, January 2009.

[112] R. N. Simons, *Coplanar Waveguide Circuits, Components, and Systems*, John Wiley & Sons, New York, 2001.

[113] W. Y. Liu, D. P. Steenson, and M. B. Steer, “Membrane-Supported CPW with Mounted Active Devices,” *IEEE Microwave Wireless Comp. Lett.*, Vol. 11, No. 4, pp. 167-169, April 2001.

[114] K. U. Harms, J. T. Horstmann, “Fabrication concept for a CMOS-compatible electrostatically driven surface MEMS switch for RF applications,” *J. Microelectronic Engineering*, Vol. 73-74, pp. 468–473, March 2004.

[115] J. Zhang, W. Ch. Hon, L. L. W. Leung, K. J. Chen, “CMOS-compatible micromachining techniques for fabricating edge-suspended passive components,” *J. Micromech. Microeng.*, Vol. 15, No. 2, pp. 328-335, November 2003.

[116] H. Kanaya, T. Nakamura, K. Kawakami, and K. Yoshida, “Design of Coplanar Waveguide Matching Circuit for RF-CMOS Fron-End,” *Electronics and Communications in Japan*, Part 2, Vol. 88, No. 7, pp.19-26, 2005.

[117] M. A. Abdalla and Z. Hu, “On the Study of Left-Handed Coplanar Waveguide Coupler on Ferrite Substrate” *Progress In Electromagnetics Research Lett.,* Vol. 1, pp. 69-75, 2008.

[118] G. L. Matthaei, L. Young, and E.M.T. Jones, *Microwave Filters, Impedance-Matching Networks, and Coupling Structures*, Norwood, MA: Artech House,1980.

[119] G. E. Ponchak and L. P. B. Katehi, “Open- and Short-Circuit Terminated Series Stubs in Finite Coplanar Waveguide on Silicon,” *IEEE Trans. Microwave Theory Tech.*, Vol. 45, No. 6, pp 970-976, June 1997.

[120] K. Hettak, N. Dib, A. Omar, G.-Y. Deisle, M. Stubbs, and S. Toutain, “A Useful New Class of Miniature CPW Shunt Stubs and its Impact on Millimeter-Wave Integrated Circuits,” *IEEE Trans Microwave Theory Tech.*, Vol. 47, No. 12 pp. 2340–2349, December 1999.

[121] A. K. Sharma and H. Wang, “Experimental Models of Series and Shunt Elements in Coplanar MMICs,” *IEEE Int. Microwave Symp. Dig. MTT-S*, Vol. 3, pp. 1349-1352, 1992.

[122] T. M. Weller, K. J. Herrick, and L. P. Katehi, “Bandstop Series Stubs for Coplanar Waveguide on GaAs,” *IEEE Electron Lett.,* Vol. 33, No. 8, pp. 684–685, April 1997.

[123] K. Hettak, J. P. Coupez, E. Rius, and S. Toutain, “A New Uniplanar Bandpass Filter Using $\lambda_g/2$ Slotline and $\lambda_g/4$ Coplanar Waveguide Resonators,” *Proc. 24th European Microwave Conference*, Vol. 2, pp. 1360-1366, October 1994.

[124] N. I. Dib, G. E. Ponchak, and L. P. B. Katehi, “A Theoretical and Experimental Study of Coplanar Waveguide Shunt Stubs,” *IEEE Trans. Microwave Theory Tech.*, Vol. 41, No. 1, pp. 38-44, January 1993.

[125] S.-S. Liao, H.-K. Chen, Y.-C. Chang, and K.-T. Li, “Novel Reduced-Size Coplanar-Waveguide Bandpass Filter Using the New Folded Open Stub Structure,” *IEEE Microwave Wireless Comp. Lett.*, Vol. 12, No. 12, pp. 476-478, December 2002.

[126] S.-H. Jang and J.-C. Lee, “Miniaturized Elliptic Bandpass Filter Using the Novel Coplanar Double Stepped Impedance Resonator,” *Microwave and Optical Technology Letters*, Vol. 48, No. 6, pp. 1059-1063, June 2006.

[127] K. Hettak, G. Delisle, and M. Boulmalf, “Simultaneous realization of millimeter wave uniplanar shunt stubs and DC block,” *IEEE Int. Microwave Symp. Dig. MTT-S*, Vol. 2, pp 809–812, June 1998.

[128] T. M. Weller, K. J. Herrick, and L. P. B. Katehi, “Quasi-static design technique for mm-wave micromachined filters with lumped elements and series stubs,” *IEEE Trans. Microwave Theory Tech.*, Vol. 45, No. 6, pp. 931–938, June 1997.

[129] R. Baliram Singh, T. M. Weller, M. C. Smith, and J. W. Culver, “Capacitively-Loaded CPW Shunt Stub Notch Filters,” *Microwave and Optical Technology Letters*, Vol. 36, No. 4, pp. 292- 295, February 2003.

[130] D. F. Williams and S. E. Schwarz, “Design and Performance of Coplanar Waveguide Bandpass Filters,” *IEEE Trans. Microwave Theory Tech.*, Vol. MTT-31, No. 7, pp. 558-566, July 1983.

[131] J. K. A. Everard and K. K. M. Cheng, “High Performance Direct Coupled Bandpass Filters on Coplanar Waveguide,” *IEEE Trans. Microwave Theory Tech.*, Vol. 41, No. 9, pp. 1568-1573, September 1993.

[132] D. Ahn, J. S. Park, C. S. Kim, Y. Qian, and T. Itoh, “A Design of the Lowpass Filter Using the Novel Microstrip Defected Ground Structure,” *IEEE Trans. Microwave Theory Tech.*, Vol. 49, No. 1, pp. 86-93, January 2001.

[133] J.-S. Lim, C.-S. Kim, Y.-T. Lee, and et al, “A New Type of Low Pass Filter with Defected Ground Structure,” *European Microwave Week 2002,* Milan, Italy, pp.24-26, September 2002.

[134] J.-S. Yoon, J.-G. Kim, J.-S. Park, C.-S. Park, J.-B. Lim, H.-G. Cho, and K.-Y. Kang, “A New DGS Resonator and Its Application to Bandpass Filter Design,” *2004 IEEE MTT-S Int. Microwave Symp. Dig.,* Texas, pp. 1605-08, June 2004.

[135] A. Boutejdar, A. Batmanov, A. Elsherbini, A. Omar, and E. Burte, “Design of Compact Tunable Band-Pass Filter Using *J*-Inverter and Quasi-Fractal Defected Ground Structure (DGS),” *EUROEM European Electromagnetic Conf.* 2008, Lausanne, Switzerland, pp. 21-25, July 2008.

[136] A. Boutejdar, A. Batmanov, E. Burte and A. Omar, “A Simple Method to Control the Reject Band of Microstrip Low Pass Filter Using a New Multi-Ring Defected Ground Structures (DGS)“, *IEEE AP-S Int. Symp.*, San Diego, California, USA, July 2008.

[137] D.-J. Woo and T.-K. Lee, “Suppression of Harmonics in Wilkinson Power Divider Using Dual-Band Rejection by Asymmetric DGS,” *IEEE Trans. Microwave Theory Tech.*, Vol. 53, No. 6, pp. 2139-2144, June 2005.

[138] J.-S. Lim, J.-S. Park, Y.-T. Lee, D. Ahn, and S. Nam, “Application of Defected Ground Structure in Reducing the Size of Amplifiers,” *IEEE Microwave Wireless Comp. Lett.*, Vol. 12, No. 7, p. 261, July 2002.

[139] A. Boutejdar, A. Batmanov, J. Machac, E. Burte and, A. Omar, “A New Transformation of Bandpass Filter to Bandstop Filter Using Multilayer-Technique and U-Defected Ground Structure (DGS),” *Radioelecktronika Conference 2008*, Prague, Czech Republic, April 2008.

[140] H. Liu, X. Sun, and Z. Li, “Novel Two-Dimensional (2-D) Defected Ground Array for Planar Circuits,” *Active and Passive Electronic Components*, Vol. 27, No. 3, pp. 161-167, September 2004.

[141] H.-M. Kim and B. Lee, “Analysis and Synthesis of Defected Ground Structures (DGS) Using Transmission Line Theory,” *European Microwave Conference,* Paris, France, Vol. 1, pp. 397-400, October 2005.

[142] A. Abdel-Rahman, A. K. Verma, A. Boutejdar, and A. S. Omar, “Control of Bandstop Response of Hi-Lo Microstrip Lowpass Filter Using Slot in Ground Plane,” *IEEE Trans. Microwave Theory Tech.*, Vol. 52, No. 3, pp. 1008-1013, March 2004.

[143] A. Boutejdar, A. Batmanov, A. Omar and E. Burte, “Design of Compact Low-pass Filter Using Cascaded Arrowhead-DGS and Multilayer-Technique”, *Asia Pacific Microwave Conference (APMC) 2008*, China, Hong Kong, pp. 1266-1270, December 2008.

[144] R.-J. Mao, X.-H. Tang, and F. Xiao, “Miniaturized Dual-Mode Ring Bandpass Filters With Patterned Ground Plane,” *IEEE Trans. Microwave Theory Tech.*, Vol. 55, No 7, pp. 1539-1547, July 2007.

[145] J.-S. Lim, Y.-T. Lee, C.-S. Kim, D. Ahn, and S. Nam, “A Vertically Periodic Defected Ground Structure and Its Application in Reducing the Size of Microwave Circuits,” *IEEE Microwave Wireless Comp. Lett.*, Vol. 12, No. 12, pp. 479-481, December 2002.

[146] E. K. I. Hamad, A. M. E. Safwat, and A. S. Omar, “L-Shaped Defected Ground Structure for Coplanar Waveguide,” *2005 IEEE Antennas and Propagation Society Int. Symp.*, Vol. 2B, Washington DC, USA, pp. 663-666, July 2005.

[147] Y.-Z. Wang, M.-L. Her, Y.-C. Chiou, Y-W. Chen, K.-Y. Lin, C.-J. Hsu, “A CPW Defected Ground Structure (DGS) for Bandpass Filter Design,” *Asia-Pacific Microwave Conference 2003*, December 2003.

[148] Y.-L. Lai, P.-Y. Cheng, “CPW Filters with Defected Ground Structures for RF and Microwave Applications,” *9th Joint Conference on Information Sciences (JCIS)*, Kaohsiung, Taiwan, October 2006.

[149] Y.-L. Lai, P.-Y. Cheng, “CPW Filters with Defected Ground Structures for RF and Microwave Applications,” *9th Joint Conference on Information Sciences (JCIS)*, Kaohsiung, Taiwan, October 2006.

[150] E. K. I. Hamad, A. M. E. Safwat, and A. S. Omar, “2D Periodic Defected Ground Structure for Coplanar Waveguide,” *German Microwave Conference (GeMiC 2005)*, Ulm, Germany, pp. 25-28, April 2005.

[151] J.-S. Lim, C.-S. Kim, Y.-T. Lee, D. Ahn, and S. Nam, “A Spiral-Shaped Defected Ground Structure for Coplanar Waveguide,” *IEEE Microwave Wireless Comp. Lett.*, Vol. 12, No. 9, pp. 330-332, September 2002.

[152] V. Radisic, Y. Qian, R. Coccioli, and T. Itoh, “Novel 2-D Photonic Bandgap Structure for Microstrip Lines,” *IEEE Microwave and Guided Wave Letters*, Vol. 8, pp. 69-71, February 1998.

[153] M.-L. Her, C.-M. Chang, Y.-Z. Wang, F.-H. Kung, and Y.-C. Chiou, “Improved Coplanar Waveguide (CPW) Bandstop Filter with Photonic Bandgap (PBG) Structure,” *Microwave and Optical Technology Letters*, Vol. 38, No. 4, pp. 274-277, August 2003.

[154] T.-Y. Yun and K. Chang, “Uniplanar One-Dimensional Photonic-Bandgap Structures and Resonators,” *IEEE Trans. Microwave Theory Tech.*, Vol. 49, No. 3, pp. 86-93, March 2001.

[155] K. T. Chan, A. Chin, M.-F. Li, D.-L. Kwong, S. P. McAlister, D. S. Duh, W. J. Lin, and C. Y. Chang, “High-Performance Microwave Coplanar Bandpass and Bandstop Filters on Si Substrates,” *IEEE Trans. Microwave Theory Tech.*, Vol. 51, No. 9, pp. 2036-2040, September 2003.

[156] J. S. Lim, S. W. Lee, C. S. Kim, J. S. Park, D. Ahn, and S. Nam, “A 4:1 Unequal Wilkinson Power Divider”, *IEEE Microwave Wireless Comp. Lett.*, Vol. 11, No. 3, pp. 124-126, March 2001.

[157] D. M. Pozar, Microwave Engineering, 2nd ed., John-Wiley & Sons, New York, 1998.

[158] A. Abdel-Rahman, *Design and Development of High Gain Wideband Microstrip Antenna and DGS Filters Using Numerical Experimentation Approach*, Ph.D. thesis, University of Magdeburg, FEIT, IESK, 2005.

[159] Sonnet Suite, Sonnet Software, Liverpool, NY, 2007. http://www.sonnetsoftware.com

[160] AWR Microwave Office, Ver. 5.51, http://web.awrcorp.com

[161] B. S. Virdee, “Current Techniques for Tuning Dielectric Resonators,” *Microwave Journal*, Vol. 46, No. 10, pp. 130–138, October 1998.

[162] K. Kageyama, K. Satio, H. Utaki, and T. Yamamoto, “Tunable Active Filters Having Multilayer Structure Using LTCC,” *IEEE Transactions on Microwave Theory and Techniques*, Vol. 49, No. 12, pp. 2421-2424, Dec. 2001.

[163] R. York, A. Nagra, E. Erker, T. Taylor, P. Periaswamy, J. Speck, S. Striffer, D. Kaufmann, and O. Auciello, “Microwave Integrated Circuits Using Thin-Film BST,” *IEEE International Symp. Applications of Ferroelectrics (ISAF)*, Vol. 1, pp. 195–200, July 2000.

[164] D. Mercier, J.-C. Orlianges, T. Delage, C. Champeaux, A. Catherinot, D. Cros, P. Blondy, “Millimeter-Wave Tune-All Bandpass Filters,” *IEEE Trans. Microwave Theory Tech.*, Vol. 52, No. 4, pp. 1175-1181, April 2004.

[165] C. Ong, and M. Okoniewski, “MEMS-Switchable Coupled Resonator Microwave Bandpass Filters,” *IEEE Trans. Microwave Theory Tech.*, Vol. 56, No. 7, pp. 1747-1755, November 2008.

[166] S. Lee, J.-H. Park, J.-M. Kim, H.-T. Kim, Y.-K. Kim, and Y. Kwon, “A Compact Low-Loss Reconfigurable Monolithic Low-Pass Filter Using Multiple-Contact MEMS Switches,” *IEEE Microw. Wireless Comp. Lett.*, Vol. 14, No. 1, pp. 37-39, January 2004.

[167] K. Entesari, K. Obeidat, A. R. Brown, and G. M. Rebeiz, “A 25–75-MHz RF MEMS Tunable Filter,” *IEEE Trans. Microwave Theory Tech.*, Vol. 55, No. 11, pp. 2399-2405, August 2005.

[168] Y. Kwon and S. Lee, “RF MEMS-Enabling Technology for Millimeter Waves,” *IEICE Trans. Electron.*, Vol. E89-C, No. 7, pp. 898-905, July 2006.

[169] S. S. Choi, D. C. Park, “60-GHz Band Dual-Mode Microstrip Ring Resonator Bandpass Filter Using Micromachining Technology,” *Int. J. Infrared Milli. Waves*, Vol. 28, pp. 961–967, September 2007.

[170] C. Lugo, G. Wang, J. Papapolymerou, Z. Zhao, X. Wang, and A. T. Hunt, “Frequency and Bandwidth Agile Millimeter-Wave Filter Using Ferroelectric Capacitors and MEMS Cantilevers,” *IEEE Trans. Microwave Theory and Tech.*, Vol. 55, No. 2, pp. 376-382, February 2007.

[171] M. F. Karim, A. Q. Liu, A. Alphones and A. B. Yu, “A tunable bandstop filter via the capacitance change of micromachined switches,” *J. Micromech. Microeng*. Vol. 16, No.4, pp. 851-861, March 2006.

[172] M. F. Karim, A. Q. Liu, A. B. Yu and A. Alphones, "Micromachined tunable filter using fractal electromagnetic bandgap (EBG) structures" *Sensors and Actuators: A*, Vol. 133, pp. 355-362, July 2006.

[173] E. K. I. Hamad, A. M. E Safwat, A. S. Omar, "A MEMS Reconfigurable DGS Resonator for k-band Applications", *J. Micromech. Systems*, Vol. 15, No. 4, pp. 756-762, August 2006.

[174] ANSYS Release 9.0, *ANSYS Coupled Field Analysis Guide,* Canonsburg, PA 15317, USA: ANSYS Inc., 2004.

[175] S. Gil, M. E. Saleta, D. Tobia, "Experimental Study of the Neumann and Dirichlet Boundary Conditions in Two-Dimensional Electrostatic Problems," *Am. J. Phys*., Vol. 70, No. 12, pp. 1208-1213, December 2002.

[176] J. F. Shackelford and W. Alexander, *CRC Materials Science and Engineering Handbook*, 3rd ed., CRC Press, Boka Raton, FL, 2001.

[177] D. Peroulis, *RF MEMS Devices for Multifunctional Integrated Circuits and Antennas*, Ph.D. thesis, University of Michigan, Electrical Engineering, 2003.

[178] S. M. Sze, *Semiconductor Devices – Physics and Technology*, John Wiley&Sons, New York, 1985.

[179] Oerlikon Balzers System, http://www.oerlikon.com/balzers

[180] Roth & Rau AG., http://www.roth-rau.de

[181] M. Molinari, H. Rinnert and M. Vergnat, "Preparation of dense, smooth and homogeneous amorphous silicon nitride films by nitrogen-ion-beam assisted evaporation," *J. Phys. D: Appl. Phys.*, Vol. 41, 175410 (4pp), August 2008.

[182] Y. T. Kim, D. S. Kim, D. H. Yoon, "Optimization of SiN thin film for high index constant planar silica waveguide," *J. Material Science and Engineering*, Vol. B118, pp. 242-245, 2005.

[183] S. A. Campbell, *The science and Engineering of Microelectronic Fabrication*, 1st ed., Oxford University Press, New York, pp. 269-272, 1996.

[184] Surface Technology Systems, STS AN SPP Company, http://www.stsystems.com

[185] Sentech Instruments GmbH., http://www.sentech.com

[186] SUSS MicroTec Test Systems GmbH., http://www.suss.com

Acknowledgments

Many people have supported and helped me during the time of work to my thesis. On this page, I want to express my gratitude to those people who have supported me carrying out this work.

First and foremost, I would like to thank my advisor, Professor Edmund P. Burte, who gave me the possibility to work in his group at the chair of semiconductor technology in a friendly and encouraging atmosphere, for his invaluable help and advice that I have received during this work.

I am very grateful to my second supervisor Prof. Abbas S. Omar for the valuable help in the field of microwave engineering, for his advices and support.

All my other former and current colleagues at the Chair of Semiconductor Technology are thanked as well. Special thanks belong to Dr. Reinhard Mikuta, Dr. Mindaugas Silinskas, Dr. Bodo Kalkofen, Dr. Marco Lisker, Dr. Cornelia Haase, Mr. Jörg Vierhaus and to all other colleagues for always being ready to help.

I wish to thank Mr. Berndt Garke from Institute of Experimental Physics for fruitful collaboration and supplying the XPS data.

Additionally, I would like to thank all members at the Institute for Electronics, Signal Processing, and Communications for their cooperation and support in the field of RF filters, especially Dr. Ehab Hamad, Mr. Ahmed Boutejdar, Mr. Atallah Balalem and Mr. Nikolaos Spiliotis in addition to the head of the Chair, Prof. Abbas S. Omar. Big thanks go out to Mr. Rodiek and Mr. Dempewolf, these very high technical men in their workshop.

Finally, my deepest feelings of thankfulness go to my parents and my friends for their support, patience and love.

Anatoliy Batmanov

Curriculum Vitae

Name: Anatoliy Batmanov

Date of Birth: January 21, 1979 in Stebnyk, Ukraine

Nationality: Ukrainian

Status: single

E-mail: Anatoliy.Batmanov@ovgu.de

Education

01.2004-12.2009	Works towards Ph.D. degree at the Institute of Micro and Sensor Systems, University of Magdeburg, Magdeburg, Germany.
09.2002-31.12.2003	Research Assistant at Chair of Semiconductor Technology, Otto-von-Guericke University of Magdeburg, Magdeburg, Germany.
2000-2001	M. Sc. in Electronics (Semiconductor Technology) from Lviv Polytechnic National University, Lviv, Ukraine.
1996-2001	B. Sc. in Semiconductor Electronics from Lviv Polytechnic National University, Lviv, Ukraine.
1985-1995	Secondary School Certificate, Stebnyk, Ukraine.

Work Experience

01.2002-09.2002	Research Assistant in Magnetic Sensor Laboratory of Semiconductor Electronic Dept., Institute of Telecommunications, Radioelectronics and Electronic Engineering, Lviv Polytechnic National University, Lviv, Ukraine.
09.2002-till now	Research Assistant for a MEMS research group, Chair of Semiconductor Technology, Otto-von-Guericke University of Magdeburg, Magdeburg, Germany.

Magdeburg, 20.08.2009

Anatoliy Batmanov